Title
Active cellular mechanics and its consequences for animal development

Permalink
https://escholarship.org/uc/item/7fg143vk

Author
Noll, Nicholas

Publication Date
2017

Peer reviewed|Thesis/dissertation

UNIVERSITY of CALIFORNIA
Santa Barbara

Active cellular mechanics and its consequences for animal development

A dissertation submitted in partial satisfaction of the
requirements for the degree of

Doctor of Philosophy

in

Physics

by

Nicholas B. Noll

Committee in charge:

Professor Boris I. Shraiman, Chair

Professor Otger Campas

Professor Matthew P. Fisher

September 2017

The dissertation of Nicholas B. Noll is approved:

Professor Otger Campas

Professor Matthew P. Fisher

Professor Boris I. Shraiman, Chair

September 2017

To my mother and father, without whom I would not be writing this dissertation.

Acknowledgements

This dissertation would not have been completed without the support and instruction of many people. My deepest gratitude goes to:

My adviser Boris I. Shraiman for his incredible mentorship and support throughout the course of my PhD career. His physical intuition, critical insight and genuine grace are extraordinary and serve as an inspiration for my scientific career. I hope in my time as his student I have absorbed a fraction of his skills and generosity.

My close collaborator Madhav Mani for both introducing me to the beauty (and physics) of developmental biology and forcing me to occasionally not worry about the microscopic details but instead deal with the fundamental questions at hand. I enjoyed working with you at the KITP late into the night immensely. I hope we continue working together.

Sebastian J. Streichan for teaching me how to open a bottle of beer using just a car key. More seriously, our collaboration taught me a lot about developmental biology and the world of experiments. I am in awe of your ingenuity and resourcefulness in the lab.

My family, especially my mother and father, Julie and Jerald Noll without whom I could not have written this dissertation. They both instilled the spirit of learning in me at an early age. Beyond academics, the support and love I was given throughout my youth was critical to my development (no pun intended). To my mom, I can only hope I can give back a fraction of what you've given to me. To my dad, I thank you for showing me what it means to live and I wish you were here in this moment.

The close friends I've made in my time here at UCSB. A special thanks go out to my roommates Andrew Dunsworth, Kenny Lee, Jason Iaconis, Kurt Fujiwara and Scott Haselschwardt whose many distractions in the form of climbing trips and late-night discussions ranging from physics to dessert classifications kept me sane. I hope we remain life-long friends.

Kelly A. Pawlak (or more affectionately Kiwi) whose physical intuition, resourcefulness, and ability to synthesize information to get to the kernel of truth constantly amazes me. This dissertation is intelligible in no small part due to her critical eye. I also would be remiss to mention our dog Kona, whose many requested walks served as a source of ideas.

The many teachers and friends over the years who have inspired a love of science and life in me.

Curriculum Vitæ

Nicholas B. Noll

Education

2017 Ph.D., Physics, University of California, Santa Barbara

2012 B.S., Physics, University of Washington, Seattle

2012 B.S.E.E, Electrical Engineering, University of Washington, Seattle

2007 Eastside Catholic, Bellevue

Professional Experience

2012	Graduate Student Researcher, University of California, Santa Barbara

Publications

N. Noll, M. Mani, I. Heemskerk, S.J. Streichan, B. Shraiman. Active Tension Network model suggests an exotic mechanical state realized in epithelial tissues. *Nature Physics*

S.J. Streichan, M. Lefebvre, N. Noll, E. Wieschaus, B. Shraiman. Quantification of myosin distribution predicts global morphogenetic flow in the fly embryo. *arXiv*:1701.07100

Abstract

Active cellular mechanics and its consequences for animal development

by

Nicholas B. Noll

A central goal of developmental biology is to understand how an organism shapes itself, a process referred to as morphogenesis. While the molecular components critical to determining the initial body plan have been well characterized, the control of the subsequent dynamics of cellular rearrangements which ultimately shape the organism are far less understood. A major roadblock to a more complete picture of morphogenesis is the inability to measure tissue-scale mechanics throughout development and thus answer fundamental questions: How is the mechanical state of the cell regulated by local protein expression and global pattering? In what way does stress feedback onto the larger developmental program?

In this dissertation, we begin to approach these questions through the introduction and analysis of a multi-scale model of epithelial mechanics which explicitly connects cytoskeletal protein activity to tissue-level stress. In Chapter 2, we introduce the discrete Active Tension Network (ATN) model of cellular mechanics. ATNs are tissues that satisfy two primary assumptions: that the mechanical balance of cells is dominated by cortical tension and that myosin actively remodels the actin cytoskeleton in a stress-dependent

manner. Remarkably, the interplay of these features allows for angle-preserving, i.e. 'isogonal', dilations or contractions of local cell geometry that do not generate stress. Asymptotically this model is stabilized provided there is mechanical feedback on expression of myosin within the cell; we take this to be a strong prediction to be tested.

The ATN model exposes a fundamental connection between equilibrium cell geometry and its underlying force network. In Chapter 3, we relax the tension-net approximation and demonstrate that at equilibrium, epithelial tissues with non-uniform pressure have non-trivial geometric constraints that imply the network is described by a weighted 'dual' triangulation. We show that the dual triangulation encodes all information about the mechanical state of an epithelial tissue. Utilizing the stress-geometry duality, we formulate a local "Mechanical Inference" of cellular-level stress using solely cell geometry that dramatically improves over past image-based inference techniques.

In Chapter 4, we generalize the ATN model to explore the controlled re-arrangement of cells within epithelial tissues. This requires us to explicitly consider the effects of cadherin mediated adhesion, and its regulation, on tissue morphogenesis. We find that positive feedback between myosin and cortical tension, along with traction-dependent depletion of cytoskeletal cadherin is sufficient to recapitulate the morphogenetic movement of cells observed during convergent extension of the lateral ectoderm during Drosophila embryogenesis. Statistical analyses of live-imaging data supports the fundamentals of the model.

Chapter 5 focuses on morphogenesis at a mesoscopic scale by coarse-graining the

cellular ATN model. Under this limit, we expect an epithelial tissue should behave as an effective viscous, compressible fluid driven by myosin gradients on intermediate timescales. Theoretical predictions are empirically tested against in-toto microscopy data obtained during early Drosophila embryogenesis.

Contents

Chapter 1

A physicist's introduction to developmental biology

The embryo exists between the fertilization of a single-celled egg, which bears no morphological resemblance to the final animal, and the eventual birth of the assembled organism. As such, the embryo bridges heredity and physical form, translating discrete genetic information into the development of shape in both space and time, a process known as *morphogenesis*. Development of the embryo into a complex organism requires precise spatio-temporal patterns of gene expression, cell growth, differentiation and cellular rearrangements. Developmental biology thus synthesizes many of the relevant scales of life; a complete understanding of the developmental program must connect gene regulation to the cellular-level processes that ultimately control the collective shaping of tissues.

From the physicist's perspective, classical mechanics provides the natural language for the causal driver of the dynamics of morphogenesis. Cells move and reorganize only when subject to an applied net force. For this reason, the precise orchestration of cellular rearrangements, growth and divisions must be regulated by a precise stress field. This sentiment is, of course, not new – it dates back to D'Arcy Thompson's seminal work in 1917, entitled *On Growth and Form* [167]. Despite its purely descriptive nature, Thompson's book provides a compelling and exhaustive case for the central thesis: biological form is a direct consequence of *physical processes and mechanical forces.* As succinctly summarized by Thompson himself, "the form of a [biological] object is a diagram of forces ... [such] that from it we can deduce the forces that are acting or have acted upon it." [167] Refinement of Thompson's ideas into predictive models was largely impeded by the complete lack of experimental data and empirical knowledge of underlying cell biology, however the book served as an influential narrative for the successive generations of scientists on the interface of Physics and Biology [19].

Despite steady advances in knowledge of fundamental biology since Thompson's publication, developmental biologists have had limited success in fulfilling his vision of quantitatively modeling organisimal development as a physical process. We pause to raise an enlightening question: Why has it taken so long?

Developmental biology has certainly not been idle. Following the dominating revolution of molecular biology through the 20th century, much of the field has focused on the biochemical aspects of development. Contrary to Thompson's 'diagrams of forces', embryos were described in the opposite limit, as passive substrates of chemical reactions between genes and gene products. The molecular worldview coalesced into a distinct thesis of 'chemical embryology' [121]: emergent genetic patterns dictate the fate of cells and ultimately cell morphology.

The mathematical framework of 'chemical embryology', was best formulated within Alan Turing's pioneering work *The Chemical Basis of Morphogenesis*, published in 1952 [169]. The paper outlined a simple core idea - the patterns observed within biological tissues can emerge spontaneously from underlying simple chemical reactions of diffusing molecules. Specifically, Turing showed that a kinetic equation which involves a fast-diffusing inhibitory molecule interacting with a slow-diffusing self-activator will generically generate a tunable, spatially periodic pattern from a homogeneous initial state [169]. He coined such molecules *morphogens*. Turing's work turned out to be prescient; it is now well-established that multicellular organisms use a myriad of morphogens to spatially pattern cell identity and differentiation within developing tissues [149, 66]. Beyond Turing's original proposed mechanism, morphogen gradients have further been shown to provide critical positional information - i.e. allowing cells to quantitatively know their location relative to the source by measuring concentration [183]. In short, Turing defined *the* questions that would prove central to developmental biology in the age of molecular genetics: what are the morphogens controlling each tissue's shape and how are they spatially patterned?

Just a year after the publication of *The Chemical Basis of Morphogenesis*, Watson and Crick discovered the structure of DNA, establishing the framework of modern molecular biology [178]. In the following decade, the relationship between DNA, RNA, and proteins would be cemented into the central dogma of biology and thus fueled the reductionist's vision that genes are the blueprints to life. Furthermore, the discovery of the lac operon in *E. coli* made clear that such genes can be controlled spatio-temporally by the cell [84]. Taken together, it was evident that the theoretical morphogens thought to orchestrate the pattern and sequence of embryonic development through induction of cell fate corresponded to regulated genes and their associated proteins. The task at hand for developmental biologists was conceptually clear yet experimentally daunting; one must enumerate the complete list of genes responsible for each developmental process through phenotypic assays of genetic knockout mutants (embryos whose genotype have a defunct individual gene relative to normal, commonly referred to as wildtype) [180]. In 1979, Christiane Nüsslein-Volhard and Eric Wieschaus launched a monumental mutagenesis screen, commonly referred to as the Heidelberg screens due to the location of the experiment, in *Drosophila melangastor* embryos which culminated in a list of 140 genes responsible for distinct developmental phenotypes visibly manifest on the level of the larval cuticle. [129]. For example, Nüsslein-Volhard and Wieschaus elucidated the hierarchy of genes responsible for anterior-posterior (head-tail) patterning and segmentation. Through subsequent maternal screens, the diffusible transcription factor *bicoid*, was found to be maternally deposited at the anterior pole in order provide quantitative positional information for cells regarding their location along the anterior-posterior axis [128]. This was the first example of a morphogen found in-vivo [48]. The gradient provided by *bicoid* defines the 'head' region of the embryo and is sequentially processed through the hierarchy of genes found in the original screens; broad expression of the 'gap genes' is refined into the fine expression of 14 segment forming 'pair-rule' genes that further subdivide into 'segment-polarity' genes. Mutation of any gene in this hierarchy will lead to loss of the corresponding segment in the larvae. For example, deletion of the pair-rule gene *even-skipped* will lead to loss of every other larval denticle [129].

The success of the Heidelberg screens influenced embryologists to produce intricate, detailed lists of molecules and their corresponding regulation of particular embryonic phenotypes [60, 87]. The description was largely binary, constrained to the realm of morphology with and without the presence of each gene. While sufficient for describing dramatic phenotypes, such as complete loss of certain segments associated to loss of the homeotic genes, many more subtle phenotypes proved hard to assess [180]. As a result, one could only say this particular gene is important for this particular developmental process at this particular region and time, but the causal influence of the gene in directing form and shape remained opaque.

Modern developmental biology is undergoing a quantitative revolution spurred by the development of genetically encoded fluorescence markers such as the green-florescent protein (GFP) [158, 138] and its derivatives that, upon transgenic implantation into a targeted gene of interest, allow one to optically measure the expressed concentration of a protein within live cells with a fluorescent microscope [28]. Coupled with a sophisticated genetic toolbox developed over the last century which allows complete editing control over entire genomes [110], researchers now have unprecedented observational power over genotypes and the resultant developmental dynamics of embryos. Furthermore, the current development of optogenetics holds promise of allowing scientists to ‘paint’ their own de-novo gene expression patterns [43].

Despite the explosion of live-imaging data capturing the dynamics of in-vivo development, there still remains a dearth of mechanistic, *predictive* models of development that couple cellular activity and biochemical patterns to the resultant physical forms of organisms [130, 40]. Central to this limitation is that, despite the fact that we know mechanics is directly causal in shaping collections of cells into functional units and we have exhaustive lists of putative molecular determinants of phenotypes, there remains no quantitative model for the distribution of forces, its regulation by morphogen signaling, and potential feedbacks onto gene expression within biological matter that is directly supported by experimental evidence [115, 184]. Basic questions regarding tissue mechanics, the constitutive relationship between stress and strain in living cells, and how connected tissues undergoing different morphological transitions mechanically interact with each other still remain unanswered.

It is time to revisit D’Arcy Thompson’s vision of biological form as manifestly equivalent to a ‘diagram of forces’ [167], however grounded within the research of molecular embryology of the past century. Can we begin to tease apart general principles of the interplay between the biochemical signaling within the cell, its emergent mechanical properties, and the resulting force field of the tissue? We are currently entering an important era of synthesis within developmental biology which must merge the complementary models of biochemical and biophysical embryology into a predictive and quantitative science. In this dissertation, we aim to model the simultaneous control of mechanics, shape, and cell fate by biochemical expression. Starting from a simplified picture of cell biology, we deduce a phenomenological model of cellular mechanics that allows us to bridge the gap between molecules and tissues. While we are not the first to approach morphogenesis from this angle, as will be discussed in detail below, we are the first to explicitly model the relationship between cytoskeletal protein activity and cellular-level stress. This allows us to not only literally derive the 'diagram of forces' and cell morphology from just patterns of expressed proteins but we also obtain quantitative predictions that are immediately falsifiable against live-imaging data. We firmly believe that refinement of such phenomenological models against empirical data is the best way to uncover the general principles of development.

We must confront the major epistemological issue raised above. Is it reasonable to suspect that the embryonic development of evolutionarily diverged organisms across the tree of life can be described by a simple set of general principles? With the apparent complexity of living systems, it may seem that theoretical physicists entering developmental biology are constrained to formulate patchwork phenomenological models of individual developmental processes, an elaborate form of 'stamp collecting' [35]. One hopes that, since embryos act as the map between genotype and phenotype, development must have simple principles that evolution can easily access and tune. The myriad of cases exhibiting convergent evolution of organismal form, despite massively divergent evolutionary paths, tenuously corroborates this belief [160]. Furthermore, developmental processes seem to be strongly conserved across organisms [150].

Experience from many-body physics instructs us that universality can emerge from the complex interactions of many particles, cells in our present case. This sentiment was marvelously espoused by Phil Anderson in *More is Different* [5], in which he states, "the behavior of large and complex aggregates of elementary particles, it turns out, is not to be understood in terms of a simple extrapolation of the properties of a few particles. Instead, at each level of complexity entirely new properties emerge... entirely new laws, concepts, and generalizations are necessary." The patterns that emerge from extensive 'stamp collecting' can lead to universal laws. Tycho Brahe was unaware of the classical law of gravitation despite his meticulous documentation of stellar and planetary orbits [166]. Sadi Carnot was oblivious to the profound connections between the 2nd Law of Thermodynamics and his derived constraint on the efficiency of heat engines [25]. In many additional cases throughout history, phenomena were humbly modeled long before the underlying general principles were clarified. We take this as inspiration for the work to follow. The purpose of this dissertation is not to outline the "Grand Unified Theory of Development", but rather take a critical first step towards discovering it via the formulation of predictive toy models validated by empirical data.

In the next section, we present the microscopic architecture of cellular organizations. As alluded to above, we can't simply understand the mechanics of biological matter by understanding the mechanics within a single cell: we must consider how cells mechanically interact with their immediate environment and thus each other. After introducing the cell biology relevant to the model proposed within the thesis, we review previous models of cellular mechanics and discuss their successes and limitations. Lastly, we outline various state-of-the-art stress assays that can be used to probe predictions of the model.

1.1 Epithelial tissues are a building block of life

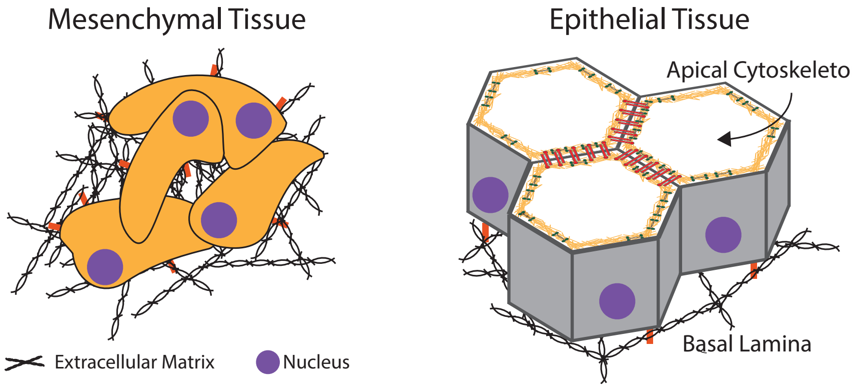

Figure 1.1: Cartoon representations of both mesenchymal and epithelial tissues. Mesenchymal cells, shown on the left, exhibit strong adhesion to the extracellular matrix (ECM), a rigid network of secreted proteins shown in black, but weak intercellular connectivity. As a result, mesenchymal cells crawl along the substrate, exhibiting fluid-like behavior. Conversely, epithelial cells form confluent sheets due to strong intercellular adhesion mediated by transmembrane proteins. Epithelial cells adhere weakly to the ECM, strictly at their basal (interior) side. Taken together, epithelial cells exhibit strong apico-basal polarity.

Cells organize into two principal tissue types within developing embryos, the mesenchyme and the epithelia [86, 168, 9], delineated primarily by the adhesive interactions between the cell, it's neighbors, and the extracellular matrix (ECM), a rigid structure of secreted proteins that provide supports and structure to the embedded cells [58]. In particular, mesenchymal cells exhibit little adhesion to neighboring cells and consequently form a loose aggregate of cells that migrate rapidly along the dense ECM [134]. Cell motility can be directed by either chemical or mechanical gradients. Mesenchymal cells exhibit rapid turnover of proteins allowing for rapid cell shape changes. As such, mesenchymal cells are often found in the adult connective tissue [3].

Conversely, epithelia are sheets of strongly connected cells, with a well defined apical and basal side facing away from and towards the body respectively [177, 100]. In a sense, epithelial tissues act much closer to physical solids relative to the mesenchyme and must actively reorganize cellular contacts to remodel its collective shape [99]. Epithelial cells are strongly apico-basal polarized; cells transmit forces to neighboring cells apically and attach to the sparse ECM basally [68]. Epithelia protectively line all surfaces and cavities within the adult body, acting as an effective barrier due to strong cell cohesion, and thus ubiquitously undergo dramatic shape transformations during morphogenesis [3]. For the remainder of this dissertation, we focus exclusively on the mechanics of epithelial tissues and thus turn our attention to a simplified introduction of the biochemical components critical to the mechanical integrity of an epithelium. It is important to note, the underlying system is *vastly* more complicated than the presentation below suggests, with an entire zoo of supporting proteins that aid in the structural network of the epithelial cell. In lieu of complexity, we seek to describe what we believe to be the minimal components that adequately capture the underlying cell biology.

The majority of epithelial tissue stress is generated and carried within the cell's actin cytoskeleton, an organized scaffolding of filamentous proteins localized to the apical cortex implicated as the primary driver of cell shape transformations, migration, and mitotic cleavage [100]. Actin is among the most prevalent, highly conserved, intracellular proteins within eukaryotic cells [47]. It exists in two primary forms: as a globular monomer known as G-actin and a filamentous polymer, called F-actin, that is constructed from a linear, helical chain of G-actin units. F-actin is polar, owing to the fact that each actin monomer orients along the anisotropic direction [76]. The end with an exposed ATP (Adenine triphosphate, commonly referred to as the unit of energy currency used ubiquitously by the cell [3]) binding side is referred to as the (-) end. The other is conveniently called the (+) end. Actin filaments are incredibly stiff with a measured Young's modulus of approximately 2.6 GPa, roughly a factor of 10 higher than that of the average eukaryotic cell [61]! In other words, the rigidity of actin is entirely sufficient to explain the mechanical integrity of the cell but is too stiff to explain the cellular deformations observed during morphogenesis relative to the known scale of active forces generated [55]. The compliance of cells thus comes from the higher level of organization seen in the cell's cytoskeleton.

The actin cytoskeleton is constructed from parallel, closely packed bundles of F-actin filaments found at the apical periphery of the cell; the observed deformation of cells is due to relative reorganization of these compliant bundles [59]. In other words, the overall deformation of cells is due to the sliding of actin filaments relative to each other, rather than deformation of an individual filament itself. This is dramatically seen in the dynamic organization of the actin cytoskeleton which drives cell migration [135]. As such, the relevant mechanical component to the cell is the entire network of F-actin bundles [55]. Internally, F-actin bundles are cross-linked by many proteins, each of which intricately regulates the dimensions, architecture and mechanical properties of the resultant composite structure [33]. For example, Fimbrin is a small actin crosslinker that forms tightly connected, stiff bundles in contrast to the much larger protein α-actinin that results in loose bundles found concentrated in stress fibers as it allows for contractile elements [3]. While we will not concern ourselves with intimate molecular details in this dissertation, it is important to note this is an example of the effect of microscopic cellular activity affecting tissue-scale mechanics; cells can dynamically regulate their stiffness! The cytoskeleton is connected to the plasma membrane, allowing for autonomous control over cell shape.

One of the most important actin binding proteins is a molecular motor known as myosin, which utilizes the energy obtained from repeated cycles of ATP hydrolysis to unidirectionally walk along F-actin [101]. While myosins constitute a superfamily of proteins implicated in many cellular functions ranging from vesicle transport to phototransduction [71], we will limit our discussion to the actin-crosslinking protein class ubiquitous in generating cellular contractility, myosin II. The structure of myosin II consists of what is known as two heavy chains that each contain the head and tail molecular domains. The head domain binds to F-actin while the tail domains wrap around each other in a coiled-coil morphology. As such, myosin II has two head domains allowing it to cross-link F-actin within a cytoskeletal bundle [171]. Each head domain contains an ATP binding site that is allosterically activated once bound to actin [3]. The resultant chemical energy obtained from the bound ATP is converted into forward movement towards the (+) end of F-actin [170]. Provided each head is bound to filaments of opposite orientations, the net result of both heads' activity will work to slide each filament past each other. The relative displacement of fibers within a bundle pulls on the compliant actin cross-linking proteins such as α-actinin, resulting in a self-tensed network [147]. Myosin II thus generates active contraction of the actin bundle through the generation of internal strain. This is most dramatically seen in in-vitro experiments where actin and myosin gels contract to a point under free boundary conditions [13]. Hereafter, we refer to the entire 'active' complex as an actomyosin bundle.

Importantly, myosin II exhibits a load-dependent walking rate, beautifully observed in single molecule experiments [92, 127]. Via an optical trap, the walking kinetics of a single myosin II motor was measured as a function of the applied force to the molecule using an attached dielectric bead embedded within an inhomogeneous light beam. Generically, the motor protein occasionally takes a backwards step towards the (-) end. As the applied force approaches the stall force, measured to be 2.2 pN for a single myosin II, the probability to walk towards the (+) and (-) end of the filament is equal [92]. Hence, the motor has 'stalled'. As you increase the load past the stall force, the motor probabilitically 'slips' and allows the actin bundle to elongate [127]. The ability for the molecular motor to physically stall while actively undergoing ATP hydrolysis is critical for the cell to maintain constant cortical tension of the cytoskeleton at constant shape [120].

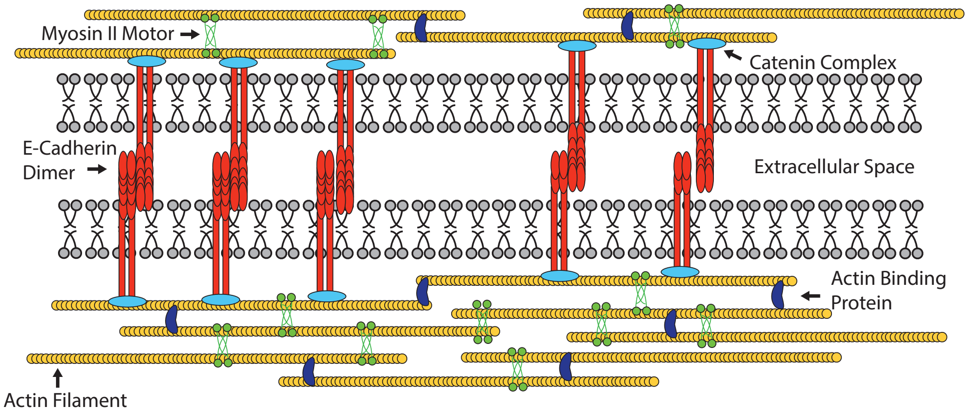

Figure 1.2: Cartoon representation of the simplified actin cytoskeleton found at the apical periphery of an epithelial cell outlined in this section. Globular actin (shown as orange circles) polymerizes into stiff filaments, known as F-actin. The dense network of filaments is subsequently cross-linked by various actin binding proteins (shown in dark blue) as well as the molecular motor myosin II (green), forming a higher level of organization known as the acto-myosin bundle. Myosin II utilizes ATP to actively contract the network by sliding filaments relative to one another. Tensile load is shared by neighboring cells by cadherin (shown in red) mediated adhesion. Cadherins are anchored to the actomyosin bundles through catenin complexes.

How do epithelial cells form a confluent layer that transmits cell-autonomous contractile stresses across the entire tissue? In other words, what plays the role of particle adhesion in biological matter? As is often the case in biology, a full description of the myriad of proteins implicated in cell-cell adhesion could fill an entire textbook. We will restrict our attention to the predominant adhesive molecular complex known as the adherens junction (AJ), a group of proteins expressed continuously along the apical surface of epithelial cells [70]. Cadherins are the core transmembrane protein within adherens junctions [126, 69]. As with myosin motors, cadherins consitute a large family of proteins. Our present discussion will focus on the sub-class of epithelial associated cadherin molecules, or E-cad in abbreviation. The extracellular domain of the E-cad molecules initiate cell-cell adhesion through Ca2+ dependent homophilic bonds to the extracellular domain of E-cads expressed on apposing cells to form a dimer pair [69]. Each homodimer can support roughly 30 pN of tension before dissociation and subsequent detachment of both molecules [7]. Interestingly, this sets a soft constraint on the amount of tolerable stress before the tissue loses mechanical integrity. The cytoplasmic domain, highly conserved across all cadherin subtypes, binds to the actin cytoskeleton via anchor proteins such as the catenins and vinculin [122, 72]. Thus the actomyosin bundles of apposing cells are mechanically linked together, allowing each cell to share and transmit tissue-wide stress via traction forces exerted on neighboring cell surfaces.

In addition to acting as the predominant adhesive protein responsible for maintaining a confluent layer, E-cadherin is actively regulated by the cell during morphogenesis, similar to myosin II [98]. AJs appear to be in a state of continuous turnover in a manner that depends on cortical tension [42]. Specifically, myosin contractility destabilizes AJs and ultimately reduces E-cad levels on high-tension interfaces [181, 11]. The opposite effect of the stabilization of AJs and of Cadherin adhesion is associated with membrane localization of Bazooka/Par3 protein [186]. A quantitative understanding of the feedback networks between mechanics, cadherin-mediated adhesion, and myosin driven cortical tension will be crucial towards a predictive model of development.

In addition to the junctional actin network, a dense actin web permeates the apical surface of each epithelial cell. This is commonly referred to as the medial actin cytoskeleton, and is implicated as the primary driver of cell shape changes during apical constriction preceding invagination at the ventral furrow [109], posterior midgut [124], and formation of tracheal pits [125] during Drosophila morphogenesis. In all three examples, the contractile dynamics were putatively caused by observed pulsatile myosin dynamics. Structurally, the medial actomyosin network is anchored to the cortical cytoskeleton by stable connections formed by Diaphanous [111] and has been determined to isotropically pull on the cell's apical perimeter, acting as a controllable, effective bulk pressure [108].

All taken together, an epithelial tissue can be thought of as a two-dimensional elastic network of *active* cytoskeletal elements in which cortical tension, cell-cell adhesion, and uniaxial cellular pressure determine the geometric properties of cells and thus the global shape of the tissue. However, the precise connection and potential feedback mechanisms between expression levels of the aforementioned cytoskeletal proteins and the resultant tissue-level stresses that drive morphogenetic movements remain unclear. Despite critical advances in live-image technology that allow us to observe protein expression patterns in real-time with sub-cellular resolution, we still have no such quantitative in-vivo assay for global stress within the tissue during morphogenesis. Progress requires quantitative modeling of the interactions between these components. Towards this goal, this dissertation will present a model that explicitly connects the activity of myosin and active recruitment of cytoskeletal proteins to tissue-scale mechanics.

1.2 Modeling epithelial morphogenesis

Modeling the role of gene expression, biochemistry, and epithelial tissue mechanics in the context of morphogenesis has a long history in the mathematical biology and biomechanics communities [132, 119, 131, 88]. Historically, researchers have taken two complementary and orthogonal approaches to capture the active mechanics of an epithelial tissue: viewing the epithelium either as a continuum material by postulating a set of hydrodynamic equations or as granular matter using discrete, cell-based models that in aggregate form the tissue [184]. The former often proves to be analytically tractable but hard to parse the direct relationship between the model's phenomenological parameters and the physical quantities of the cell, while the latter benefits from explicit modeling of cell and molecular biology but is often solved only with the help of numerical computation.

The fundamental degrees of freedom of hydrodynamic theories of epithelial morphogenesis are cell density $\rho(\boldsymbol{r}, t)$ and the tissue-level stress tensor $\sigma(\boldsymbol{r}, t)$ [106]. Continuum models often postulate that the epithelial tissue acts as a visco-elastic material, behaving as a deformable solid during quick experimental manipulations but exhibiting cell sorting behavior akin to a liquid in long-term organ cultures [106]. Rheological experiments support this hypothesis, [56] and we will later see how such macroscopic behavior can emerge from simple actomyosin contractility microscopically. The cell's ability to actively contract relative to its environment is modeled as internal force dipoles within a coarse-grained 'active' stress tensor σ_{active}. Active stress is thought to both drive tissue flow and balance externally applied forces [85]. When connected to biochemistry, such models exhibit Turing-like symmetry breaking of the uniform ground state [132]. In recent years, generalizations of these hydrodynamic equations have been explored that couple an additional 'shape' nematic tensor field $\boldsymbol{Q}(\boldsymbol{r}, t)$, thought to capture the local geometric anisotropy of cells, into the dynamics [136]. A simplified version of this model has recently been utilized to understand the relevant forces during morphogenesis of the pupal wing of Drosophila [51]. However, continuum level models have limitations: assumed phenomenological parameters will in reality depend upon cellular activity outside of the modeled simple additive stress, ultimately limiting their predictive power of morphogenetic dynamics. Elucidation of these dependencies and their direct connection to gene expression *requires* multiscale modeling starting from discrete cells [141]. We thus focus the remainder of our attention on describing past efforts regarding discrete cellular models. Interested readers are referred to [106] for thorough reviews of the continuum approaches to epithelial morphogenesis and the burgeoning field of 'Active Matter.'

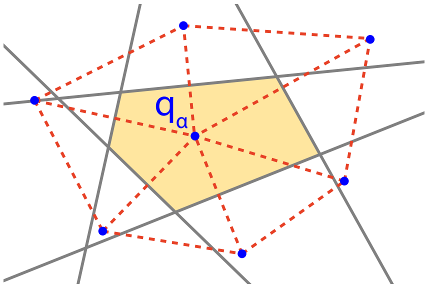

Figure 1.3: An illustrative example of the Voronoi construction for 7 generating points $\boldsymbol{q}_\alpha$. Each Voronoi cell can be obtained by drawing all perpendicular bisections of displacement vectors between generating points, shown as the gray solid lines. The intersection of all such lines forms the outline of the corresponding Voronoi cell, the interior here is shown in orange. This procedure simultaneously defines the 'dual' Delaunay triangulation, shown in the red dashed lines here.

The complementary modeling approach is to focus view tissue morphogenesis at the cellular level and thus resultant from patterned cell shape changes and coordinated rearrangements. This requires parameterization of the shape of the epithelial cell. Although D'Arcy Thompson recognized that cells affected one another's shape through a 'triangle of forces' akin to a soap foam [167], the first systematic study of cellular tessellations formed at the apical surface of an epithelial tissue was published in 1978 by Hisao Honda which showed many examples of epithelial cells that were well approximated by a Voronoi tessellation, commonly known as the Wigner-Seitz construction to physicists [78]. A Voronoi tessellation is constructed from a discrete set of generating points, denoted $\{\boldsymbol{q}_\alpha\} \in \mathbb{R}^2$, by taking the intersection of all half-spaces closest to point $\boldsymbol{q}_\alpha$ relative to the remaining generators within the set [173]. As such, each Voronoi cell forms a convex polygon which contains all points in the plane closest to its corresponding generating point, as shown in Fig. 1.3. Connecting neighboring generating points forms the 'dual' Delaunay triangulation. Under this approximation, an observed cellular flow could be parameterized simply by the movement of the underlying generating points $\{\boldsymbol{q}_\alpha\}$. As will be shown in Chapter 5, Honda's initial assessment wasn't too far off from the general description of cellular aggregates.

The Vertex Model, initially developed to describe the random 2D patterns observed in dry foams and grain aggregates [64, 179], soon supplanted the Voronoi approximation as the predominant idealization of epithelial apical geometry [79]. As before, cells are approximated as a planar polygonal network, however generalized such that vertex positions $\boldsymbol{r}_i$, loci where three or more cells meet, are the geometric degrees of freedom.

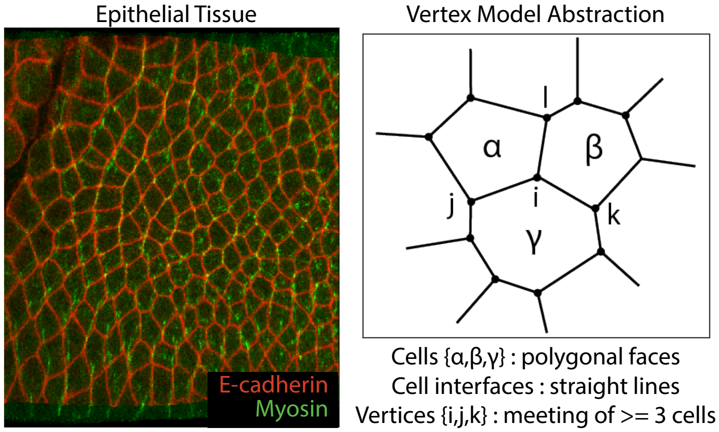

Figure 1.4: (Left) Fluorescence live-imaging data taken from the lateral ectoderm of Drosophila during the onset of germ-band extension showing the apical surface of the epithelium. E-cadherin is shown in red and myosin is shown in green. Note the approximate polygonal behavior of the cell array. (Right) We show the abstraction of the apical geometry of an epithelial tissue as a Vertex Model. Cells are represented as convex, polygonal faces. In this dissertation, all cells will be labeled by greek letters. Vertices are the positions where 3 or more cells meet - they will be labeled by roman letters.

Vertices are connected by straight lined edges representing intercellular junctions. See Fig. 1.4 for a graphical depiction of the abstraction. In addition to geometric dynamics parameterized by vertex positions, the overall topology of the planar array is allowed to evolve through three elementary processes, summarized in Fig. 1.5. The first, called a T1 process, constitutes a neighbor exchange between cells. It can be thought of as an edge shrinking to zero, followed by subsequent replacement with an orthogonal one. Cell death and mitosis are similarly referred to as a T2 and T3 process respectively [179].

Morphogenesis of the cellular network is specified entirely by the vertex dynamics, $\dot{\boldsymbol{r}}_i$, and an algorithm for the execution of the elementary topological transitions that are driven by forces acting on vertices [54, 4]. The Vertex Model assumes each vertex is

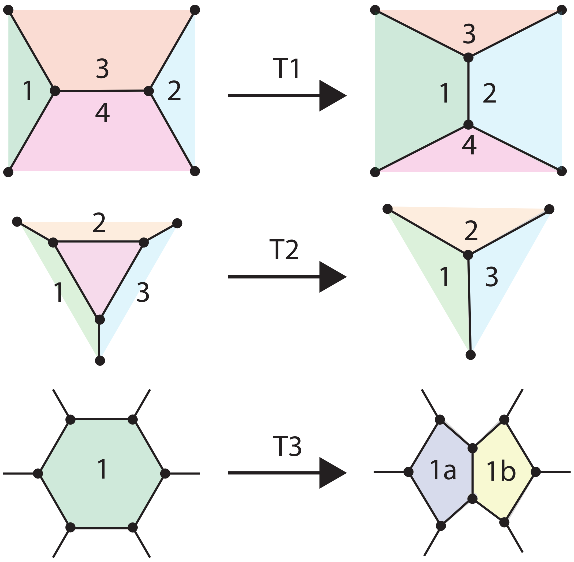

Figure 1.5: Graphical illustration of the three elemental topological rearrangements defined for discrete network based models of aggregate materials in $2D$. A T1 process is a local neighbor exchange between cells, a T2 process can be thought of as extrusion from the confluent layer and thus models cell death and a T3 process is the net result of a mitosis event.

embedded within a viscous medium and that dynamics are relaxational

$$\nu \frac{d}{dt}\boldsymbol{r}_i = \boldsymbol{F}_i = -\frac{\partial E}{\partial \boldsymbol{r}_i} \tag{1.1}$$

Mechanical equilibrium is reached when the net force is zero and vertices stop moving. There is no universal convention regarding the choice of the functional form for E or the number of parameters modeled per cell, although they are often parameterized in terms of cell area and edge length $E[\{A_\alpha\}, \{r_{ij}\}]$. Microscopic details are determined by the discretion of the individual researcher and the particular morphogenetic event intended to be modeled, resulting in an abundance of examples in the literature [80, 52, 146, 29]. We focus on a few recent examples that have dramatically influenced the biomechanics community.

Farhadifar et. al [52] were interested if cellular mechanics, modeled as a polygonal vertex model, coupled to cell proliferation, is sufficient to quantitatively describe the observed geometries of the growing pupal Drosophila wing. The mechanical energy approximated the tissue by only its apical cross-section similar to the traditional vertex models used by Honda [79], however with the introduction of an elastic contribution from the actin cytoskeleton on the perimeter of the cell

$$E\left[\boldsymbol{r}_i\right] = \sum_{\alpha} \left[\frac{K_\alpha}{2} \left[A_\alpha - A_{0,\alpha}\right]^2 + \frac{\Gamma_\alpha}{2} \rho_\alpha^2 \right] + T \sum_{<i,j>} r_{ij} \tag{1.2}$$

Greek letters are taken to index cells while ρ_α and A_α denote the perimeter and apical cell area of cell α respectively. Tissue geometry was assumed to change adiabatically and thus cells remain in mechanical equilibrium while the underlying model parameters evolve. Cell divisions were introduced at random with stochastic, uniformally distributed orientations. This model was utilized to estimate average values for each parameter by comparison with the distribution of cell neighbor number and apical areas as well as validated using laser ablation data. As such, Farhadifar et al.[52] not only demonstrated that these vertex models could recapitulate the geometry of in-vivo cell packings resultant from growth, but also were the first to estimate vertex model parameters quantitatively. Rauzi et. al [146] extended Eq. 1.2 to include effects of spatial anisotropy allow by defining junctional parameters to be explicit functions of orientation - e.g. $T_{ij} = T(\theta_{ij})$. This generalization is sufficient to generate the morphogenetic flow observed in the convergent extension of the germ band of the Drosophila embryo [146].

Vertex models have been also been utilized to address the fundamental question of what controls the final size of limbs and organs. It is widely thought that morphogen gradients must regulate final size by patterning cell proliferation rates, either through its gradient or morphogen concentration [41]. However, such models have a hard time explaining the uniform growth and synchrony of arrest upon completion of growth observed in systems like the developing Drosophila wing. Mechanical feedback on proliferation rates has been proposed as an alternative [159]. To quantitatively study if this effect could explain the dynamics of growth in the Drosophila wing, Hufnagel et. al [80] generalized the traditional planar vertex model to include the 3D effects of cell apico-basal height. Growth occurs over the course of days while mechanical equilibration of the actin cytoskeleton appears to occur on the time-scale of seconds. As such, it is reasonable to assume shape adiabatically evolves along the manifold of mechanical equilibrium states. Thus, Hufnagel et al. assumed instantaneous epithelial geometry minimized the following energy

$$E\left[\boldsymbol{r}_i, h_\alpha\right] = \sum_\alpha \rho_\alpha + a\left[A_\alpha h_\alpha - V_0\right]^2 + \sum_{\{\beta\}_\alpha} b\left[h_\alpha - h_\beta\right]^2 + c\left[h_\alpha - 1\right]^2 \qquad (1.3)$$

h_α denotes the apico-basal height of cell α. The actin cytoskeleton only appears in this equation as a uniform surface tension term that is imagined to act on the surface of each elastic cell. Allowing cells to divide (T3) at random with probability proportional to the morphogen concentration and dependent on their state of stress, the vertex model predicts a novel mechanism for final size determination of the wing; once the edge of the wing falls below a morphogen threshold, it stops growing and effectively arrests the bulk of the disk through mechanical feedback.

Vertex models have proven invaluable in deciphering the pattern of cellular mechanics required to drive different morphogenetic movements observed in a multitude of model organisms. However, such models have been limited to phenomenological descriptions of stress with no connection to cytoskeletal proteins and their dynamic regulation. Hufnagel et al. [80] demonstrated that vertex models can be used to probe the macroscopic consequences of mechanical feedback on growth at the cellular-scale. We look to continue this approach and model both the explicit effects of myosin activity and mechanical feedback on the cytoskeleton. Can we begin to connect phenomenological parameters within the vertex model to the active regulation of cytoskeletal proteins? Explicit multi-scale modeling tested against empirical data is required to make sense of the interplay between cellular activity and tissue mechanics.

1.3 Experimental assays of cellular mechanics

Measuring the state of stress of a developing tissue presents a considerable experimental challenge. This section will provide a brief description of the currently available techniques used to assay cellular mechanics within a confluent layer of cells. We note that many sophisticated techniques exist to measure forces of in-vitro cell cultures. For example, Traction Force Microscopy (TFM) has proven immensely useful to understanding the distribution of forces at play during cell migration [117]. To perform TCM, cells are cultured on a synthetic, deformable ECM laced with fluorescent beads that serve as fiduciary markers for substrate displacement [45]. The substrates used are known linear isotropic elastic materials, such as silicone, and thus stress applied on the synthetic ECM by the confluent cell layer can be easily obtained from the displacement field of the beads [151]. However, it is known that cells actively change their mechanical state in response to developmental signals. If one is interested in developmental dynamics, it is not enough to measure cell stiffness in a plate. We need to measure the effective constitutive relationships in the presence of relevant biochemical feedbacks and morphogenetic signals. As such we focus our remaining attention on in-vivo measurements.

The most common method for measuring in-vivo stress is laser micro-ablation. This method originated as a surgical procedure; a macroscopic incision was made using a scalpel to measure the retraction/extension velocity of the resultant wound [12]. Retraction or extension implied the original tissue was respectively under tensile or compressive loading. The technique has shrunk to sub-cellular length scales, trading the scalpel for focused UV laser light that 'cuts' the cytoskeletal bundle abutting a cell-cell interface [104]. The resultant retraction velocity is used as a proxy for the cortical tension that was in the pre-cut actin cytoskeleton. Laser ablation has proved incredibly useful; the technique was central in the discovery that anisotropic tension in the Drosophila lateral ectoderm drives cell intercalation during germ-band extension [146] and that dorsal closure is driven by supracellular myosin cables [89]. Unfortunately, it is clearly a destructive procedure that greatly perturbs the sample, allowing the experimentalist only local snapshots of subcellular stress. Furthermore, one needs highly time-resolved movies to meaningfully measure the retraction velocity.

Recently, experimentalists have utilized optical tweezers to quantitatively probe stress at the subcellular scale. These experiments leverage the fact that dielectric beads under focused light of graded intensity are subject to an effective force pushing it towards the high intensity region [164]. This method has proven useful for measuring the rheology of actomyosin bundles of cellular interfaces. In the Drosophila embryo, it was shown that the average cortical tension along interfaces was on the order of 100 pN and that tension equilibrates on the time-scale of a few seconds, incredibly fast compared to the hour/day timescale of morphogenesis [8]. Interestingly, this is entirely consistent with the estimated 50 motors that participate in actin contraction [142] are at stall (recall the stall force was measured to be roughly 2 pN/motor). We will return to this idea in Chapter 2. Unfortunately, this method is difficult to calibrate and execute, and as with laser ablation, only provides information about stress at the junctional level.

Campas et al. measure stress in-situ [24] by introducing oil microdroplets the size of single cells into the confluent cell layer to act as a force transducer. Specifically, the surface of the droplet is coated with adhesive molecules to permit binding between the oil droplet and neighboring cells. The three dimensional geometry is reconstructed for each microdroplet and deformations from a spherical shape are utilized to infer the anisotropic forces applied on the droplet by the surrounding tissue. As mechanical properties of the oil are explicitly measured, all measurements are made in absolute units. This method has recently been generalized to include ferrofluidic droplets that can act as micro-mechanical actuators [154]. This method allows one to probe tissue mechanics at larger length-scales then both micro-ablation or optical tweezers by the addition of multiple droplets. Unfortunately, experimentalists still must sparely sample to ensure the mechanical state of the tissue is unperturbed [24].

Additionally, there have been recent developments that seek to leverage the prevalence of florescence microscopy and measure stress purely visually. The most direct of these methods utilizes FRET (Forster resonance energy transfer) tension sensors embedded within molecular elements of interest [116]. A FRET sensor consists of two florophores, aptly termed a donor and acceptor. The donor florophore is chosen so that its excitation spectrum overlaps with the absorption spectrum of the acceptor. As it is dependent on dipolar interactions, energy transfer drops off like R^{-6} where R is the distance between donor and acceptor [74]. This concept is turned into a force tensor by connecting the donor and acceptor elements with an elastic polymer of known stiffness [114]. In principle, measuring the ratio of emitted frequencies of the donor and acceptor florophore can be used to measure the extension of the elastic polymer and thus the force applied to the FRET sensor. Such tension sensors have been successively embedded into vinculin [65] and cadherin molecules [17] (both critical components of AJs) in-vitro, as well as in live drosophila ovaries [23]. Unfortunately, the method is difficult to calibrate, relying on in-vitro techniques to estimate the FRET efficiency to force relationship. As such, it is not quantitative. As a result, the relationship between traction exerted across adhesive bonds and cortical tension, a critical quantity for morphogenesis, remains unknown.

1.4 Image-based inference of cellular mechanics

Despite the advances made by the methods presented in the above section, there is still no satisfactory experimental tool to quantitatively measure the distribution of stress throughout a tissue over the course of development. This raises an important question: how are we to investigate the interplay between mechanics and cytoskeletal regulation within a developing epithelial monolayer if one of the critical fields remains opaque to us? Short of direct measurement, progress can be made using model-driven inference. Hence, in recent years researchers have developed many 'image-based' tools that allow one to infer mechanics based solely upon cellular geometry, *conditioned* on a chosen model of cell mechanics.

In 2010, Brodland et al. formulated "Video Force Microscopy" which partitions the forces acting within an epithelial tissue into 'active' stresses localized along cell boundaries and 'passive' stresses that deform the cytoplasm [20]. All tricellular junctions are dynamically tracked and assumed to move due to viscous forces. Finite element methods are utilized to calculate the passive forces needed to deform the cytoplasm as was observed in the course of the movie. Both are integrated to estimate the 'active' junctional forces. "Video Force Microscopy" has been applied to Drosophila embryos undergoing ventral furrow formation to show the movement must be driven by apical constriction and basal contractions of the ectoderm [20].

A complementary method, originally proposed by Chiou et al. [29] and later extended [83], models the epithelial cell array as a two-dimensional vertex model in equilibrium.

Chiou et al. demonstrate that the differential form of any two-dimensional vertex model can be generically written

$$dE[\{dr_{ij}\}, \{dA_\alpha\}] = \sum_{<i,j>} T_{ij} dr_{ij} + \sum_{\alpha} p_\alpha dA_\alpha \tag{1.4}$$

As eq. 1.4 defines tension and pressure as conjugate to edge length and polygonal area, mechanical equilibrium is equivalent to the constraint of force balance imposed on vertices

$$\boldsymbol{F}_i = \sum_{\{j\}_i} T_{ij} \hat{\boldsymbol{r}}_{ji} + \frac{P_\alpha - P_\beta}{2} \left[\hat{\boldsymbol{z}} \wedge \boldsymbol{r}_{ji}\right] = 0 \tag{1.5}$$

$\hat{r}_{ji}$ denotes the unit vector pointing to vertex j from i, and P_α, P_β denote the cells separated by edge i, j. Eq. 1.5 is a linear system of equations for parameters $\{T_{ij}\}, \{P_\alpha\}$ and thus can be inverted using the static geometry of cells. Simple graph-theoretic counting (using Euler's formula) proves such an inverse is underdetermined for a planar array due to the lack of knowledge about the boundary conditions and thus the parameters can only be partially determined. Furthermore, the inverse is plagued by sensitivity to noise [29]. Despite its limitations, the "Mechanical Inverse" algorithm has proven useful in interpreting in-vivo data when compared to micro-ablation data [82]. In Chapter 5 we will re-formulate this problem to mitigate both of these issues.

Of course, the 'measured' stresses are only as valid as the chosen model of cell mechanics, of which there is still no consensus. The results from above *in-silico* methods must be cross-validated by comparison to one of the methods outlined above or supplemented with phenomenological correlations before they can be taken seriously. That said, image-based techniques currently provide the best path towards realizing the biological ‘diagram of forces’ as originally conceptualized by D’Arcy Thompson. Furthermore, the map of stresses within the embryo provides us a quantitative method to test our models.

1.5 Outline of the dissertation

The remainder of this dissertation will formulate a phenomenological model that incorporates the effects of actomyosin activity within the cytoskeleton and cadherin mediated adhesion on the mechanics at the cellular and tissue scale. Critically, we model the simultaneous dynamics and interplay between mechanics, cytoskeletal activity, and cell morphology. We obtain explicit relations between all three phenomenological fields. At every step, quantitative predictions from the model are tested against live-imaging data to lend strong support to its underlying assumptions. After we show the model is an accurate representation of in-vivo tissue mechanics, we use it to improve upon past attempts at measuring epithelial stress from just images of cellular morphology. We expect this method to become immediately useful to researchers hoping to disentangle an organism’s form, the ‘diagram of forces’, and expression patterns of cytoskeletal proteins.

Chapter 2 formulates the basic components of the Active Tension Network (ATN) model of epithelial morphogenesis. Generalizing the vertex model, we assume that the mechanical balance of cells within a tissue is dominated by cortical tension and introduce tension-dependent active remodeling of the cortex. We find that ATNs exhibit unusual mechanical properties. Specifically, an ATN behaves as a fluid at short times, but at long times supports external tension like a solid. Furthermore, an ATN has an extensively degenerate equilibrium mechanical state associated with a discrete conformal - “isogonal” - deformation of cells. The equilibrium mechanical state is parameterized by a rigid ‘tension-triangulation’. The ATN model predicts a constraint on equilibrium cell geometries, which we demonstrate to approximately hold in certain epithelial tissues. We further show that isogonal modes are observed in the Drosophila embryo, accounting for the striking variability of apical areas of ventral cells and helping understand the early phase of gastrulation.

Chapter 3 relaxes the original assumption that all cells have constant pressure introduced in Chapter 2. In doing so, we generalize the ‘tension triangulation’, giving us a bijective mapping between equilibrium epithelial cell morphology and the ‘diagram of forces’ D’Arcy Thompson originally conceptualized. This framework should allow one to easily measure arbitrary distributions of stress within two-dimensional networks. We leverage the existence of the generalized dual triangulation to formulate a robust, local “Mechanical Inverse” algorithm that allows one to infer network level mechanics from an image of cell morphology. The inference algorithm is verified in-vivo both at the cellular scale and organismal scale using Drosophila live image data.

Chapter 4 extends the ATN model in Chapter 2 to include positive feedback between myosin and cortical tension, as well as to include the effects of traction-dependent regulation of E-cadherin within AJs. With these simple additions to the model, we recover the morphological transition caused by cell intercalation observed during the convergent extension of the lateral ectoderm in Drosophila melongaster. Predictions from the model are checked using data kindly provided by the Lecuit lab [146].

Chapter 5 leaves the world of individual cells and moves towards a mesoscopic (patches of many cells) description of morphogenesis. To do so, we coarse-grain the linearized discrete model presented in Chapter 2. On this length and time scale, the model predicts epithelial tissues should behave as a viscious, slightly compressible fluid (akin to honey) driven internally by the global imbalance of myosin motors. We quantitatively check this intuition against *in-toto* imaging of the first few couple hours of embryogenesis in Drosophila melongaster. Specifically, the coarse-grained ATN model can predict morphological flow solely from the distribution of myosin. The data analysis pipeline presented in this section should be general to arbitrary developing systems.

Finally, Chapter 6 serves as a conclusion and presents the future outlook of the contained work. We believe the next logical step beyond the work presented in this dissertation is to couple the mechanics driving cellular rearrangements to the concomitant patterning of cell fate induction. The duality between equilibrium cellular tessellations and stress triangulations provides a useful parameterization of cellular morphogenesis, in a cell-specific fashion, that should immediately applicable to models of the interplay between cellular patterning and mechanics. To close out, we suggest that development of the chick cochlea provides an excellent entry point into the study of such models.

Chapter 2

Active Tension Network model of epithelial morphogenesis

As we stressed in Chapter 1, mechanical interactions play a crucial role in epithelial morphogenesis, yet understanding the complex mechanisms through which stress and deformation affect cell behavior remains an open problem. In this chapter, we formulate and analyze the Active Tension Network (ATN) model, which assumes that the mechanical balance of cells within a tissue is dominated by cortical tension and introduces tension-dependent active remodeling of the cortex. We find that ATNs exhibit unusual mechanical properties. Specifically, an ATN behaves as a fluid at short times, but at long times supports external tension like a solid. We call such materials 'active solids.' Furthermore, an ATN has an extensively degenerate equilibrium mechanical state associated with a discrete conformal - "isogonal" - deformation of cells. The ATN model predicts a constraint on equilibrium cell geometries, which we demonstrate to approximately hold in certain epithelial tissues. We further show that isogonal modes are observed in the fruit fly embryo, accounting for the striking variability of apical areas of ventral cells and helping understand the early phase of gastrulation. All experimental data of ventral cells was taken by collaborator Sebastian J. Streichan (KITP, UCSB).

2.1 Formulation of model

As described in Chapter 1, epithelial monolayers are often approximately represented by two-dimensional polygonal tilings, parameterized by a set of vertex coordinates $\{\boldsymbol{r}_i\}$ and are often described by Vertex Models [77, 52] which assume that the geometry of cells minimizes mechanical energy defined in terms of cell edge lengths ($r_{ij} = |\boldsymbol{r}_i - \boldsymbol{r}_j|$) and cell areas ($A_\alpha$). We begin this chapter by introducing a generalized class of vertex models by adding internal variables to capture the active adaptation of the cytoskeleton. We begin by defining mechanical energy in its differential form [29]

$$dE[\{\boldsymbol{r}_i\}] = \sum_{<i,j>} T_{ij}\, dr_{ij} + \sum_{\alpha} p_\alpha\, dA_\alpha \tag{2.1}$$

where tension, T_{ij}, defines the change in mechanical energy in response to a change of edge length (dr_{ij}) and the 2D 'apical pressure', p_α, defines the response to a change in cortical area (dA_α). Tension Nets correspond to the situation where pressure differentials between neighboring cells are negligible so that mechanical balance is dominated by cortical tension. In this limit $p_\alpha \approx p_0$ with p_0 controlling the total area of cells, and preventing the collapse of the network under the action of tension.

Vertex dynamics is relaxational and is given by

$$\nu \frac{d}{dt}\boldsymbol{r}_i = -\partial_{\boldsymbol{r}_i} E = \sum_{\{j\}_i} T_{ij}\hat{\boldsymbol{r}}_{ji} = \sum_{\{j\}_i} \boldsymbol{T}_{ij} \tag{2.2}$$

where $\{j\}_i$ denotes the set of all vertices connected to vertex i, $\hat{\boldsymbol{r}}_{ji}$ is a unit vector in the direction from $\boldsymbol{r}_i$ to $\boldsymbol{r}_j$, and ν represents the effective friction between apical cytoskeleton and its substrate [106] which determines the timescale of mechanical relaxation. Mechanical equilibrium of a Tension Net is reached when tensions balance, which geometrically means that for each vertex i, the three corresponding tension vectors $\boldsymbol{T}_{ij}, \boldsymbol{T}_{ik}, \boldsymbol{T}_{il}$ form a triangle. Since adjacent vertices share an edge, global tension balance implies that the set of T_{ij}'s defines a triangulation as shown in Fig. 2.1 a,b [113, 75].

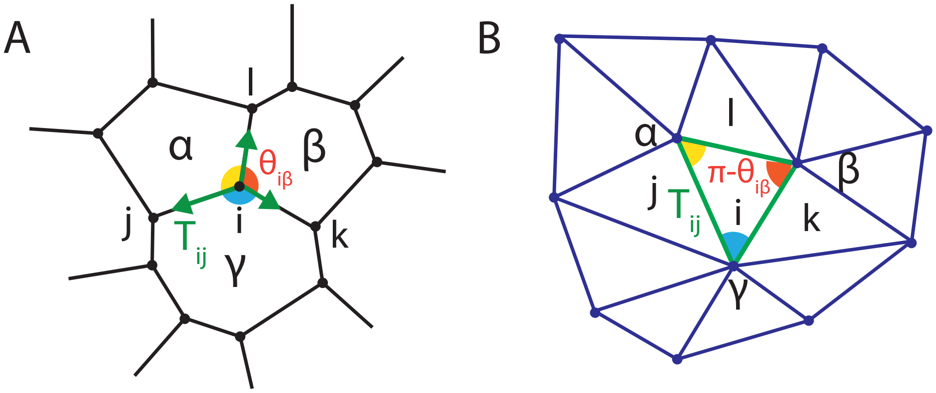

Figure 2.1: Force balance in a tension net defines a triangulation of the “tension plane”. (A) 2D array of cells represented by a polygonal tiling. In mechanical equilibrium tensions balance at each vertex. (B) Equilibrated tensions form a triangulation, with triangle angles supplementary to the angles at the corresponding vertex.

Microscopically, each edge in this network represents the mechanically coupled actomyosin bundles of neighboring cells, connected to each other via adherens junctions along the cell-cell interface, as shown schematically in Fig. 2.2a. Vertices serve as physical barriers to the lateral movement of cadherin clusters and contracting actomyosin bundles

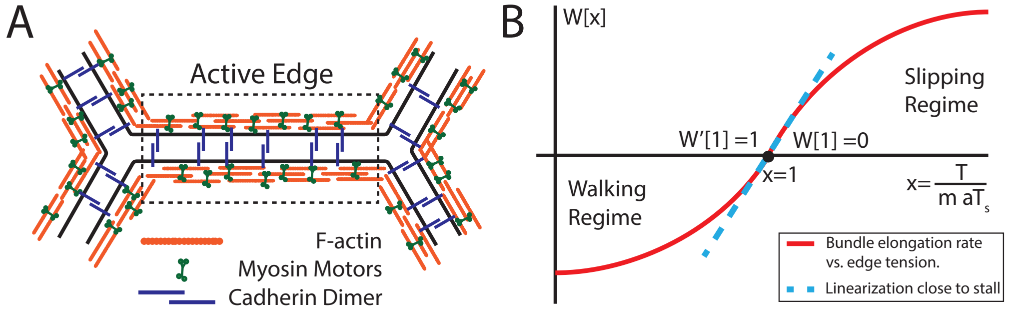

Figure 2.2: Role of myosin motors in the ATN model. (A) Schematic of the basic active element of a tension network: actomyosin cables on apposing interfaces are cross-linked by cadherin dimers; (B) Dependence of the actomyosin bundle contraction rate on mechanical load: the "walking kernel" $W(x)$, see Eq. 2.3, changes sign from contraction to elongation when mechanical load per myosin T/am exceed the stall load T_s.

[30, 27]. The coupled actomyosin bundles along the cell edge form a natural mechanical unit - an "active edge" in Fig 2.2a - which carries tension. Edge tension, T_{ij}, depends on the edge length r_{ij} as well as on the intrinsic variables representing the local state of the actomyosin bundle and cadherin-mediated adhesion between cells. Specifically, we assume a simple elastic form, $T_{ij} = K(r_{ij} - \ell_{ij})$, parameterizing the internal state of each interface by an intrinsic "rest length" ℓ_{ij} of the underlying actomyosin filament, itself a dynamical variable governed by

$$\ell_{ij}^{-1} \frac{d}{dt} \ell_{ij} = \tau_\ell^{-1} W \left[\frac{T_{ij}}{m_{ij} a T_s} \right] \tag{2.3}$$

The generic features of the "walking kernel" $W[x]$, illustrated in Fig. 2.2b, are based on single-molecule experiments [34, 127] previously described: myosin motors can walk, contracting the actin bundle, unless the load per myosin, T_{ij}/am_{ij}, reaches the "stall force" level T_s, above which the filament elongates as motors slip backwards [90]. Here m_{ij} is the average myosin line-density along the edge and a is the length scale over which motors share mechanical load.

Eqs. 2.2, 2.3 define the dynamics of a Tension Net with a specified myosin distribution on interfaces. The fixed point of these equations is reached when i) tensions balance at all vertices and ii) all edges are at their stall tension, set by the local myosin (linear) density ($T_{ij} = aT_s m_{ij}$). Global tension balance requires the set of T_{ij}'s to form a triangulation and therefore edge tensions, and hence myosin levels, cannot be prescribed independently. How can mechanical equilibrium be achieved? At this point we recall that myosin distribution within tissues is not fixed and is known to respond to mechanical cues, although the exact form of this mechanical feedback is not fully understood [53, 137]. Here we propose a particular form of mechanical feedback on myosin, that will ensure convergence to a balanced state. The latter is achieved if myosin recruitment depends on the internal strain rate of each filament:

$$m_{ij}^{-1}\frac{d}{dt}m_{ij} = \alpha \ell_{ij}^{-1}\frac{d\ell_{ij}}{dt} \tag{2.4}$$

with α parameterizing the rate of myosin recruitment, which we assume to be slow relative to both mechanical relaxation and actomyosin contractility. This form of mechanical feedback recruits myosin to overloaded slipping bundles and reduces myosin on underloaded contracting bundles until the stall condition is reached, bringing the system to equilibrium. The "Dynamic Recruitment" hypothesis, defined by Eq 2.4, is dictated by the requirement of ATN stability and should be regarded as a prediction of the model to be tested by future experiments.

2.2 Equilibrium properties of model: Isogonality and Geometric compatibility

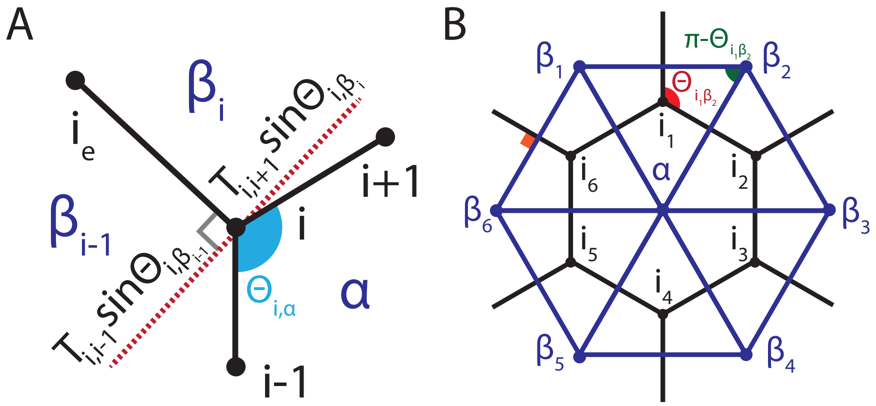

Figure 2.3: (a) Mechanical balance of a tension net implies that at vertex i, $T_{i,i-1}\sin(\theta_{i,\beta_{i-1}}) = T_{i,i+1}\sin(\theta_{i,\beta_i})$, as tensions must balance along the direction perpendicular to the edge external to cell α. This construction can be repeated on all vertices of cell α. The circular product of such ratios around a cell is defined as the 'compatibility condition'. (b) A diagram representing both the notation used to define the compatibility constraint and the "dual triangulation" of the tension plane which corresponds to the tension balanced state. Edges of the $\alpha\beta_1\beta_2$ triangle represent tensions that balance at vertex i_1, while angles (of the triangle) are complementary to the angles of the corresponding vertex of the polygonal cell array (e.g. $\angle\alpha\beta_2\beta_1 = \pi - \theta_{i_1\beta_2}$).

The 'duality' between an equilibrium tension net and the corresponding triangulation of the tension plane (see Fig. 2.1ab) implies the existence of certain constraints on cell geometry. In this section, we explicitly construct the tension triangulation, as well as derive the geometric constraint for an arbitrary cell array to be compatible with tension balance. Consider vertex 'i', depicted in Fig. 2.3a, formed by the triplet of cells $(\alpha, \beta_{i-1}, \beta_i)$. Force balance at this vertex is written

$$T_{i,i_e}\hat{\boldsymbol{r}}_{i_e,i} + T_{i,i+1}\hat{\boldsymbol{r}}_{i+1,i} + T_{i,i-1}\hat{\boldsymbol{r}}_{i-1,i} = 0 \tag{2.5}$$

Projecting this equation onto the red-line as shown in Fig 2.3a

$$T_{i,i+1}\left[\hat{\boldsymbol{r}}_{i_e i}\wedge\hat{\boldsymbol{r}}_{i_+ i}\right]=T_{i,i-1}\left[\hat{\boldsymbol{r}}_{i_- i}\wedge\hat{\boldsymbol{r}}_{i_e i}\right]\implies\frac{T_{i,i+1}}{T_{i,i-1}}=\frac{\sin\left(\theta_{i,\beta_{i-1}}\right)}{\sin\left(\theta_{i,\beta_i}\right)}\tag{2.6}$$

This construction can be done for each vertex belonging to a cellular plaquette. Indexing vertices belonging to cell α using a CCW convention with $i\in\{1,2,...,z_\alpha\}$, as shown in Fig. 2.3b, we take the circular product around the cell and define the "geometric compatibility" measure χ_α

$$\chi_\alpha=\prod_{i=1}^{z_\alpha}\frac{\sin\left(\theta_{i,\beta_i}\right)}{\sin\left(\theta_{i,\beta_{i-1}}\right)}=\prod_{i=1}^{z_\alpha}\frac{T_{i,i-1}}{T_{i,i+1}}=1\tag{2.7}$$

The circular product over the ratios of tensions is a telescoping product and thus is equal to one for a static tension net, which we call the compatibility condition. An array with all $\chi_\alpha=1$ is geometrically *compatible* with tension-balance. Since χ_α can be readily measured, the compatibility constraint allows one to quantitatively assess whether a given cell array is consistent with a balanced tension net.

A corollary to the compatability condition is that tensions form a triangulation 'dual' to the cell array. Once again, we consider force-balance at vertex 'i', but this time rotated by $\pi/2$

$$\hat{\boldsymbol{z}}\wedge\left[T_{i,i_e}\hat{\boldsymbol{r}}_{i_e,i}+T_{i,i+1}\hat{\boldsymbol{r}}_{i+1,i}+T_{i,i-1}\hat{\boldsymbol{r}}_{i-1,i}\right]=\boldsymbol{q}_{\beta_{i-1}\beta_i}+\boldsymbol{q}_{\beta_i\alpha}+\boldsymbol{q}_{\alpha\beta_{i-1}}=0\tag{2.8}$$

where $\boldsymbol{q}_{\alpha\beta_{i-1}},\boldsymbol{q}_{\beta_i\alpha},\boldsymbol{q}_{\beta_{i-1}\beta_i}$ are vectors that make up edges of the triangle dual to vertex i, shared by cells $\alpha,\beta_i,\beta_{i-1}$. We have $\boldsymbol{q}_{\alpha\beta}=\boldsymbol{Q}_\alpha-\boldsymbol{Q}_\beta$ where $\boldsymbol{Q}_\alpha$ denotes the vertex of the dual triangulation that corresponds to cell α. Summing around vertices belonging to a cellular plaquette will cancel out internal dual vectors and leave us with

$$\sum_i \boldsymbol{q}_{\beta_{i-1}\beta_i} = 0 \tag{2.9}$$

Thus, the outside edges of all triangles made from tensions acting at vertices around a cell must form a *closed polygon*, ensuring that we can build a closed triangulation out of tensions. This is equivalent to the constraint that $\sum_i \theta_{i,\alpha} = 2\pi$. One can then see that the compatibility constraint is simply the law of sines applied to triangles around the plaquette! Specifically, we note that if $\theta_{i\beta}$ is the angle at vertex i belonging to cell β; its complement $\pi - \theta_{i\beta}$ is the corresponding angle of the dual triangle in the tension plane (Fig. 2.1ab). By applying the law of sines to the triangles surrounding dual vertex α one rederives the compatibility condition. It is important to note that this construction only defines the triangulation up to a scale reflecting the fact that at equilibrium, all tensions are only known up to an overall multiplicative factor.

The compatibility constraint is a necessary condition for mechanical equilibrium under conditions of tension dominance. Its failure would imply either that (i) the tissue is not in mechanical equilibrium or that (ii) forces other than cortical tension contribute significantly to the balance. Observed fluctuations make it clear that mechanical equilibrium can only be approximate. Note, that while being necessary, the compatibility constraint is not sufficient to conclude tension balance. E.g. it is conceivable that cell array has “compatible geometry” for a reason other than tension-net equilibrium, however, we are not aware of any alternative simple physical mechanism that would explain this geometry.

The geometry of the dual triangulation also constrains possible sets of balanced tensions. A triangulation is specified by the positions of its c (the number of polygonal cells in the array) vertices, and hence has $2c$ independent degrees of freedom. This number is smaller than the number of edges $e = 3c$ (assuming all vertices in the cell array are three-fold), which means that T_{ij}'s can't be prescribed independently: the balanced set satisfies c constraints.

The above counting argument further implies that the map between cell geometry and tension triangulation is highly degenerate. The number of degrees of freedom of a compatible cell array is given by $2v - c = 3c$ (v being the number of vertices of the cell array), which is c degrees of freedom larger than that of the dual triangulation. Hence, a given set of balanced tensions corresponds to a manifold of nets with one degree of freedom per cell. Specifically, as long as none of the vertex angles are perturbed, we can freely "inflate" or "deflate" cells, as illustrated in Fig. 2.4a, with no cost of energy and thus without disturbing mechanical equilibrium and the underlying tension triangulation. Quite generally such angle preserving - hereafter referred to as "isogonal" deformations have the form

$$\delta \boldsymbol{r}_i = S^{-1}_{\alpha\beta\gamma}[\boldsymbol{T}_{ij}\Theta_\beta + \boldsymbol{T}_{ik}\Theta_\alpha + \boldsymbol{T}_{il}\Theta_\gamma] \tag{2.10}$$

where $\delta \boldsymbol{r}_i$ denotes the displacement of vertex i shared by cells α, β, γ and $S_{\alpha\beta\gamma}$ (Fig. 2.1ab) is the area of the vertex's dual triangle. $\{\Theta_\alpha\}$ parameterize the c-dimensional manifold of equilibrim states. Tensions $\{\boldsymbol{T}_{ij}, \boldsymbol{T}_{ik}, \boldsymbol{T}_{il}\}$ capture the implicit geometric constraints within tension nets central to the structure of the isogonal modes: note for

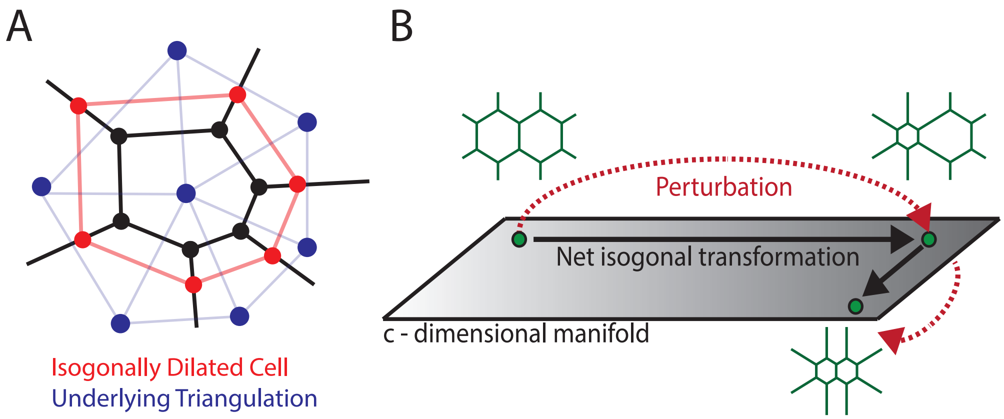

Figure 2.4: The equilibrium manifold of an ATN. (a) Cartoon of an *isogonal* 'breathing mode' of a cell in a tension net. (b) Because ATN equilibrium is a manifold rather than a point, after a transient perturbation the system does not necessarily return to the same state, resulting in an 'isogonal' transformation.

example that $\delta \boldsymbol{r}_i = 0$ for $\Theta_\alpha = \Theta_\beta = \Theta_\gamma$. The compatibility condition (see Eq. 2.7) satisfied by equilibrium tension nets is essential for allowing such isogonal modes to exist. Because they do not invoke a restoring force, isogonal deformations are easily excitable "soft modes" and are expected to dominate observed fluctuations of tension nets close to mechanical equilibrium. We note that isogonal modes can be thought of as a discrete manifestation of the conformal symmetry that appears in 2D continuum elasticity in the limit of a vanishing bulk modulus. Isogonal modes also generalize the isoperimetric "breathing modes" of a hexagonal lattice [172].

2.3 Linear Response of a 1D Active Tension Chain

Let us now consider the dynamics of small perturbations around a mechanical equilibrium state, which can be described by linearizing Eqs. 2.2-2.4. Before the full detailed calculations are carried out in the next section, the key features can be understood from a vastly simpler analysis of a 1D "Active Tension Chain" model analyzed here.

Starting from Eqs 2.2-2.4 and specializing to a one-dimensional *uniform* cable of active-elements, the linearized equations for small perturbations arond a given fixed point become

$$\begin{aligned}
\frac{d}{dt}\,\delta r_n &= \nu^{-1}K\bar{\ell}\left[\delta u_n - \delta u_{n-1}\right] \\
\frac{d}{dt}\,\delta u_n &= \nu^{-1}K\left[\delta u_{n+1} + \delta u_{n-1} - 2u_n\right] - \frac{l_0 W'[1]}{\tau_\ell u_0}(\delta u_n - \delta m_n) \\
\frac{d}{dt}\,\delta m_n &= \alpha\tau_\ell^{-1}W'[1]\left(\delta u_n - \delta m_n\right)
\end{aligned} \tag{2.11}$$

We've defined 1D strain $u_n \equiv (r_{n,n+1} - \ell_n)/\bar{\ell} = T_n/K\bar{\ell}$ where $r_{n,n+1} = r_{n+1} - r_n$ the length of the edge between vertices r_{n+1} and r_n and $\bar{\ell}$ is the mean intrinsic length. We have rescaled $m \to \frac{aT_s}{K\bar{\ell}}m$ to make it dimensionless. In the continuum limit, these transform to

$$\partial_t \begin{pmatrix} \delta r \\ \delta u \\ \delta m \end{pmatrix} = \begin{pmatrix} 0 & \nu^{-1}K\bar{\ell}^2\partial_x & 0 \\ 0 & \nu^{-1}K\bar{\ell}^2\partial_x^2 - \kappa & \kappa \\ 0 & \bar{\alpha} & -\bar{\alpha} \end{pmatrix} \begin{pmatrix} \delta r \\ \delta u \\ \delta m \end{pmatrix} \tag{2.12}$$

x denotes the coordinate along the cable. Furthermore we've defined $\kappa \equiv \frac{\bar{\ell}W'[1]}{\tau_\ell u_0}$ and $\bar{\alpha} = \alpha\tau_\ell^{-1}W'[1]$. As was expected, all elements of the first column of the matrix are zero, implying that δr displacements along the cable are zero modes and that their associated dynamics is slaved to the dynamics of tension and myosin perturbations. Hence, we focus on the reduced myosin/tension system in Fourier space (define $D \equiv \nu^{-1}K\bar{\ell}^2$)

$$\partial_t \begin{pmatrix} \tilde{u} \\ \tilde{m} \end{pmatrix} = \begin{pmatrix} -Dk^2 - \kappa & \kappa \\ \bar{\alpha} & -\bar{\alpha} \end{pmatrix} \begin{pmatrix} \tilde{u} \\ \tilde{m} \end{pmatrix} \tag{2.13}$$

The exact dispersion relation for both branches is

$$\lambda_{1,2} = -\frac{Dk^2+\bar{\alpha}+\kappa}{2}\left[1 \pm \sqrt{1-\frac{4\bar{\alpha}Dk^2}{(Dk^2+\bar{\alpha}+\kappa)^2}}\right] \tag{2.14}$$

Assuming mechanical feedback occurs on a slower time-scale than actomyosin contractility ($\frac{\bar{\alpha}}{\kappa} << 1$) we can expand each dispersion relation to linear order in $\frac{\bar{\alpha}}{\kappa}$

$$\lambda_{1,2} \approx -\left[Dk^2+\kappa+\frac{\bar{\alpha}\kappa}{Dk^2+\kappa}\right], -\frac{\bar{\alpha}Dk^2}{Dk^2+\kappa} \tag{2.15}$$

We immediately see that first branch is gapped by κ while the second branch is acoustic, corresponding to fact that a global rescaling of tension and myosin along the cable does not perturb the underlying force balance or stall condition and thus there are phonons at long times and length scales effectively behaving as a solid! The eigenvectors are

$$\phi_{1,2} \approx \begin{pmatrix} Dk^2+\kappa \\ -\bar{\alpha} \end{pmatrix}, \begin{pmatrix} \kappa \\ Dk^2+\kappa \end{pmatrix} \tag{2.16}$$

For $\bar{\alpha}=0$ the gapped mode corresponds solely to tension perturbations that exponentially localize within a length scale $\sqrt{D/\kappa}$ - at short times isogonal/fluid deformations will occur within this 'droplet'. This recapitulates a passive Maxwellian viscoelasticity. Conversely, for $0<\bar{\alpha}<<\kappa$, the gapped mode is an admixture between both tension and myosin perturbations along the cable. Taken together, Eqns. 2.15,2.16 exhibit exotic behavior, we call an 'Active Solid'. At long wavelengths, and thus small k, only the acoustic branch is non-zero. The spring constant of this mode is the second derivative of the dispersion relation at $k=0$ and thus $K_{eff}=\bar{\alpha}\kappa^{-1}D$ as reported.

To gain further insight into the rheology of this material, we now study Eq. 2.13 under sinusoidal forcing on the boundary. We expand tension along the cable in a Fourier sine series

$$u = u_0 + u_\Delta \left(\frac{x}{L}\right) + \sum_{q=1}^{\infty} \tilde{u}_q \sin\left(\frac{q\pi x}{L}\right) \tag{2.17}$$

We are only interested in symmetric longitudinal pulling and thus set $u_\Delta = 0$. A similar decomposition exists for myosin line density m

$$i\omega\, \bar{u}_q + \left(D\frac{q^2\pi^2}{L^2} + \kappa\right)\bar{u}_q - \kappa\bar{m}_q = \frac{(1-(-1)^q)}{\pi q}\bar{F}_{ext}(\omega) = \bar{F}_q \tag{2.18}$$

$$i\omega\bar{m}_q + \bar{\alpha}\bar{m}_q - \bar{\alpha}\bar{u}_q = \frac{(1-(-1)^q)}{\pi q}\bar{M}_{ext}(\omega) = \bar{G}_q \tag{2.19}$$

F_{ext} and M_{ext} represent the time-dependent external force acting on the boundary of the 1D chain. The dynamic boundary conditions act as a source as expected (onto only the odd modes as they respect the left/right symmetry). Eq. 2.13 implies $\bar{m}_q = \frac{\bar{G}_q + \alpha\bar{u}_q}{\alpha + i\omega}$. Substituting this into the Eq. 2.17.

$$\bar{u}_q\left[D\frac{q^2\pi^2}{L^2} + \kappa\left(1 - \frac{\bar{\alpha}}{\bar{\alpha} + i\omega}\right) + i\omega\right] = i\omega\left[\bar{F}_q + \frac{\kappa}{\bar{\alpha} + i\omega}\bar{G}_q\right] \tag{2.20}$$

which can be simplified to obtain (we assume the forcing function on myosin is equivalent to the forcing function on tension)

$$\bar{u}_q(\omega) = -\frac{b^2(\omega)}{(\pi q)^2 + b^2(\omega)}\frac{(1-(-1)^q)}{\pi q}\bar{F}_{ext}(\omega) \tag{2.21}$$

where we defined $b^2(\omega) = i\omega L^2 D^{-1}\left[1 + \frac{\kappa}{\bar{\alpha}+i\omega}\right]$. The Fourier series over q can be resummed to give $\bar{u}(x,\omega)$ for $x \in [-L/2, L/2]$.

$$\bar{u}(x,\omega) = \frac{\cosh(\frac{bx}{L})}{\cosh(\frac{b}{2})}\bar{F}_{ext}(\omega) \tag{2.22}$$

This immediately implies the phase relationship between strain and the external force is

$$\bar{r}(\omega) = -\frac{ib^2 \cosh(\frac{bx}{L})}{\omega L^2 \cosh(\frac{b}{2})} \bar{F}_{ext}(\omega) \tag{2.23}$$

We note this has the an additional regime of behavior relative to passive materials. For $\omega << \bar{\alpha}$, the relationship is $\bar{r} \sim D^{-1}\left[1 + \frac{\kappa}{\bar{\alpha}}\right]\bar{F}$ and thus it behaves as a spring with stiffness $\frac{\bar{\alpha}D}{\kappa+\bar{\alpha}}$ as expected from our dispersion relation derived above. In other words, for slow perturbations we pull on the myosin feedback law! For $\bar{\alpha} << \omega << \kappa$ the relationship is $\bar{r} \sim \frac{i\kappa}{D\omega}\bar{F}$ and thus it behaves as a visco-elastic fluid, probing the gap between acoustic and optical branch. This regime is where isogonal deformations and localized stress patterns should exist. Lastly, if $\omega >> \kappa$ then $\bar{r} \sim D^{-1}\bar{F}$ - i.e. we are simply pulling on the elastic cytoskeletal network.

2.4 2D Active Tension Network is an 'active solid'

The two-dimensional dynamics near equilibrium is most naturally expressed in terms of edge vectors $\boldsymbol{r}_{ij}$. Equations of motion can be derived directly from Eq. 2.2-2.4 presented above. Hereafter time is rescaled $t \to \frac{K}{\nu}t$ to reduce the appearance of unnecessary constants.

$$\frac{d}{dt}\boldsymbol{r}_{ij} = \boldsymbol{u}_{i_1 i} + \boldsymbol{u}_{i_2 i} + \boldsymbol{u}_{jj_1} + \boldsymbol{u}_{jj_2} - 2\boldsymbol{u}_{ij} \tag{2.24}$$

where $\boldsymbol{u}_{ij} \equiv K^{-1}T_{ij}\hat{\boldsymbol{r}}_{ij} = u_{ij}\hat{\boldsymbol{r}}_{ij}$ and neighboring vertices of i are taken to be j, i_1, i_2. Parameterization in terms of edge vectors simplifies the resultant algebra at the cost of introducing $2c$ additional degrees of freedom associated to the geometric constraint that edge vectors sum to zero around each cellular plaquette

$$\sum_{<i,j>\in\mathcal{E}_\alpha} s^\alpha_{ij}\,\boldsymbol{r}_{ij} = 0 \quad \forall\alpha \tag{2.25}$$

$\mathcal{E}_\alpha$ denotes the set of all edges associated to cell α while $s^\alpha_{ij} = \pm 1$ if $\boldsymbol{r}_{ij}$ points counterclockwise or clockwise respectively. It is easy to check that dynamics described by Eq. 2.24 preserves the constraint defined by Eq. 2.25 - each vertex's equation of motion will appear in the sum twice with opposing signs. We linearize Eq. 2.24 and decompose each edge vector into transverse $\delta\theta_{ij}$ and longitudinal δr_{ij} components defined by

$$\delta\boldsymbol{r}_{ij} = \delta r_{ij}\,\hat{\boldsymbol{r}}_{ij} + r_{ij}\,\delta\theta_{ij}\,(\hat{\boldsymbol{z}}\wedge\hat{\boldsymbol{r}}_{ij}) \tag{2.26}$$

leaving us with equations

$$\frac{d}{dt}\delta r_{ij} = \sum_{<k,l>}\left[L_{ij;kl}\,\delta u_{kl} - A_{ij;kl}\,u_{kl}\delta\theta_{kl}\right] \tag{2.27}$$

$$r_{ij}\frac{d}{dt}\delta\theta_{ij} = \sum_{<k,l>}\left[A_{ij;kl}\,\delta u_{kl} + L_{ij;kl}\,u_{kl}\delta\theta_{kl}\right] \tag{2.28}$$

where we have defined

$$L_{ij;kl} \equiv \hat{\boldsymbol{r}}_{ij}\cdot\hat{\boldsymbol{r}}_{kl}\left[\mathcal{A}_{ki}\delta_{li} + \mathcal{A}_{lj}\delta_{kj} - \mathcal{A}_{li}\delta_{ki} - \mathcal{A}_{kj}\delta_{lj}\right] \tag{2.29}$$

$$A_{ij;kl} \equiv \hat{\boldsymbol{r}}_{ij}\wedge\hat{\boldsymbol{r}}_{kl}\left[\mathcal{A}_{ki}\delta_{li} + \mathcal{A}_{lj}\delta_{kj} - \mathcal{A}_{li}\delta_{ki} - \mathcal{A}_{kj}\delta_{lj}\right] \tag{2.30}$$

$\mathcal{A}_{ij}$ is the adjacency matrix of the cell array, i.e. is one only if vertex i and j are connected, and δ_{ij} is the Kronecker delta. Dynamics of small perturbations in intrinsic length is found by expanding Eq. 2.3 about the fixed point

$$\frac{d}{dt}\delta\ell_{ij} \;=\; \kappa_{ij}\left[\delta u_{ij} - \delta m_{ij}\right] \tag{2.31}$$

where

$$\kappa_{ij} \equiv \frac{\nu \ell_{ij} W'(1)}{\tau_\ell K u_{ij}} \tag{2.32}$$

Tension dynamics is easily obtained via the constitutive relation $u_{ij} = r_{ij} - \ell_{ij} = T_{ij}/K$

$$\frac{d}{dt}\delta u_{ij} = \frac{d}{dt}\delta r_{ij} - \kappa_{ij}\delta u_{ij} + \kappa_{ij}\delta m_{ij} \tag{2.33}$$

Lastly, the myosin dynamics is governed by

$$\frac{d}{dt}\delta m_{ij} = \bar{\alpha}\left(\delta u_{ij} - \delta m_{ij}\right) \tag{2.34}$$

where myosin has been rescaled to have units of interfacial deformation: $\delta m_{ij} \to aT_s K^{-1}\delta m_{ij}$ and $\bar{\alpha} \equiv \alpha\nu K^{-1}\tau_\ell^{-1}W'(1)$. Isogonal modes correspond to $\delta\theta = \delta u = 0$ which is realized by $\delta\ell_{ij} = \delta r_{ij}$, provided $\sum_{<i,j>\in\mathcal{E}_\alpha} \sigma_{ij}^{\alpha}\, \delta r_{ij}\hat{\boldsymbol{r}}_{ij} = 0$. The latter constraint is satisfied for

$$\delta\boldsymbol{r}_i = \hat{\boldsymbol{r}}_{ji}\frac{T_{ji}\Theta_\gamma}{S_i} + \hat{\boldsymbol{r}}_{ki}\frac{T_{ki}\Theta_\alpha}{S_i} + \hat{\boldsymbol{r}}_{li}\frac{T_{li}\Theta_\beta}{S_i} \tag{2.35}$$

where $\delta\boldsymbol{r}_i$ denotes displacement of vertex at which adjacent cells α, β, γ meet; $\Theta_\alpha, \Theta_\beta, \Theta_\gamma$ are independent variables associated with isogonal modes of the denoted cells and S_i denotes the area of said vertex's dual triangular plaquette. Thus, isogonal deformations have no restoring force. Eqs. 2.31 - 2.34 fully specify the closed form linearized dynamics with matrix H that can be expressed

$$S = U^{-1} H U \tag{2.36}$$

where $U \equiv \text{diag}\left[1, 1, \sqrt{u_{ij} r_{ij}}, \sqrt{\frac{\kappa_{ij}}{\bar{\alpha}}}\right]$ and

$$S \equiv \begin{pmatrix} 0 & L_{ij;kl} & -A_{ij;kl} & 0 \\ 0 & L_{ij;kl} - \kappa_{ij}\delta_{ij;kl} & -A_{ij;kl}\sqrt{\frac{u_{kl}}{r_{kl}}} & \sqrt{\bar{\alpha}\kappa_{ij}}\delta_{ij;kl} \\ 0 & \sqrt{\frac{u_{ij}}{r_{ij}}}A_{ij;kl} & \sqrt{\frac{u_{ij}}{r_{ij}}}L_{ij;kl}\sqrt{\frac{u_{kl}}{r_{kl}}} & 0 \\ 0 & \sqrt{\bar{\alpha}\kappa_{ij}}\delta_{ij;kl} & 0 & -\bar{\alpha}\delta_{ij;kl} \end{pmatrix}$$

Because the first column of the matrix is equal to zero, δr_{ij} is slaved to other components and thus the rank of H is at most $9c$ as our null space contains c isogonal modes defined above, along with the $2c$ geometric constraints (see Eq. 2.25) that are conserved by the dynamics. The left eigenvectors of isogonal modes were numerically found to be exponentially localized around the respective cell with a length scale $(\kappa + \bar{\alpha})^{-1/2}$: i.e. they are only forced with the screening length set by contractility as shown in Fig. 2.7(a). This reproduces the result found in $1D$.

The reduced matrix $\tilde{S}$ is obtained by eliminating the 1^{st} row and 1^{st} column of S. It is manifestly symmetric in our chosen basis, following immediately from the fact that $L_{ij;kl}$ and $A_{ij;kl}$ are symmetric and anti-symmetric respectively. Furthermore, it is easy to see that $L_{ij;kl}$ satisfies all properties of a normalized weighted graph Laplacian defined over edges in our triangulation and thus will be negative semi-definite, as shown in Fig. 2.5, ensuring stability of the tension-triangulation of the unperturbed ATN state. $\bar{\alpha} > 0$

introduced acoustic branches and thus phonons at long times.

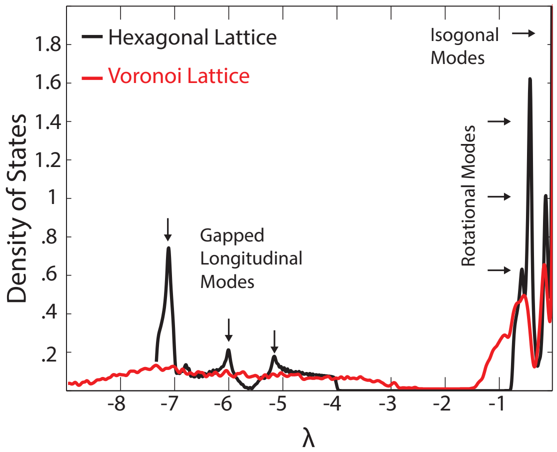

Figure 2.5: “Density of states” plot for the normal modes of H governing the dynamics of fluctuations about the ATN equilibrium corresponding to i) a hexagonal array (black line) and ii) a randomly generated Voronoi tesselation (red line). In both cases $3c$ modes lie at zero, of which c are the isogonal modes and the remaining $2c$ correspond to geometric constrains (on edge vectors). The rest of the eigenvalues are negative as required by stability. 1/3 of the modes (in the hexagonal lattice case) are separated from zero by a gap proportional to the activity parameter q.

We conclude that $2D$ modes will exhibit (albeit in a more complex form) qualitatively equivalent features as that derived for the $1D$ cable above - solid-like phonons with weak spring constants at long time and short-scale liquid like behavior dominated by isogonal deformations. This was checked by probing the linear rheology of the material as a function of the frequency ω of the perturbing boundary condition. Specifically, a square grid of $15x15$ cells was initialized with a random tension triangulation and subjected to a longitudinal force $T_B \cos(\omega t)$. The amplitude and phase of the longitudinal strain along the pulling axis was measured from the resultant simulation, Fig. 2.6 displays the result as a function of ω and position along the pulling axis boundary to boundary. The system can be seen to transition from a floppy elastic material at $\omega \sim 0$ as there is no phase difference between displacements and force. As we crossover to fluid behavior, the phase difference transitions to $\pi/2$ which is expected if the force is being balanced solely by viscocity. Higher frequency perturbations only pull on the elastic cytoskeletal network.

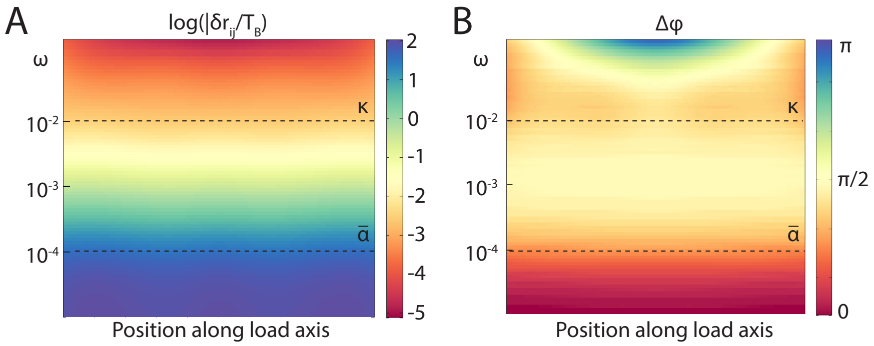

Figure 2.6: Mechanical properties of an 2D ATN. (a) Amplitude and (b) phase of the longitudinal strain (as a function of position) in response to periodic uniaxial forcing $T_B \cos \omega t$ applied at the boundaries ($\kappa = 10^{-2}$ and $\bar{\alpha} = 10^{-4}$). As the frequency ω decreases below $\bar{\alpha}$ the phase shifts from $\pi/2$ to 0 indicating crossover from viscous fluid behavior to an elastic solid. This contrasts with the conventional Maxwellian viscoelasticity crossover towards elasticity with ω *increasing* above κ .

Lastly, we ask are the measured eigenmodes localized or extended? To address this question we numerically measured the distribution of participation ratios, defined as

$$p_{n'} \equiv \sum_{n=1}^{N} |\phi_n^{n'}|^4 \tag{2.37}$$

where $\phi_n^{n'}$ represents the n^{th} component of the flattened eigenvector $\begin{pmatrix} \delta r_{ij} & \delta u_{ij} & r_{ij}\,\delta\theta_{ij} & \delta m_{ij} \end{pmatrix}^T$ and $n, n' \in [1, N]$ where N denotes the system size. If $\phi^{n'}$ is extended, then $|\phi_n^{n'}| \sim 1/\sqrt{N}$ and thus $p_{n'}$ should scale with inverse system size. Similarly, if $\phi^{n'}$ is localized, it should saturate to a finite number with increasing N. We tested the localization of our modes by tracking how the distribution of $p_{n'}$ scaled with increasing number of cells within hexagonal and randomly generated voronoi lattices. Isogonal modes were excluded from

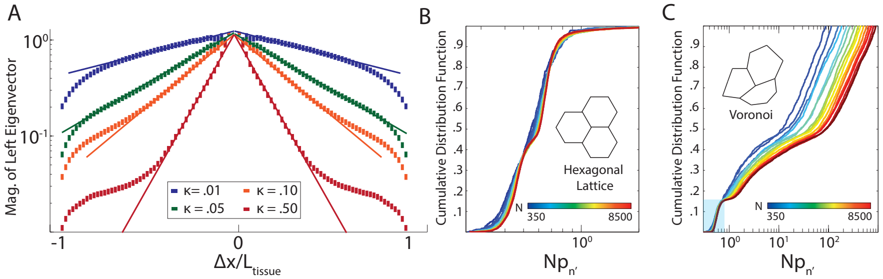

Figure 2.7: (a) Eigenvectors associated to isogonal modes fall off exponentially with the characteristic length scale of decay $\sim \kappa^{-1/2}$. Points correspond to left eigenvectors obtained by numerical diagonalization of H; solid lines are decaying exponentials with characteristic length $\kappa^{-1/2}$. (b) Eigenmode structure for regular hexagonal (b) and random Voronoi (c) lattices: fraction of eigenmodes (excluding isogonal modes) below a given participation ratio $Np_{n'}$ (defined by Eq. 2.37) scaled with the number of cells N. All modes are extended as indicated by the collapse of curves scale on top of each other.

analysis as it is known a priori that each is localized to a single cell. All non-isogonal modes are fully extended in the hexagonal case - the system is diagonalizable in a plane-wave basis - as shown numerically in Fig. 2.7b. Conversely, as shown in Fig. 2.7c, it was found that all but one band of ‘transverse’ modes localize for disordered Voronoi lattices. In other words, c modes are still fully extended on a disordered triangulation.

2.5 Empirical test of geometric compatibility in various Drosophila tissues

As discussed in Chapter 1, while it is not yet possible to measure all internal tensions in a living tissue, eqn. 2.7 provides us with a quantitative assay of the validity of the balanced tension net approximation using apical geometry alone. Exact satisfaction of the constraint $\log \chi = 0$ is not anticipated owing to the errors associated with the acquisition and analyses of imaging data, as well as due to cell array fluctuations that result in deviations from tension balance.

The appeal of the geometric compatibility constraint, defined by eqn. 2.7, is that one can directly measure it from images of an epithelial tissue and thus immediately test the validity of force balance and tension dominance assumptions. Alas, even if the assumptions were correct, one would not expect this constraint to be satisfied exactly by empirical data because of i) the measurement noise (imperfect image segmentation as well as fundamental digitization of vertex positions) and the ii) dynamical fluctuations of cells. Hence our analysis focuses on the probability density function (PDF), $P(\log \chi)$, and evaluates the tendency towards $\log \chi = 0$ (i.e. constraint satisfaction) which manifests itself as a statistically significant reduction of variance compared to a randomized "control distribution" that corresponds to mechanically unconstrained cell arrays (or convex polygonal tessellations of a plane) built from the distributions of observed angles within the real tissue. Below we discuss the exact construction of the control distribution and elucidate its discriminatory power using synthetic data. Furthermore, we expand upon potential tests one can use to analyze potential sources of the measured variation.

It is important to note that the average $\langle \log(\chi) \rangle = \frac{1}{c} \sum_{\alpha} \log(\chi_{\alpha})$ is determined entirely by χ_{α} from the cells on the *boundary* of the tissue. When computing the mean, each lattice angle in the bulk will be summed over twice with opposing signs and thus the only contribution comes from angles along the boundary. This is just a discrete manifestation of Stokes' law. Since the number of boundary cells scales as $\sqrt{c}$ for $c \gg 1$, the average goes to zero as $1/\sqrt{c}$. Hence, empirically $P(\log \chi)$ is approximately normal with zero average.

The control distribution is constructed as follows. A random cell is sampled from the segmented cell array. Each vertex of the sampled cell is *given* a random external edge using a vertex angle sampled from the empirical angle distribution. The remaining angle is simply the supplementary of the interior angle of the cell plus the randomly sampled angle. To ensure convexity, the configuration is accepted provided no angle greater than π was generated. This procedure is repeated a sufficient number of times to ensure the distribution is well sampled (set to $10x$ the number of cells in the array). Hence, the control distribution measures the 'maximum' variance possible in $\log(\chi)$ given just the set of observed lattice angles. We then compare the variances between the measured PDF and the control: $\sigma_{data}/\sigma_{null} << 1$ signifies statistically significant tendency of the observed array geometry towards small values of χ and hence approximate compatibility.

To validate the proposed statistical test, we examined synthetic data constructed by minimizing a vertex-type model energy function which allows for variation of internal pressure of cells $p_\alpha = 2\Gamma(A_\alpha - \bar{A}_\alpha)$ while making edges Hookean springs with randomized intrinsic lengths ℓ_{ij}:

$$E = \sum_{<i,j>} (r_{ij} - \ell_{ij})^2 + \Gamma \sum_{\alpha} (A_\alpha - \bar{A}_\alpha)^2 \tag{2.38}$$

Intrinsic cell area $\bar{A}_\alpha$ is to be a quenched random number sampled from a Gaussian distribution with mean $3\sqrt{3}/2$ and standard deviation σ_a. Furthermore, intrinsic edge length ℓ_{ij} is sampled from a Gaussian distribution with mean 1 and standard deviation fixed to be .2. The external space has pressure -1 to balance the internal tension of the vertex model. Cell arrays are obtained by minimization of E (approximately 300 cells were relaxed per iteration) under the prescribed boundary conditions. We then construct $P(\log \chi)$ distributions for the generated cell arrays for different values of Γ and σ_a and compare to corresponding control distributions. This allows us to estimate the ratio $\sigma_{data}/\sigma_{null}$ as a function of pressure's contribution to mechanical equilibrium.

To quantify the effect of pressure fluctuations (forced in the model by heterogeneity of $\bar{A}_\alpha$), we compute the curvature (normalized to average edge length) $R^{-1} \equiv \frac{\Delta pr}{T}$ of each edge as defined by the Young-Laplace Law, which relates the radius of curvature of the interface R^{-1} to edge tension T and the pressure difference Δp across the edge. Average curvature $\langle R^{-1} \rangle$ is a convenient measure of the extent of pressure contribution to the force balance relative to tension.

The above vertex model allowed us to quantitatively study the effect of pressure differentials, captured by $\langle R^{-1} \rangle$, and measurement error associated to the discretization of vertex positions on an image on the variance of $P(\log \chi)$. 'Pixelation' noise, denoted σ_{pix}, was introduced by scaling tissues obtained from minimization of Eq. 2.38 to match the desired edge length and then rounding vertex position to the nearest integer. Both the resultant standard deviation of the $\log(\chi)$ distribution as well as the ratio $\sigma_{data}/\sigma_{null}$ are reported in Fig. 2.8e,f. As expected, σ_χ increases as pressure differences become non-negligible ($\langle R^{-1} \rangle > .1$) and as measurement uncertainty increases. These results provide a baseline to which to compare data.

Furthermore, as cell edge curvature can be directly measured from high quality images of epithelial tissues, we can estimate both $\langle R^{-1} \rangle$ and σ_{pix} parameters corresponding to real tissues. In Fig. 2.8e,f we place on the heat maps the points corresponding to the pupal notum, ventral mesoderm, lateral ectoderm, and larval wing disc epithelia (marked respectively as the triangle, square, circle and star) for comparison with results below. Curvatures were estimated by fitting segmented edges to circles.

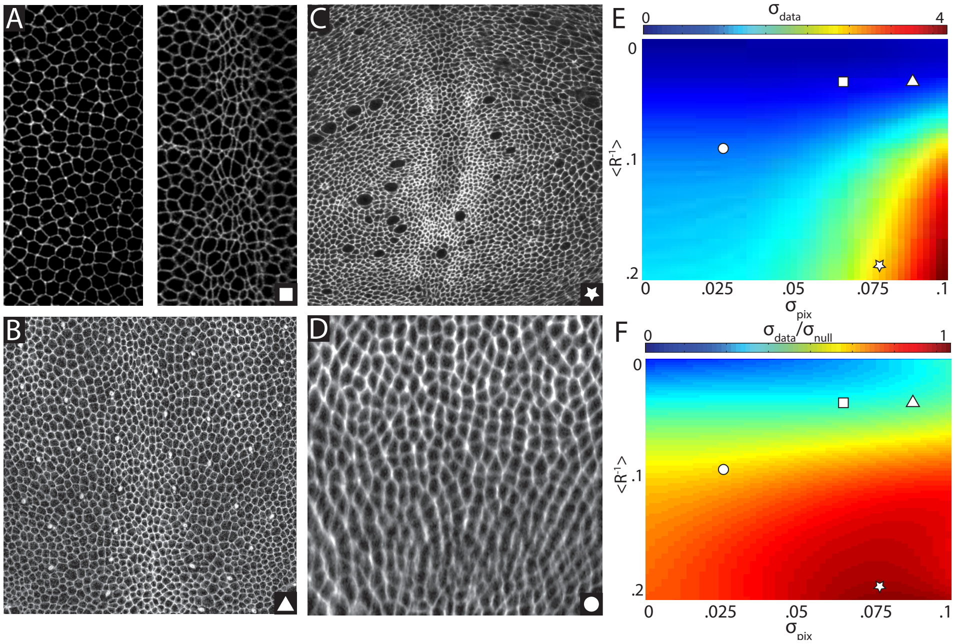

Figure 2.8: (a) An image of the ventral mesoderm (Drosophila embryo) before invagination of the ventral furrow; (b) Pupal notum epithelium; (c) Epithelium of the wing imaginal disc at the third instar larval stage; (d) Embryonic lateral ectoderm during early germ band extension; (e) A heatmap of the standard deviation of $\log(\chi)$ (obtained via synthetic data created minimizing the energy of Eq. 2.38) as a function of both average edge curvature R^{-1}, normalized to average edge length, and measurement noise σ_{pix}, simulated by introducing rounding error in vertex position. The triangle, square, circle, and star markers denote the estimated positions of the pupal notum, ventral furrow, lateral ectoderm, and wing disc epithelia respectively. (f) The analogous plot to (e) showing the ratio $\sigma_{data}/\sigma_{null}$. As curvature and measurement noise increase, the ratio tends toward 1 as expected. Again the estimated positions of each tissue is marked.

Tissue	σ_{data}	$\sigma_{data}/\sigma_{null}$	K.S. Pval
Ventral Furrow	.42	.53	6.4e-10
Pupal Notum	.51	.57	3.6e-6
Lateral Ectoderm	1.23	.72	4.6e-5
Larval Wing Disc	2.1	.98	5.7e-4

Figure 2.9: Characterization of the distribution of the compatibility measures for the four tissues.

All four analyzed tissues are shown in Fig 2.8: ventral mesoderm prior to invagination, pupal notum, lateral ectoderm during early germ band extension, and third instar larval imaginal wing disc (data kindly provided by Ken Irvine [143]). Example images of the analyzed data are shown in Fig. 2.8a-d. The measured ratios $\sigma_{data}/\sigma_{control}$ collected in Fig. 2.9, along with the Kolmogorov Smirnov p-value defined between control and empirical distributions [112], were found to be consistent with synthetic ratios of their estimated positions on Fig. 2.8f and thus we conclude both the ventral mesoderm and pupal notum are well approximated as quasistatic tissues in tension-balance.

2.6 Isogonal modes drive Drosophila ventral furrow formation

One of the striking predictions of the ATN model is the existence of the isogonal soft modes that allow easy variability of cell area. Extreme variability of apical cell area has

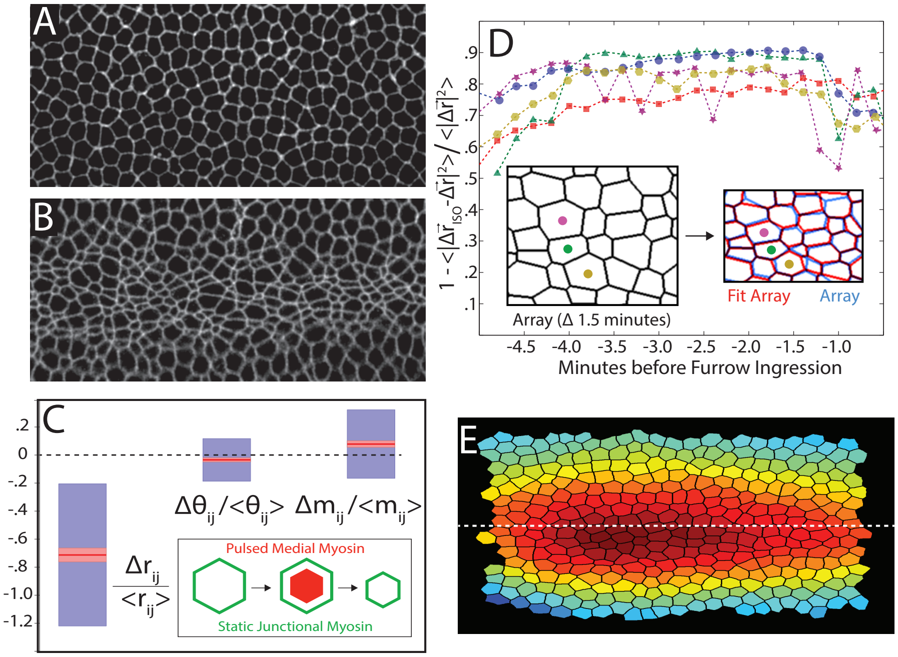

Figure 2.10: Ventral view of Drosophila embryo at the beginning of VF formation (a) and 4 minutes later (b). (c) The measured changes in edge length Δr_{ij}, edge orientation angle $\Delta\theta_{ij}$ and relative myosin level Δm_{ij} during VF formation: red lines denote the means (with 95% confidence intervals). Blue boxes denote 1σ. Edge length shrinks by $\sim 75\%$ while changes in myosin and edge orientation are considerably smaller. (d) Fraction of cell deformation ($\Delta\boldsymbol{r}$) captured by isogonality ($\Delta\boldsymbol{r}_{iso}$) obtained via least squares minimization of Eq.2.10. Each color represents an independent measurement with 200 cells. Inset: a graphical comparison for a sample fit. (e) Spatial profile of the isogonal mode amplitude, $\{\Theta_\alpha\}$ describes increasing anisotropic compression of cells towards ventral midline.

been observed at the beginning of the gastrulation process in Drosophila, when cells along the ventral midline of the embryo constrict their apical surfaces, initiating the formation of a furrow that subsequently internalizes the future mesoderm [165], as shown in Fig. 2.10ab. This apical constriction was shown to be driven by pulsed contractions of the *medial* actomyosin network (located near the apical cell surface) that pull on the *cortical* cytoskeleton. The process has been described as a “ratchet”: medial myosin pulses cause transient constrictions subsequently stabilized by the retracted cytoskeletal cortex [109].

Motivated by the agreement with the compatibility constraint found in the above section, we propose an alternative interpretation of the phenomenon in terms of the ATN model. If we assume that the *cortical* myosin concentrations are relatively static over the timescale of medial myosin pulsing, the ATN model predicts that any transient perturbation of mechanical balance due to medial myosin contractions would leave behind an isogonal deformation of the cell array, as it returns to mechanical balance dominated by cortical tensions that remain unchanged. Hence we predict that cell deformation during the early stages of ventral furrow formation should be well described by motion along an isogonal manifold.

We quantified the early VF formation process using time-lapse imaging of fluorescently-labelled myosin and cell membranes. Relative levels of cortical myosin (excluding an overall magnitude increase [109] that does not affect local tension balance) and edge orientations do not change significantly over the course of VF formation, despite large changes in edge lengths (Fig. 2.10c). This finding, together with the approximate "compatibility" of embryonic mesoderm presented in the previous section, lend strong support to the validity of the assumptions underlying the ATN model interpretation of the VF formation process in terms of isogonal deformations driven by transient medial myosin pulses.

Analyzing five movies of VF formation (as in Fig 2.10ab) we found that isogonal deformations $\Delta \boldsymbol{r}^{iso}$, found by least squares analysis of Eq. 2.10, consistently account for $\sim$85% of the measured vertex displacements, Fig. 2.10d. The spatial profile of $\{\Theta_\alpha\}$, integrated over the course of VF dynamics is approximately parabolic (see Fig. 2.10e), giving rise to isogonal, but anisotropic, constriction of cells with the long axis of cells oriented along the anterior-posterior direction [165]. Thus, the mesoderm during VF formation indeed appears to behave as a transiently perturbed ATN, flowing along the isogonal manifold comprised of the degenerate set of its (mechanical) equilibrium states (see Fig. 2.4b). The ATN model provides a reduced set of degrees of freedom that accurately describe the dynamics of VF formation.

In conclusion, we discuss the phenotypes of *twist* and *snail* mutants. *snail* embryos fail to coalesce medial myosin structures and do not initiate pulsed contraction of cells: hence *snail* embryos simply lack the transient perturbations [109] necessary to induce isogonal "flow" along the equilibrium manifold. Conversely, *twist* embryos exhibit pulsed apical contraction of cells but are unable to fully stabilize the constricted state [108]. These mutants also appear to have reduced tension in the cortical cytoskeleton and exhibit strongly curved cell-cell interfaces. The latter fact suggests relatively large differences in pressures between adjacent cells, in which case contribution of pressure to local force balance cannot be neglected. This agrees with the highly curved cell morphologies observed in *twist* RNAi mutants [109]. Pressure variation lifts the degeneracy of the ATN mechanical equilibrium manifold so that isogonal deformations experience a restoring force, thus limiting the response to transient perturbations. This intuition was checked via simulation.

Simulation of the WT phenotype was initialized to a rectangular array of hexagonal cells with unit edge length. Equations 2.2,2.3 were simulated on each edge under the assumption of a constant, uniform myosin field. Each cell's pressure was taken to be $2\Gamma\left[A_\alpha - \bar{A}_\alpha\right]$ with $\bar{A}_\alpha = 3\sqrt{3}/2$ (the area of a hexagon with a unit edge) for all cells in the mesoderm. Effects of the medial myosin pulse were simulated via a transient isotropic perturbation of tensions around cells (with amplitude comparable to the scale of cortical tension). Inter-arrival times between myosin pulses were Gaussian distributed and randomly sampled for each cell in the marked furrow (see red box in Fig. 2.11a). No pulses were simulated outside of the synthetic furrow. To represent the *twist* phenotype we carried out a similar simulation, but with the tension scale reduced by a factor of 10 so that $T \sim \Delta pr$. This moved the system out of the tension-net regime, causing the area-elasticity term to 'force' retraction of the cell after contractions caused by the myosin pulse. Randomizing $\bar{A}_\alpha$ magnified the stabilization defects - intended to simulate potential effects of the lack of a persistent medial actin network. Plots of the final lattice as well as representative time-traces from synthetic cells are shown in Fig 2.11cd.

2.7 Future tests

The ATN model presented in this chapter describes epithelial tissue dynamics in terms of three processes: i) fast relaxation towards mechanical equilibrium dominated by cortical tension, ii) myosin driven rearrangements of the cortex on an intermediate time scale, and iii) on the slowest timescale, Dynamic Recruitment (or reduction) of myosin that is driven by the internal *rate of strain* in the cortex, Eq. 2.4. The first two alone would result in a viscoelastic fluid behavior (driven by myosin generated internal forces). The unusual behavior arises from the assumed Dynamic Recruitment of myosin, which dramatically changes the asymptotic behavior so that while being able to flow at short times, ATNs, like solids, can support external stress at long times. While the presented measurements suggest the validity of tension-balance in describing the mechanical equilibrium of an epithelial tissue, new experiments will be needed to test the Dynamic Recruitment hypothesis, which was introduced to explain how myosin levels at different interfaces can be coordinated to attain tension balance across a tissue.

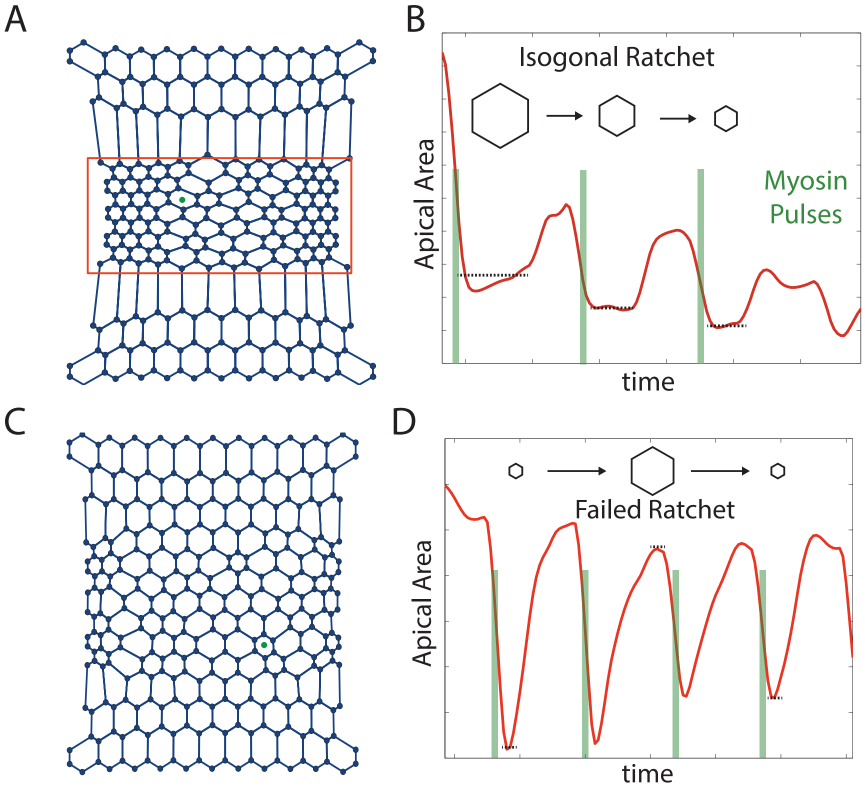

Figure 2.11: (a) Plot of the simulated active tension net with bulk medial myosin pulses within the red box. (b) A characteristic time-course of apical area of single cell during the simulation - denoted in (a) with a green dot. Cell contracts as a result of medial myosin pulses and subsequently stabilizes at a smaller area (until its neighbor is pulled). Three such pulses are shown. (c) The analogous plot to (a) but in the model with reduced tension $T \sim \Delta p r$. As pressure can no longer be neglected, cells by and large recover their apical area and do not show net constriction. (d) The time-course of apical area of cell marked with green dot in (c). The constriction fails to stabilize at a smaller area due to the influence of pressure. The result is large area fluctuations (due to small cortical tension) that do not permanently constrict.

Chapter 3

The dual formulation of epithelial mechanics

In this chapter, we pursue D'Arcy Thompson's goal of elucidating the map between biological form and the corresponding 'diagram of forces' [167] in the context of epithelial tissues. The ATN model presented in Chapter 2 explored the geometric consequences of uniform pressure across all cells within the epithelium. Static tension networks exhibit an extensive number geometric constraints, defined as the compatibility condition, which are a strict consequence of the duality of the network geometry to a tension-triangulation. Here, we relax the tension-net assumption to discover generalized variants of both the geometric compatibility condition and the 'dual' triangulation for an arbitrary cell array.

Our formalism departs from traditional vertex models [79, 80, 52]; intercellular junctions are no longer assumed to be straight polygonal edges but rather curve in accordance with the Young-Laplace law. Given that cellular pressure is isotropic and cortical tension is constant along interfaces, intercellular edges are circular arcs. As before, mechanical equilibrium of this network is achieved when tensions balance at each vertex. We show that in the context of the generalized curved network, force balance is equivalent to the geometric constraint that all centroids of the circular edges meeting at a vertex must be collinear. This is recognized as the generalization of the compatibility condition presented in Chapter 2 and is the starting point for our definition of the dual triangulation. In this way, our dual construction can be thought of as a generalization of the Cremona-Maxwell diagram to a network of circularly curved junctions. [113]

The dual triangulation encodes all information about the mechanical state of an epithelial tissue. As such, our dual triangulation provides an intuitive language to clarify the relationship between discrete cellular geometry and the 'diagram of forces' that patterns it. Remarkably, equilibrium mechanics generates geometric form analogous to the passage from a Delaunay triangulation to a Voronoi tessellation. [173, 44]

We conclude the chapter by utilizing the discovered duality as the foundation for a local 'Mechanical Inference" algorithm which greatly improves upon current image-based methods. Using synthetic data as a comparative benchmark, we show that our algorithm correctly infers mechanics under arbitrary pressure differentials and moderate measurement noise in contrast to existing methods. We show, by comparison to in-vivo data for the early stages of Drosophila gastrulation, that our "Mechanical Inference" more accurately predicts the distribution of the major molecular stress generator myosin

II. Our proposed framework defines convenient degrees of freedom in which to study the mechanics of epithelial tissues and thus we expect the formulated mechanical inverse should serve as an indispensable tool to study the laws underlying morphogenesis and the mechanics of active matter.

3.1 Equilibrium properties of an epithelial tissue with non-uniform pressure

We introduce a generalization of vertex models that parameterizes apical cell geometry by not only positions of vertices, $\boldsymbol{r}_i$, defined as the location where three or more cells meet, but we also allow for edges to be 'curved' consistent with discontinuities of stress across the cellular interface. The latter is the major departure from classical vertex models [77, 80] based upon the polygonal approximation to cellular geometry. As such, the mechanical state of the network is parameterized by an effective interfacial tension $T_{\alpha\beta}$, where α, β labels the cells partitioned by the given edge, and an effective hydrostatic pressure p_α capturing the contribution of uniaxial stress from the cell to the global mechanical balance.

Given that the cell stress is assumed isotropic, mechanical equilibrium across cell interfaces requires that edges within the cell array are circular arcs with radii $R_{\alpha\beta}$ given by the Young-Laplace Law

$$[p_\alpha - p_\beta]R_{\alpha\beta} = T_{\alpha\beta} \tag{3.1}$$

A graphical example of the resultant curved tension network is shown in Fig. 3.1a. Similarly, force balance at vertex i constrains the three tension vectors $\boldsymbol{T}_{i,\beta\alpha}$, pulling tangent to each circular arc as depicted in Fig. 3.1ab, to sum to zero

$$\frac{T_{\beta\alpha}}{R_{\beta\alpha}}[\boldsymbol{r}_i - \boldsymbol{\rho}_{\beta\alpha}]^* + \frac{T_{\alpha\gamma}}{R_{\alpha\gamma}}[\boldsymbol{r}_i - \boldsymbol{\rho}_{\alpha\gamma}]^* + \frac{T_{\gamma\beta}}{R_{\gamma\beta}}[\boldsymbol{r}_i - \boldsymbol{\rho}_{\gamma\beta}]^* = 0 \tag{3.2}$$

where $\boldsymbol{\rho}_{\beta\alpha}$ is defined as the centroid of the circular arc associated to edge α, β and $\boldsymbol{r}^* \equiv \hat{\boldsymbol{z}} \wedge \boldsymbol{r}$. Utilizing the Young-Laplace Law as defined in eq. 3.1, the force balance condition simplifies to

$$[p_\beta - p_\alpha]\,\boldsymbol{\rho}_{\beta\alpha} + [p_\alpha - p_\gamma]\,\boldsymbol{\rho}_{\alpha\gamma} + [p_\gamma - p_\beta]\,\boldsymbol{\rho}_{\gamma\beta} = 0 \tag{3.3}$$

Remarkably, at equilibrium, the centroids of all three edges meeting at a vertex are constrained to be collinear, with distance along the line controlled by relative pressure differences, depicted graphically in Fig. 3.1b. This is recognized as the generalization of the geometric compatibility condition obeyed by a static tension net of uniform pressure discussed in Chapter 2. The geometric compatibility of any cellular network with mechanical balance under arbitrary pressure differentials can be tested from an image of cell morphology alone! This is an unexpected new result.

The above geometric constraint is a corollary of the fact that there is an underlying weighted triangulation 'dual' to the equilibrium cell array, analogous to the Maxwell-Cremona diagram dual to a static network of trusses [113]. Specifically, Eq. 3.3 implies that edge centroids of a compatible network admit an irrotational decomposition

$$\boldsymbol{\rho}_{\beta\alpha} = \frac{p_\beta \boldsymbol{q}_\beta - p_\alpha \boldsymbol{q}_\alpha}{p_\beta - p_\alpha} \tag{3.4}$$

where $\boldsymbol{q}_\alpha$ is defined as the position of the vertex 'dual' to cell α. Importantly, edge

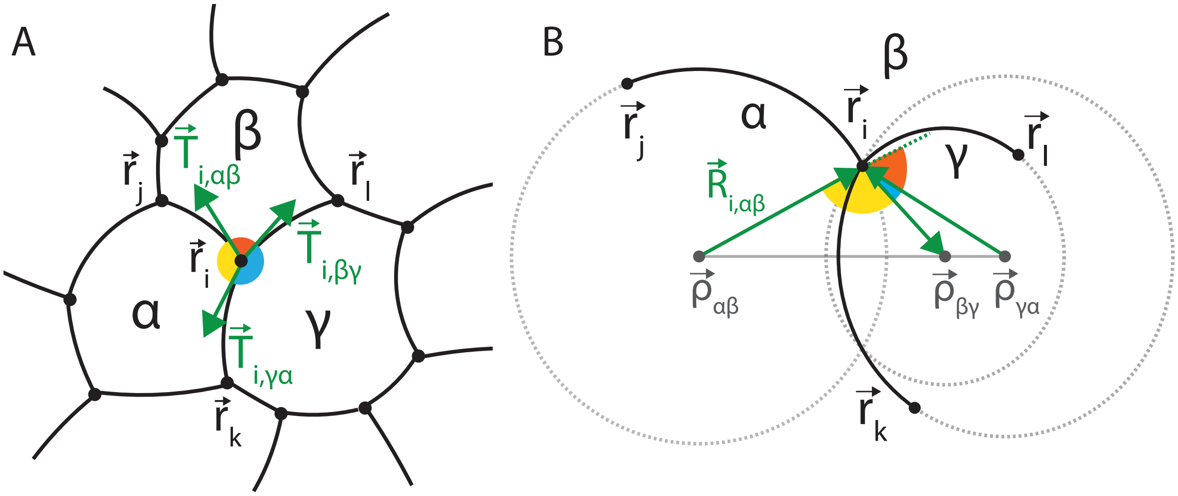

Figure 3.1: a) A depiction of a cell array with non-negligible pressure differences at equilibrium. Curvature of edges are given by the Young-Laplace law. Force balance at vertex i is imposed by summing the three tension vectors tangent to each edge. b) The equilibrium condition at a vertex in a force-balanced cell array is equivalent to the three arc centroids being collinear.

centroids $\{\boldsymbol{\rho}_{\alpha\beta}\}$ don't uniquely specify vertex positions of the network - i.e. there are many balanced cell arrays that *share the same set of edge centroids*. Specifically, in order for all three collinear edges (with centroids defined by eq. 3.4) to intersect at a well-defined vertex $\boldsymbol{r}_{\alpha\beta\gamma}$, their respective radii must obey

$$\begin{aligned}&(p_\alpha - p_\beta)\, R_{\alpha\beta}^2 + (p_\beta - p_\gamma)\, R_{\beta\gamma}^2 + (p_\gamma - p_\alpha)\, R_{\gamma\alpha}^2 = \\ &(p_\alpha - p_\beta)\, \boldsymbol{\rho}_{\alpha\beta}^2 + (p_\beta - p_\gamma)\, \boldsymbol{\rho}_{\beta\gamma}^2 + (p_\gamma - p_\alpha)\, \boldsymbol{\rho}_{\gamma\alpha}^2\end{aligned} \tag{3.5}$$

Eq. 3.5 represents v constraints on e parameters and thus, assuming vertices are three-fold, the set of solutions is expected to have a c dimensional nullspace. Given a solution, we can generate another geometrically compatible cell array by transforming $\bar{R}_{\alpha\beta}^2 =$

$R^2_{\alpha\beta} + \frac{\Theta_\alpha - \Theta_\beta}{p_\alpha - p_\beta}$, where Θ_α parameterizes the c dimensional manifold of equilibrium arrays that share the same set of edge centroids. This is recognized as the generalization of the isogonal modes previously discovered for a static tension-net in Chapter 2.

3.2 All equilibrium cellular networks are dual to a triangulation

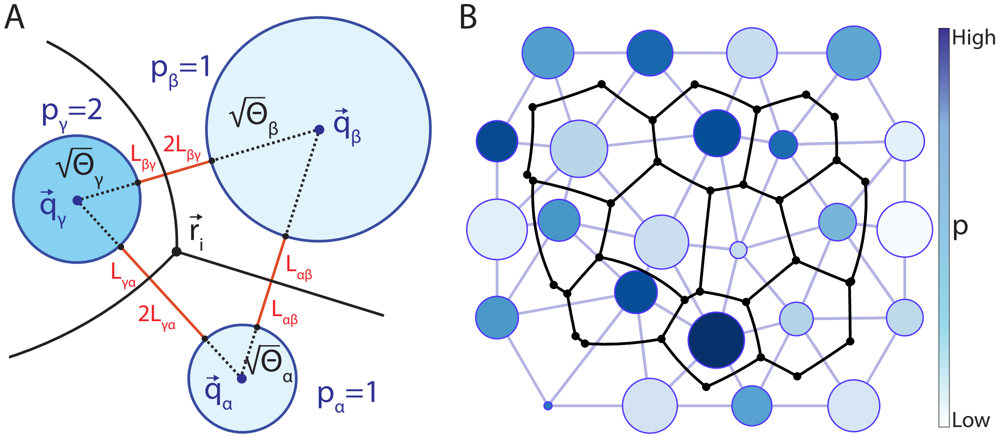

Figure 3.2: a) An example of the relationship between an equilibrium cellular network and the dual weighted triangulation. Generating points are represented by circles of radius $\sqrt{\Theta_\alpha}$ at position $\boldsymbol{q}_\alpha$ equipped with their own isotropic metric p_α. Edges are loci of points equidistant between two generating points, as shown by the red lines. b) A graphical example of the weighted dual triangulation and its corresponding equilibrium cell array.

In this section, we show that as defined in the previous section, 'dual' vertices $\{\boldsymbol{q}_\alpha\}$, along with the introduced weights $\{\Theta_\alpha, p_\alpha\}$ generalize the passage between Voronoi tessellations and Delaunay triangulations. Specifically, we take the distance d_α from point

$\boldsymbol{q}_\alpha$ to position $\boldsymbol{r}$ to be

$$d_\alpha^2(\boldsymbol{r}) = p_\alpha |\boldsymbol{r} - \boldsymbol{q}_\alpha|^2 - \Theta_\alpha \tag{3.6}$$

As depicted in Fig. 3.2a, each generating point $\boldsymbol{q}_\alpha$ is now represented by a circle of finite radius $\sqrt{\Theta_\alpha}$. Distance from this point is measured from the circumference of the circle. Similarly, each generating point measures distance proportional to $\sqrt{p_\alpha}$, depicted by the hue of each circle in Fig. 3.2a. Hence, the squared distance from point $\boldsymbol{q}_\alpha$ is given by the expression

Analagous to the voronoi-delaunay construction, edge α, β within the corresponding cell array is the locus of points equidistant from the generators at $\boldsymbol{q}_\alpha$ and $\boldsymbol{q}_\beta$ and thus must satisfy the equation

$$p_\alpha \left|\boldsymbol{r}_{\alpha\beta} - \boldsymbol{q}_\alpha\right|^2 - \Theta_\alpha = p_\beta \left|\boldsymbol{r}_{\alpha\beta} - \boldsymbol{q}_\beta\right| - \Theta_\beta \tag{3.7}$$

Squaring this out and expanding

$$\boldsymbol{r}_{\alpha\beta}^2 \left[p_\alpha - p_\beta\right] - 2\, \boldsymbol{r}_{\alpha\beta} \cdot \left[p_\alpha \boldsymbol{q}_\alpha - p_\beta \boldsymbol{q}_\beta\right] + \left[p_\alpha \boldsymbol{q}_\alpha^2 - p_\beta \boldsymbol{q}_\beta^2 - \Theta_\alpha + \Theta_\beta\right] = 0 \tag{3.8}$$

We define $\boldsymbol{\rho}_{\alpha\beta} \equiv \frac{p_\alpha \boldsymbol{q}_\alpha - p_\beta \boldsymbol{q}_\beta}{p_\alpha - p_\beta}$ (note it matches with Eq. 3.4) and complete the square to obtain

$$\left[\boldsymbol{r}_{\alpha\beta} - \boldsymbol{\rho}_{\alpha\beta}\right]^2 = \frac{p_\alpha p_\beta |\boldsymbol{q}_\alpha - \boldsymbol{q}_\beta|^2 + (p_\alpha - p_\beta)\left[\Theta_\alpha - \Theta_\beta\right]}{\left[p_\alpha - p_\beta\right]^2} = R_{\alpha\beta}^2 \tag{3.9}$$

This is the equation for a circle of radius $R_{\alpha\beta}$ centered at position $\boldsymbol{\rho}_{\alpha\beta}$. Importantly, we immediately see that the center and radius of the circle obey Laplace's Law and force balance, Eq. 3.3! In short, every cell tessellation has a dual description as a weighted triangulation. Interpreting p_α as the 'apical' 2D pressure immediately implies that the tension of this edge is

$$T_{\alpha\beta} = \sqrt{p_\alpha p_\beta |\boldsymbol{q}_\alpha - \boldsymbol{q}_\beta|^2 + (p_\alpha - p_\beta)\left[\Theta_\alpha - \Theta_\beta\right]} \tag{3.10}$$

Note that the generalized isogonal modes Θ no longer leave tensions invariant. Each vertex $\boldsymbol{r}_{\alpha\beta\gamma}$ position of the curved cell array occurs at the intersection of three edges (circles) and thus must simultaneously satisfy the following three equations

$$|\boldsymbol{r}_{\alpha\beta\gamma} - \boldsymbol{\rho}_{\beta\alpha}|^2 = R^2_{\beta\alpha} \qquad |\boldsymbol{r}_{\alpha\beta\gamma} - \boldsymbol{\rho}_{\alpha\gamma}|^2 = R^2_{\alpha\gamma} \qquad |\boldsymbol{r}_{\alpha\beta\gamma} - \boldsymbol{\rho}_{\gamma\beta}|^2 = R^2_{\gamma\beta} \tag{3.11}$$

We subtract the second equation from the first and expand out to obtain

$$2\,\boldsymbol{r}_{\alpha\beta\gamma} \cdot \left[\boldsymbol{\rho}_{\alpha\gamma} - \boldsymbol{\rho}_{\beta\alpha}\right] = \left[R^2_{\beta\alpha} - \rho^2_{\beta\alpha}\right] - \left[R^2_{\alpha\gamma} - \rho^2_{\alpha\gamma}\right] \tag{3.12}$$

Substitute in each definition from above and define $\boldsymbol{\eta}_{\alpha\beta\gamma} \equiv p_\alpha \boldsymbol{t}_{\gamma\beta} + p_\beta \boldsymbol{t}_{\alpha\gamma} + p_\gamma \boldsymbol{t}_{\beta\alpha}$ where $\boldsymbol{t}_{\beta\alpha} \equiv p_\beta \boldsymbol{q}_\beta - p_\alpha \boldsymbol{q}_\alpha$

$$\begin{aligned}&\frac{2\,\boldsymbol{r}_{\alpha\beta\gamma} \cdot \boldsymbol{\eta}_{\alpha\beta\gamma}}{\left[p_\beta - p_\alpha\right]\left[p_\alpha - p_\gamma\right]} = \\ &\frac{(p_\gamma - p_\beta)\left[p_\alpha \boldsymbol{q}^2_\alpha - \Theta_\alpha\right] + (p_\alpha - p_\gamma)\left[p_\beta \boldsymbol{q}^2_\beta - \Theta_\beta\right] + (p_\beta - p_\alpha)\left[p_\gamma \boldsymbol{q}^2_\gamma - \Theta_\gamma\right]}{\left[p_\beta - p_\alpha\right]\left[p_\alpha - p_\gamma\right]}\end{aligned} \tag{3.13}$$

This equation is solved by

$$\begin{aligned}\boldsymbol{r}_{\alpha\beta\gamma} &= \frac{1}{4S_{\alpha\beta\gamma}}\left[\left[p_\alpha \boldsymbol{q}^2_\alpha - \Theta_\alpha\right]\boldsymbol{t}^*_{\gamma\beta} + \left[p_\beta \boldsymbol{q}^2_\beta - \Theta_\beta\right]\boldsymbol{t}^*_{\alpha\gamma} + \left[p_\gamma \boldsymbol{q}^2_\gamma - \Theta_\gamma\right]\boldsymbol{t}^*_{\beta\alpha}\right] + \Gamma_{\alpha\beta\gamma}\boldsymbol{\eta}^*_{\alpha\beta\gamma} \\ &= \boldsymbol{r}^0_{\alpha\beta\gamma} + \Gamma_{\alpha\beta\gamma}\boldsymbol{\eta}^*_{\alpha\beta\gamma}\end{aligned} \tag{3.14}$$

where we've defined $\boldsymbol{t}^*_{\beta\alpha} \equiv \hat{\boldsymbol{z}} \wedge \boldsymbol{t}_{\beta\alpha}$. The value of $\Gamma_{\alpha\beta\gamma}$ is obtained by intersecting the line with the original circles. Thus, plug this expression back into our first equation for a circle

$$\Gamma^2_{\alpha\beta\gamma}\,\eta^2_{\alpha\beta\gamma} + 2\,\Gamma_{\alpha\beta\gamma}\left[\boldsymbol{r}^0_{\alpha\beta\gamma} - \boldsymbol{\rho}_{\beta\alpha}\right]\cdot\boldsymbol{\eta}^*_{\alpha\beta\gamma} + (r^0_{\alpha\beta\gamma})^2 - 2\,\boldsymbol{r}^0_{\alpha\beta\gamma}\cdot\boldsymbol{\rho}_{\beta\alpha} + \rho^2_{\beta\alpha} - R^2_{\beta\alpha} = 0 \quad (3.15)$$

After some arithmetic hoops, the solution to this equation is found to be

$$\Gamma^{\pm}_{\alpha\beta\gamma} = \frac{1}{\left[\frac{\eta^2_{\alpha\beta\gamma}}{2S_{\alpha\beta\gamma}}\right]}\left[1 - \frac{\boldsymbol{r}^0_{\alpha\beta\gamma}\cdot\boldsymbol{\eta}^*_{\alpha\beta\gamma}}{2S_{\alpha\beta\gamma}} \pm \sqrt{\left[1 - \frac{\boldsymbol{r}^0_{\alpha\beta\gamma}\cdot\boldsymbol{\eta}^*_{\alpha\beta\gamma}}{2S_{\alpha\beta\gamma}}\right]^2 - \left[\frac{\eta^2_{\alpha\beta\gamma}}{2S_{\alpha\beta\gamma}}\right]\left[\frac{(r^0_{\alpha\beta\gamma})^2}{2S_{\alpha\beta\gamma}}\right]}\right] \quad (3.16)$$

Therefore, *every* equilibrium cellular network is dual to a weighted triangulation. An example of a cell array and its conjugate triangulation is shown in Fig. 3.2b. Crucially, the geometry of the dual weighted triangulation *directly* encodes all mechanical parameters of the conjugate force-balanced cell array. In the limit that pressure $p_\alpha = p_0$ is set to a uniform constant, we recover the properties of the ATN model presented in Chapter 2 where again Θ_α plays the role of the zero, isogonal mode. Additionally, setting all $\Theta_\alpha = \Theta_0$ we recover the Delaunay to Voronoi duality as we note that Eq. 3.14 reduces to the circumcenter of its respective triangle.

Provided there is time-scale separation between cellular rearrangements and mechanical equilibration, it is common to approximate morphogenesis as the adiabatic evolution of cellular geometry constrained to instantaneously obey mechanical equilibrium. The above dual weighted triangulation provides us with a simple set of degrees of freedom to describe such adiabatic cellular flows generically. In fact, any vertex model, independent of the assumed form of the mechanical energy and proposed feedback mechanisms, will reduce to our dual geometric description. Choice of mechanical feedback and cytoskeletal regulation is tantamount to an assumption for the forward equation of motion for $\{\boldsymbol{q}, p, \Theta\}$. Thus, we will find it useful to measure the dual triangulation directly from the data.

3.3 Formulation of local Mechanical Inverse using dual triangulation

The above section formulated the forward problem: given a weighted triangulation, $\{\boldsymbol{q}_\alpha, \Theta_\alpha, p_\alpha\}$, eqns. 3.10, 3.14 fully specify the geometry of the conjugate equilibrium cell array. Ultimately we wish to solve the *inverse* problem. Given a cell array, we seek to infer an approximate dual weighted triangulation that accurately reproduces the observed cellular morphology and thus ultimately measures the underlying compatible mechanical state. This is achieved by minimizing the least-squares difference between the observed cell geometry and the estimated geometry from the dual triangulation.

Specifically, the dual weighted triangulation is fit by minimizing the energy

$$E = \frac{1}{n_e} \sum_{<\alpha,\beta>} \frac{1}{2N_{\alpha\beta}} \sum_{n}^{N_{\alpha\beta}} \left[|\boldsymbol{r}_{\alpha\beta|n} - \boldsymbol{\rho}_{\alpha\beta}| - R_{\alpha\beta} \right]^2 \tag{3.17}$$

$\boldsymbol{r}_{\alpha\beta|n}$ denotes the n^{th} estimated position of edge α, β obtained directly from the segmentation. $\boldsymbol{\rho}_{\alpha,\beta}$ and $R_{\alpha\beta}$ are given by eqns. 3.4 and 3.10 (in conjunction with Laplace's Law) respectively. Eq. 3.17 has a simple geometric interpretation - it measures the distance between the estimated and measured circular arc for each edge in degrees of freedom that natively enforce geometric compatibility with force balance as per eq. 3.3. To obtain an initial guess for minimization of Eq. 3.17, we leverage the fact that $\{\boldsymbol{\rho}_{\alpha\beta}\}$ is independent of $\{\Theta_\alpha\}$ to obtain initial estimates for $\{\boldsymbol{q}_\alpha\}$ and $\{p_\alpha\}$. As depicted in Fig. 3.1, the vector pointing from each arc's centroid to either of the attached vertices, $\boldsymbol{r}_i - \boldsymbol{\rho}_{\alpha\beta}$, is orthogonal to the associated tension vector $\boldsymbol{T}_{i,\beta\alpha}$ as they lay along the radial and tangential directions of edge $\alpha\beta$ respectively. In conjunction with Eq. 3.4, this implies that $[(p_\alpha - p_\beta)\,\boldsymbol{r}_i - (p_\alpha \boldsymbol{q}_\alpha - p_\beta \boldsymbol{q}_\beta)] \cdot \hat{\boldsymbol{T}}_{i,\beta\alpha} = 0$ which can immediately be leveraged to fit $\{\boldsymbol{q}_\alpha, p_\alpha\}$ to the cell array. Specifically, we minimize the energy functional

$$E_1\left[\boldsymbol{q}_\alpha, p_\alpha\right] = \frac{1}{n_e} \sum_{<\alpha,\beta>} \left[\hat{\boldsymbol{\tau}}_{i,\beta\alpha} \cdot \hat{\boldsymbol{T}}^{obs}_{i,\beta\alpha}\right]^2 + \left[\hat{\boldsymbol{\tau}}_{j,\beta\alpha} \cdot \hat{\boldsymbol{T}}^{obs}_{j,\beta\alpha}\right]^2 + \Lambda\Big[|\boldsymbol{q}_{\beta\alpha}| - n_e\Big]$$

where $\boldsymbol{\tau}_{i,\beta\alpha} \equiv (p_\alpha - p_\beta)\,\boldsymbol{r}^{obs}_i - (p_\alpha \boldsymbol{q}_\alpha - p_\beta \boldsymbol{q}_\beta)$ has been defined for notational convenience. $\boldsymbol{r}^{obs}_i$ is the vertex position measured from the segmentation and $\hat{\boldsymbol{T}}^{obs}_{i,\beta\alpha}$ is obtained by fitting each edge to a circular arc, described in detail below. Λ is a Lagrange multiplier that fixes the scale in the q-plane and thus ensures we don't infer the trivial solution with uniform $\boldsymbol{q}$ and p. Given $\boldsymbol{q}^0_\alpha$ and p^0_α, we obtain Θ^0_α by linear regression of

$$\frac{p^0_\alpha p^0_\beta |\boldsymbol{q}^0_\alpha - \boldsymbol{q}^0_\beta|^2 - R^2_{\alpha\beta}}{p^0_\alpha - p^0_\beta} = \Theta_\alpha - \Theta_\beta \tag{3.18}$$

subject to the constraint that $\sum_\alpha \Theta_\alpha = 0$.

Importantly, our inverse is over-constrained in contrast to previously proposed methods [29, 83]. Assuming all vertices are three-fold, the number of geometric degrees of freedom of a curved cell array, $2n_v + n_e = 7c$, is greater than $4c$ parameters allowed to vary in the minimization of Eq. 3.17. This allows us to 'measure' boundary stresses using just information of bulk cellular morphology! As such, our method is local and thus immediately applicable to inference of inter-tissue forces.

3.4 Validation of local Mechanical Inverse using synthetic data

In order to verify the validity of our algorithm to infer a possible dual weighted triangulation that corresponds to the observed cell geometry, we checked its ability to invert known values and compare our algorithm against other state-of-the-art mechanical inversion techniques. For this, we need a reliable way to generate arbitrary equilibrium networks. Values for $\{\boldsymbol{q}_\alpha\}$, $\{p_\alpha\}$, and $\{\Theta_\alpha\}$ can be chosen arbitrarily. The only complicated step is to compute the resultant graph topology, i.e. which three cells meet at each vertex. This is computed using MATLAB's native bwdist and watershed functionality. Specifically, distance away from each generating point $\boldsymbol{q}_\alpha$ is calculated using bwdist and

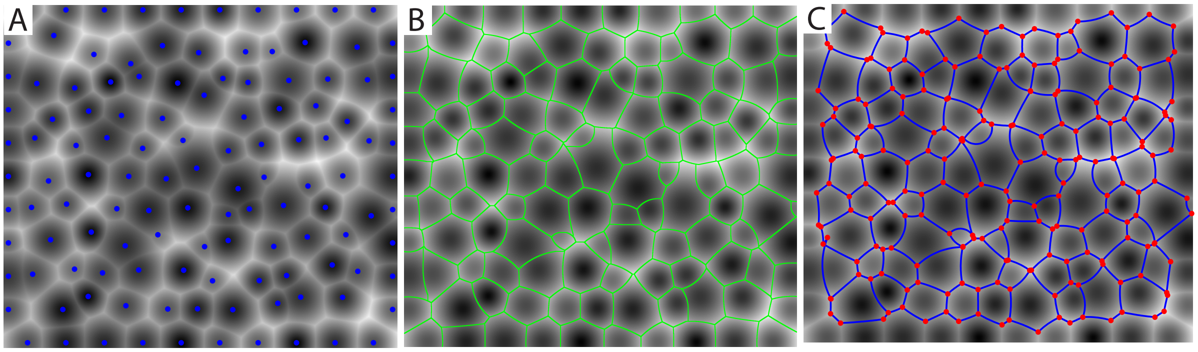

Figure 3.3: a) An example plot of the image of closest weighted distance from all generating points (shown as blue dots). b) An output of edges, defined as the locus of points equidistant between neighboring generating points, overlayed in green over the original distance function. c) The segmentation output from the watershed algorithm is used to infer the triangulation topology. The resultant triangulation using the known values for the generating points and the measured triangulation topology, is overlayed in blue.

then multiplicatively/additively weighted by p_α/Θ_α to obtain $d_\alpha^2(\boldsymbol{r}) = p_\alpha|\boldsymbol{r}-\boldsymbol{q}_\alpha|^2-\Theta_\alpha$ estimated over the image. This procedure is repeated for each generator and the minimum across all points is taken - the net result is then a scalar field that measures the minimum weighted distance away from any triangulation vertex, $d(\boldsymbol{r})^2 = \min_\alpha d_\alpha^2(\boldsymbol{r})$. An example is given in Fig. 3.3a. Recall that edges of the corresponding cell geometry are defined as the locus of points equidistant away from each generator and thus will be 'ridges' of local maxima within the image $d^2(\boldsymbol{r})$ that are found easily using the watershed algorithm, see Fig. 3.3b for an example. Vertices of this segmentation are defined as branch points of the resultant skeletonization and are used to define the generated triangulation topology. The resultant equilibrium network can then be immediately calculated from the original parameters for $\{\boldsymbol{q}_\alpha\}$, $\{p_\alpha\}$, and $\{\Theta_\alpha\}$. An example is plotted over the distance map in Fig. 3.3c.

The synthetic data utilized to test our inverse algorithm was generated by initializing a triangular lattice of ~ 120 generating points $\boldsymbol{q}_\alpha$ within a rectangle of size $[1, \sqrt{3}/2]$. Gaussian noise of tunable strength σ_q was added to each generator position. Pressures p_α were pulled from a uniform distribution of tunable width σ_p to generate lattices of varying curvature used in the correlation plots presented below. Values for $\{\Theta_\alpha\}$ were pulled from a Gaussian with standard deviation .2. Once exact values were fixed, exact cell geometry was calculated utilizing the fitting algorithm described above - i.e. minimization of Eq. 3.17. Random white noise, modeling measurement noise, was added to both vertex position $\boldsymbol{r}_i$ as well as position of edge centroids $\boldsymbol{\rho}_{\alpha\beta}$ to test sensitivity of the algorithm.

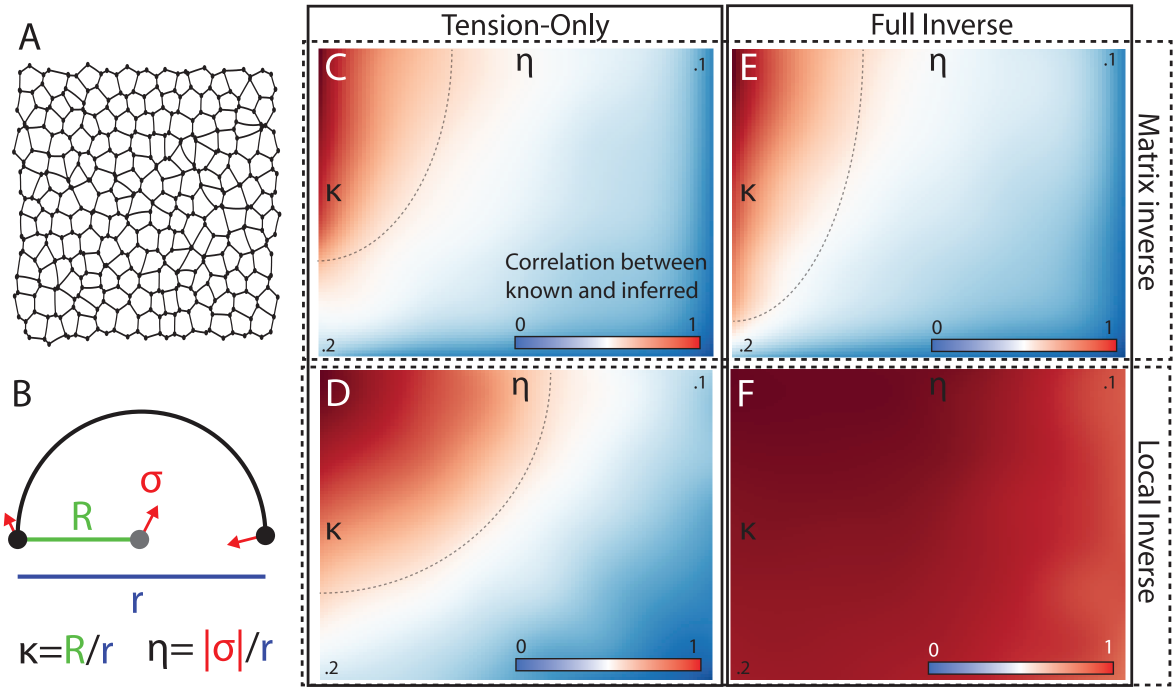

Figure 3.4: (a) An example of the synthetic cell array used to benchmark the proposed inference algorithm. (b) Graphical depiction of the two parameters, measurement noise η and normalized bond curvature κ, defined to test inverse procedures. σ denotes the average strength of simulated measurement noise, R is the radius of curvature, and r is the distance between vertices. Remaining four plots represent heatmaps of correlation between inferred tensions and pressures as a function of average κ and η for (c) tension matrix inverse (d) tension dual inverse (all $p_\alpha = 1$) (e) pressure matrix inverse (f) weighted triangulation inverse. Regions of correlation higher than .8 are delineated by the gray dashed line. Note dramatic improvement of (f) compared to (e), or (d) compared to (c).

A graphical example can be seen in Fig. 3.4a.

We benchmarked four mechanical inverse algorithms as a function of measurement noise, η, as described above, and the contribution of pressure to the mechanical balance, κ, both are graphically defined in Fig. 3.4b. Specifically, we investigated the relative efficacies of the following inference schemes: (i) the matrix inverse with all pressures rigidly constrained to 1, (ii) the dual inverse with all pressures rigidly constrained to 1, (iii) the full matrix inverse augmented with measured curvatures and (iv) the full weighted dual inference. The resultant correlation between inferred and the known generated tensions and pressures are shown in Fig. 3.4(c-f). As is clear, both the constant pressure (ii) and fully generalized dual inverses (iv) are significantly less sensitive to measurement noise than their matrix inverse counterparts (algorithms (i) and (iii) respectively). Furthermore, we see algorithm (iii) fails for $\kappa \sim .2$ due to the assumptions of small pressure differentials used to linearize the underlying force-balance equations. Inference of the weighted-dual triangulation is robust to both, showing high correlation in the entire tested parameter regime.

3.5 In-vivo correlates of local mechanical inference in Drosophila

As will be discussed in detail in Chapter 4, immediately succeeding the formation of the ventral furrow (VF), Drosophila embryos undergo germ-band extension (GBE), a major morphogenetic movement resulting in the convergent extension of the lateral ectoderm, a tissue which approximately doubles its length along the embryo's antero-posterior (AP) axis through coordinated cell intercalation events [81]. Cell neighbor exchanges are thought to be oriented by myosin anisotropy within the tissue, which distributes into supracellular cables that run along the dorso-ventral (DV) axis of the embryo that, in turn, orient the direction of intercalations via the active contraction of cytoskeletal actin

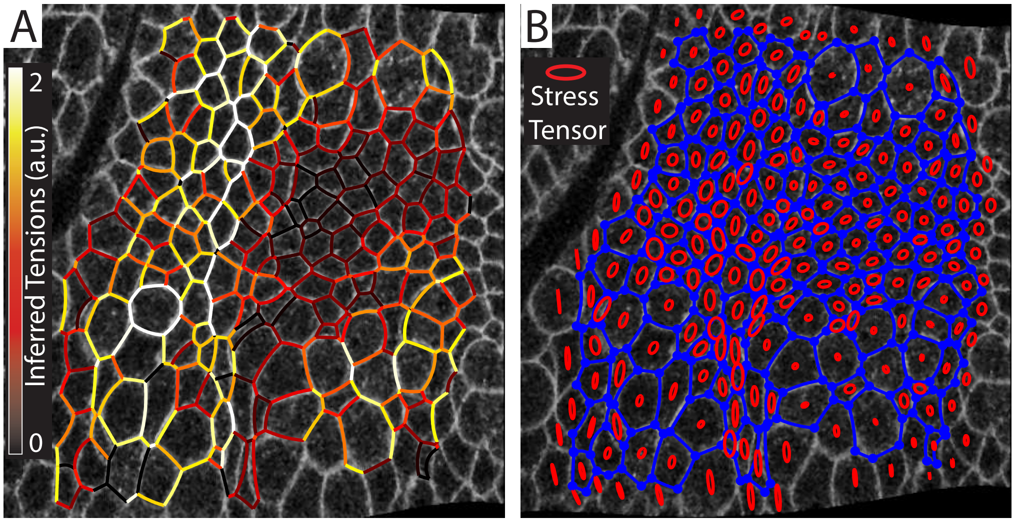

Figure 3.5: (a) An overlay of inferred tensions on the curved cellular array produced from the estimated dual weighted triangulation during germ band extension (GBE) of the lateral ectoderm during early Drosophila embryogenesis. (b) The analogous plot as in (a) but overlayed with the average stress tensor for each cell plotted as an ellipse. The major/minor axis of the ellipse corresponds to the principal/minor axis of stress.

bundles [36]. This has been supported by ablation assays that have determined the supracellular myosin cables exhibit significantly higher cortical tension than AP oriented cell junctions [145]

As evinced by Fig. 3.5a, the proposed stress-inference can immediately test this picture by 'direct', non-destructive, measurement of tensions shown overlayed over the fluorescent-marked membrane. Strikingly, we find the observed cell geometry to be well-fit by an equilibrium cell network over the first 90 minutes of convergent extension, exhibiting an average residual of eq. 3.17 of approximately 1 throughout convergent extension. As shown in Fig. 3.6a, we find a good correlation $\rho \sim .4$ between measured myosin line density and inferred cortical tension during the fast phase of GBE (first 40 minutes), strongly supporting the proposition that myosin is the molecular generator of active stress driving cell intercalation. Furthermore, our algorithm greatly outperforms those based upon simple matrix inferences given fixed geometry.

Another ubiquitous morphogenetic motif found in elongating tissues is the coordinated axis of division of mitotic cells. While intercalations account for the majority of the observed shape change during GBE, it has been shown that cells within the posterior region of the lateral ectoderm systematically orient their division axes to the AP axis, contributing to the global elongation [39]. The upstream signal that instructs the orientation of divisions is largely unknown, although the division axis of such cells is randomized in embryos lacking AP patterning. Strong evidence has emerged that the cell's mechanical environment plays a large role in spindle alignment [102, 123]. Our stress inference supports this hypothesis.

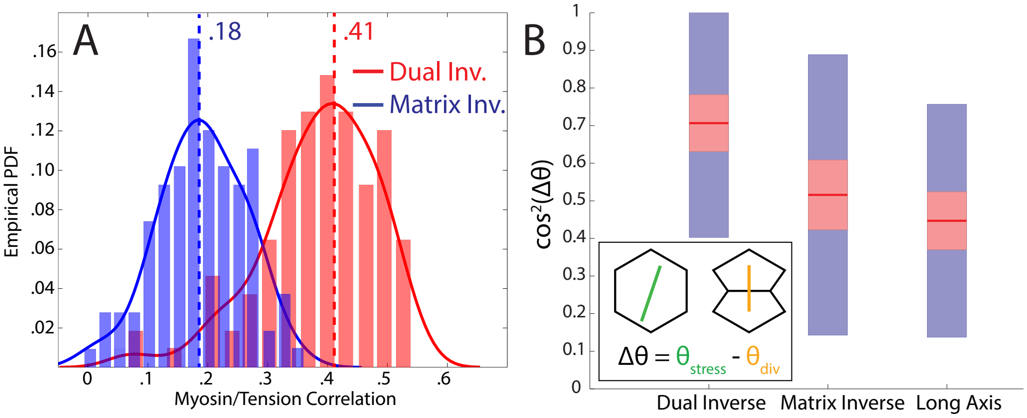

Figure 3.6: (a) Comparison of the correlation between myosin and inferred tensions between the matrix inverse and our proposed dual inference algorithms during the first 40 minutes of GBE. (b) Comparison of the division axis of oriented cell divisions during GBE and the predicted axis of division using the computed average stress per cell (computed using the new and old inverses) and the long axis. Stress and long axis were computed for mitotic cells 2 minutes before the registered time of division.

The average stress tensor for each cell, plotted in Fig. 3.5b as an ellipse, is given by

$$\bar{\sigma}_{\alpha}^{ab} = \frac{1}{A_{\alpha}} \int_{A_{\alpha}} d^2\boldsymbol{r}\, \sigma^{ab}(\boldsymbol{r}) = p_{\alpha}\delta^{ab} + \sum_{\{\beta\}_{\alpha}} \frac{T_{\alpha\beta}}{2A_{\alpha}} \int_{\boldsymbol{r}_{\alpha\beta}} dr\, \hat{\tau}_{\alpha\beta}^{a} \hat{\tau}_{\alpha\beta}^{b} \tag{3.19}$$

where $\{\beta\}_{\alpha}$ denotes all cells connected to cell α. The second term denotes the line integral over each edge belonging to cell α. $\hat{\boldsymbol{\tau}}_{\alpha\beta}$ is taken to be the tangent normal to the circular arc of edge α, β. This result is derived explictly in the appendix. As shown in Fig. 3.6b, we find the principal stress axis, computed for 70 tracked divisions over roughly 90 minutes of convergent extension, to be a stronger predictor of spindle orientation at the time of division, misplacing the predicted spindle axis on average by $\sim 25^0$, as opposed to long axis, a common predictor of future division orientation. Furthermore, the proposed inverse produced a stronger prediction (based upon 95% confidence intervals using t-test) than currently available image-based methods and the commonly used geometric long axis. The improved precision is resultant from our model's ability to capture large pressure differentials, in direct contrast to inference methods based on classical vertex models.

3.6 Mechanical inference reveals patterns of stress

To demonstrate the ubiquitous utility of the local Mechanical Inverse, we ran the proposed algorithm on various supplementary epithelial cell arrays. Specifically, the algorithm was utilized to infer stress of the developing chick basilar papilla [62], mouse cochlea [163], larval Drosophila eye [105], and the pupal Drosophila notum [10]. All fits were found to have residual energy $E \sim 1$ (defined in eq. 3.17) implying excellent compatibility with a cell array at force balance. The resultant interfacial tensions are plotted as a heatmap in Fig. 3.7.

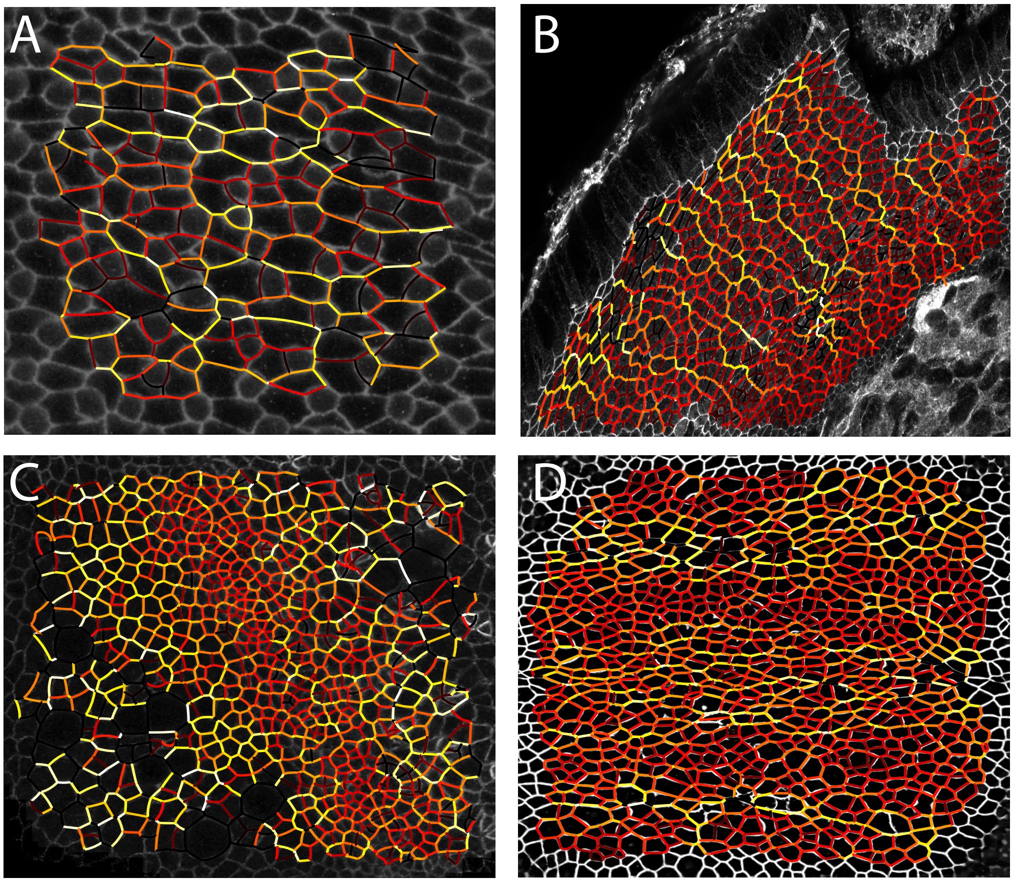

Figure 3.7: Representative images of cellular morphology from the developing (a) chick basillar papilla at embryonic day 6 (b) mammalian cochlea (c) Drosophila larval compound eye , and (d) Drosophila pupal notum. Color code represents the inferred cortical tension - the hotter the color implies higher tension. All fits were excellent with $E \sim 1$ implying we were on average 1 pixel off the segmented position of edges.

The mechanical "inference" algorithm gives us a quantitative window into the patterns of stress within developing tissues. We highlight two examples from the above data set. We first focus on the developing Drosophila compound eye, shown in Fig. 3.7c.

During the larval stage, the eye undergoes a dynamic transition from an unordered epithelium into a highly regular hexagonal pattern of ommatidial cells destined to become the adult composite retina cells [26]. The ordering transition is driven by a morphogenetic furrow that propagates through the tissue. Cells arrest their proliferation as they enter the furrow and leave fully differentiated and geometrically patterned [26]. The inferred pressure field, shown in Fig. 3.8 displays the morphogenetic furrow has a factor of 2 higher pressure than the surrounding tissue. Thus the furrow is a traveling pressure wave! Furthermore, we see that ommatidia cells retain their high pressure state as the furrow passes.

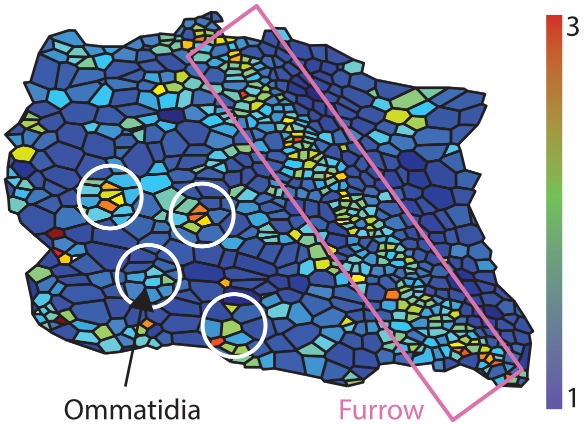

Figure 3.8: Heatmap of pressures measured within the Drosophila compound eye [105]. The furrow is marked by the pink box while a subset of ommatidia are circled in white. The furrow is progressing to the right of the image. We see high pressure both throughout the furrow and within the ommatidial cells.

We next examine the Drosophila pupal notum, shown in Fig. 3.7d. The mechanical 'inference' algorithm shows three macrosopic stress cables running along the horizontal axis of the tissue. This is confirmed by coarse-graining the microscopic stress tensor (full details on the coarse-graining procedure can be found in the appendix) and examining the three resultant components. As shown in Fig.3.9, the largest stress is concentrated at the center of the tissue, with symmetric stress cables flanking the midline.

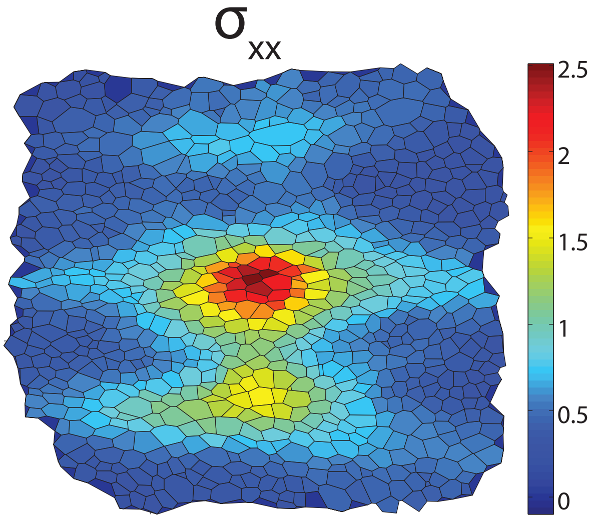

Figure 3.9: Heatmap of the *xx* component of the coarse-grained stress tensor of the Drosophila pupal notum [105]. The other components showed no pattern at the mesoscopic scale.

Chapter 4

Active cell mechanics of coordinated cellular rearrangements

Convergent extension is a highly conserved developmental process by which tissues extend along one axis concomitant with contraction along the orthogonal direction [176]. Mechanistically, the shape transformation of the overall tissue emerges from the hyperbolic flow of its constituent cells. At the cellular level, the hyperbolic flow must be generated by coordinated cellular rearrangements, also known as T1 processes [174, 81]. A graphical representation of both scales can be found in Fig. 4.1. Zooming in even further, patterned T1 processes within an epithelium place a unique demand on adherens junctions: the tissue must remain a confluent layer while simultaneously remodeling cellular interfaces [36].

In the context of the *Drosophila melanogaster* embryo, convergent extension of the

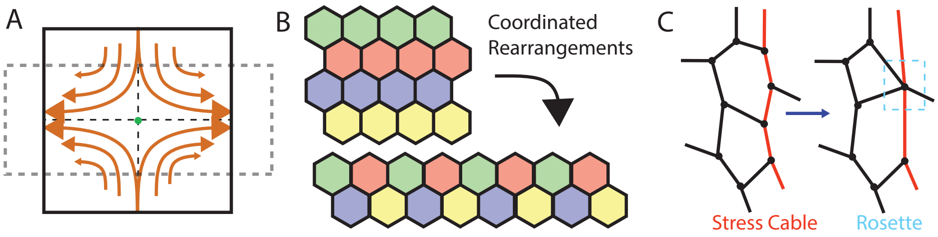

Figure 4.1: (a) The developmental movement convergent extension results in the elongation of one tissue axis at the expense of length in the other as the result of a hyperbolic cellular flow, shown graphically as orange arrows. The final tissue shape is shown as the gray dashed line. (b) The hyperbolic cell flow at large scales is generated by highly regulated local cellular rearrangements, often referred to as T1 processes. (c) Germ band extension in *Drosophila melongaster* is an example of the convergent extension morphogenetic movement. Cell neighbor exchanges are coordinated with the help of DV oriented stress cables, depicted above in red, that drive the formation of 4-fold vertices.

lateral ectoderm is referred to as Germ Band Extension (GBE) and has been the subject of a great deal of experimental work [81, 148, 36, 22]. GBE immediately proceeds after the ventral furrow invaginates and results in the approximate doubling of anterio-posterior (AP) length, at the expense of height along the dorso-ventral (DV) axis. Cellular rearrangements that compose the global flow [81] are coordinated by the presence of supracellular stress cables that orient along the DV axis of the lateral ectoderm [36], depicted in Fig. 4.1c. Stress cables are enriched with myosin II motors which are thought to actively contract intercellular junctions along the cable to either 4-fold vertices [91] or higher order structures termed rosettes [185]. E-cadherin plays a critical role in initializing oriented T1 processes exhibited by the simultaneous down-regulation along contracting edges and up-regulation on AP oriented cell interfaces [186]. The growth of new AP oriented edges from the de-novo 4-fold vertices is putatively driven by external stress along the AP axis emanating from the invagination and subsequent dorsal migration of the posterior midgut [36, 103].

In order to model the coordinated cellular rearrangements required for convergent extension flows such as GBE, we generalize the ATN model to explicitly include the effects of cadherin-mediated adhesion within the context of epithelial mechanics in this chapter. The extended model posits that myosin and cadherin recruitment to the cytoskeleton is positively regulated by cortical tension of the cell. Furthermore, we propose that cadherin activity is negatively regulated by traction forces at cellular interfaces. Traction is generated by an asymmetric distribution of cortical tension between adherent cells that must be supported by stress along cadherin dimers; a sufficiently strong traction force can lead to disassembly of the dimer [140]. Our postulated regulatory architecture of cytoskeletal mechanics is supported by the analysis of live-image data that allows simultaneous measurement of cadherin and myosin dynamics in-vivo – kindly provided by Thomas Lecuit [36].

Since myosin generates cortical tension, a sufficiently strong positive feedback on myosin recruitment leads to bistability within our model, allowing cytoskeletal edges to exist in either relatively high or low state of tension. Under this new condition, a nominally hexagonal lattice of cells can exist either in an isotropic state, with cells having regular hexagonal shapes, or in an anisotropic state with 2/3rds of cell edges in the high tension state with rectangular cell shape. Interestingly we will show that nucleation of an anisotropic state from an isotropic one can proceed through the formation of extended chains of high-tension edges, suggesting a possible mechanism for the formation of the stress fibers thought to be critical to the overall movement in-vivo [36].

Our model exhibits a secondary instability that drives the anisotropic hexagonal lattice towards formation of 4-fold vertices and higher order rosettes, a process known to occur during GBE and more general convergent extension flows [185]. This instability, in the context of our model, is driven by the presence of traction stresses [96] along the spontaneously generated stress fiber. High traction causes reduction of cadherin along the interface, which simultaneously increases tension and traction, resulting in the contraction of alternating interfaces along the fiber to zero length and thus initializing the T1 neighbor exchange process. We also find that within the model 4-fold vertices are stable provided they belong to a stress fiber. This means that the T1 process cannot be completed, unless in the presence of a global stress as experimentally observed [36]. Taken together, our extended ATN model proposes that myosin and cadherin dynamics, when connected to cellular mechanics, are sufficient to explain the morphological dynamics of early germ band extension.

4.1 Lateral ectoderm behaves as driven tension network during Germ-Band Extension

Before generalizing the ATN model of Chapter 2 to describe the morphological dynamics observed during GBE, we pause and ask if the tissue is empirically consistent with such a simplifying assumption. As presented in Section 5 of Chapter 2, the lateral ectoderm is geometrically compatible with an equilibrium lattice with averaged edge curvatures $\langle R_{\alpha\beta}^{-1} r_{\alpha\beta} \rangle \sim .08$, and thus is consistent with a tension-dominated cell array. Furthermore, the *Local Mechanical Inverse* algorithm outlined in detail in Chapter 3 (subject to the uniform pressure limit) was used to infer the dynamic map of tensions corresponding to the observed cell morphology, shown in Fig. 4.2b – hotter colors correspond to high relative tension. The variations in inferred tensions during GBE is up to two-fold, in agreement with laser ablation experiments [146]. The pattern of tension in Fig. 4.2b reveals clear anisotropy, with visible stress fibers, and thus is qualitatively consistent with earlier experimental studies [146]. With the developed tools, this comparison can easily be made quantitative. To this end, we examine the correlation between the inferred tension and junction-averaged myosin fluorescence intensity at $\approx 10^6$ junctions over the approximate 1 hour time lapse of GBE. In Fig. 4.2c we present the histogram of the myosin-tension correlation coefficient for each time-point.

The correlation coefficient of ~ 0.5 may not seem impressive at first glance, but there are multiple reasons why exact correlation is not to be expected. First, average junctional myosin level is not the only factor on which junctional tension depends, below we shall model an explicit dependence on the cadherin level that is empirically observed. We fully expect this still does not exhaust the list of other contributing factors. Furthermore, one must remember the noisy nature of measurements of both myosin fluorescence levels and cell geometry. Given this list of complications, it is quite remarkable that we find this level of correlation between observed local myosin levels and tension inferred from cell

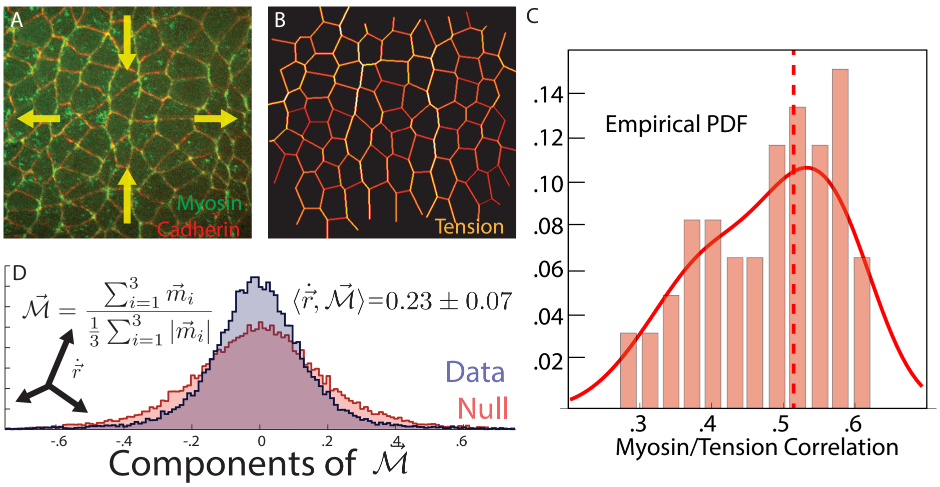

Figure 4.2: *The balance of forces during Germ Band Extension:* A) An apical cross section of the lateral ectoderm of the early Drosophila embryo (planar polarized distributions of myosin in green, and cadherin in red can be seen). Yellow arrows indicate the convergent extension flow in the moving reference frame of the tissue. B) Inferred pattern of relative junctional tensions – hotter colors correspond to larger tensions. Relative tensions span a factor of 2 in agreement with laser ablation experiments [146]. Supracelluler stress-fibers are visible. C) Histogram of the correlation coefficient between junctional myosin and inferred tension. Median, (dashed line) ≈ 0.5 based on analysis of $\approx 10^6$ junctions taken from each time-point. D) The distribution of components of the net myosin vector at a vertex (in blue), relative to a null (in red) constructed randomly from the data. KS p-value $\approx 10^{-60}$, indicating that myosin-dependent forces are closer to being balanced than expected at random. The unresolved component correlates with vertex velocity, $\dot{\vec{r}}$, indicating that unresolved myosin-dependent forces drive motion in the epithelial tissue.

geometry on the assumption of static force balance.

Lastly, if the cellular array is indeed close to equilibrium, then the dynamics of the ATN necessitates that myosin motors are at stall on each cytoskeletal bundles. As such, not only do we expect interfacial tensions to sum vectorially to zero at every vertex but similarly, myosin line densities should balance. We checked this empirically, as shown Fig. 4.2d. The probability density function of the magnitude of the normalized myosin vector residual, $\mathcal{M} = |\sum_{i=1}^{3} \vec{m}_i| / \frac{1}{3} \sum_{i=1}^{3} |\vec{m}_i|$, is shown in Fig. 4.2d in blue, where it is compared to the control in red constructed by combining triads of myosin densities and angles from distinct vertices in the field of view. Clearly, the $\vec{\mathcal{M}}_i$ residual estimated from observed junctional myosin is much closer to zero than expected by chance, as would be expected in the case of approximate balance of forces. Remarkably, despite the crude nature of our myosin level-based estimation of the net force, the correlation coefficient comes out to be $\approx 0.23 \pm 0.07$ with strong statistical significance (correlation coefficient of shuffled data is $\approx 0.04 \pm 0.06$), which strongly confirms our guiding approximation of the instantaneous mechanical state of the tissue.

4.2 Modeling positive mechanical feedback on cytoskeleton

In this section, we generalize the ATN model of epithelial mechanics to move beyond the phenomenological correlations presented above and describe the morphological dynamics of GBE and thus further understand the cell biological processes and mechanical forces that drive convergent extension. The spontaneous emergence of supracellular stress cables, the correlated myosin and cadherin dynamics resulting in a complementary expression pattern, and the observed morphological transition from hexagonal to square celllar packing can not be explained by the ATN model as it stands, without invoking fine-tuning of myosin patterning. We instead look for simple mechanisms that could explain such phenomena.

As before, we assume vertex dynamics are relaxational and driven by imbalanced cortical tension

$$\nu \dot{\boldsymbol{r}}_i = \sum_{\{j\}_i} T_{ij} \hat{\boldsymbol{r}}_{ji} \tag{4.1}$$

Similarly, we model each cortical bundle as an active elastic element such that $T_{ij} = K(r_{ij} - \ell_{ij})$ where the dynamics of ℓ_{ij} is driven by myosin contractility of the actin bundle. Here we postulate the adhesive force, mediated by trans-cadherin dimers, loads the myosin motors that cross-link actin filaments within the cytoskeletal bundles of each cell.

$$\ell_{ij}^{-1} \dot{\ell}_{ij} = \tau_\ell^{-1} W \left[\frac{T_{ij} + \lambda c_{ij}}{m_{ij} a T_s} \right] \tag{4.2}$$

Eq. 4.2 includes the effect of adhesion λc_{ij} which appears in the argument of the walking kernel $W[x]$ initially proposed in the original model. λ is taken to be a phenomenological parameter that controls the strength of the interaction, although it is presumably regulated by the AJ-actin binding proteins such as the catenin complex [122]. While Eq. 4.2 is an assumption of the model, the effect agrees with biophysical intuition and has been observed experimentally [21]. At equilibrium, we expect vertices to be stationary and myosin motors to be at stall, now set by the modified stall tension $T^*_{ij} = aT_s m_{ij} - \lambda c_{ij}$. Cadherin acts as an effective adhesive force and thus negatively contributes to line tension. It is known that cortical tension positively regulates cytoskeletal myosin expression within the lateral ectoderm during GBE [53]. As we seek to model myosin dynamics on an intermediate time-scale, we propose tension-dependent recruitment of junctional

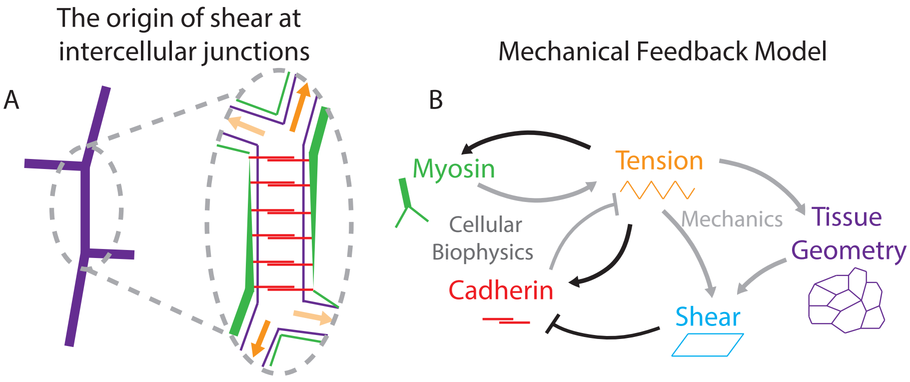

Figure 4.3: The origin of shear stress at a cell-cell contact and model for mechanical feedback. a) Asymmetric configurations of tensions in neighboring junctions are supported by gradients in cortical myosin in green (inset). The transfer of tension from one cell to the other generates shear stresses and loads cadherin bonds. b) Three key ingredients of our model: the mechanics of a tissue, the biophysics of the molecular generation of stresses, and mechanical feedback (in black).

myosin in place of the slow strain-rate dependent explored in Chapter 2. Specifically, myosin densities are now assumed to evolve according to the simple kinetic law

$$\dot{m}_{ij} = \Gamma_m + k_m \frac{T_{ij}^n}{T_{ij}^n + T_m^n} - \tau_m^{-1} m_{ij} \tag{4.3}$$

The exact form chosen for the tension-dependent recruitment of Eq. 4.3 is inconsequential to the resultant analysis; we simply require it be a generic sigmoidal form.

As with myosin, it has been experimentally suggested that cadherin is recruited to adherens junctions in response to increases in cortical tension [98, 157, 161]. Furthermore, single molecule experiments show caderin assembly and disassembly rates intimately depend upon the force applied across the dimeric bond [140]. The sign of the interaction depends upon the conformation of bond; catch and slip cadherin bonds will disassemble slower and faster respectively in the presence of an applied force [98, 46]. We assume cadherin bonds in the lateral ectoderm during GBE are predominately slip bonds and thus disassemble in the presence of force. This assumption is critical to the instability explored later in this chapter and should be taken as an easy prediction to verify experimentally.

$$\dot{c}_{ij} = \Gamma_c \frac{T_{ij}^n}{T_{ij}^n + T_c^n} - \left[\tau_c^{-1} + k_c \frac{\Sigma_{ij}^n}{\Sigma_{ij}^n + \Sigma_*^n}\right] c_{ij} \tag{4.4}$$

Σ_{ij} denotes the average load applied per cadherin molecule expressed on edge i, j. In the context of the vertex model, Σ_{ij} denotes the traction stress, or the load that must be distributed by cadherin molecules in order to hold the attached cortices of neighboring cells to a fixed interfacial tension. Following [29], we re-examine a microscopic picture of a cell junction, shown in Fig. 4.4 Denoting the cortical tension of cell α to be Γ_α, we

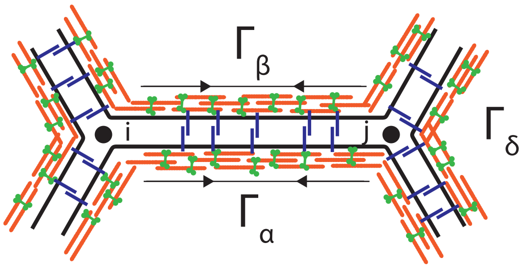

Figure 4.4: The average shear stress at a cell-cell contact applied across cadherin molcules in the context of a vertex model. Recall that cadherin mechanically couple neighboring actin bundles to maintain a constant cortical tension across. Thus, asymmetries of tension *across* the interface must be supported entirely by cadherin molecules. We define this to be junctional traction.

require that the composite junction is held at constant tension $T_{\alpha\beta} = \Gamma_\alpha(x) + \Gamma_\beta(x)$, but allow each cell's cortical tension to vary across the edge. The average shear force on each actin bundle belonging to cell α, β is $\Sigma_{ij} = [\Gamma_\alpha(r_{\alpha\beta}) - \Gamma_\alpha(0)]/r_{\alpha\beta}$. Assuming the cortical tension for each cell's cytoskeleton is continuous across vertices, it is straightforward arithmetic to derive

$$\Sigma_{ij} = \frac{|T_{\alpha\gamma} + T_{\beta\delta} - T_{\gamma\beta} - T_{\alpha\delta}|}{r_{ij}} \tag{4.5}$$

Taken together, eqns. 4.1-4.5 fully specify the dynamics of the network.

4.3 Empirical support for mechanical regulation of myosin and cadherin

In this section, we use a correlation analysis to provide evidence for each term of the above biochemical equations of motion. Providing empirical support for the posited dynamics, eqns. 4.3-4.4 is obscured by the interactions implicit in the phenomena; cytoskeletal protein expression, forces, and cellular geometry are known to mutually effect one another which confounds our analysis if we would like to study the interaction between myosin and cadherin expression while controlling for their known tension-dependent recruitment (which could dominate the correlations). This presents an important problem that warrants careful consideration: how can we isolate the *direct* pairwise correlations between two stochastic variables, X_1 and X_2, that is not mediated through any auxiliary field X_3? One can easily check that the canonical Pearson correlator measures the *effective* two-point correlator between X_1 and X_2 and thus contains information of the interaction averaged over all potential paths. We make this concrete by considering a generic trivariate Gaussian distribution.

$$\rho(X_1, X_2, X_3) = \frac{1}{\mathcal{Z}} \exp\left[-\frac{1}{2}\boldsymbol{X}^T A \boldsymbol{X} + \boldsymbol{\mu} \cdot \boldsymbol{X}\right] \tag{4.6}$$

$\mathcal{Z}$ is the normalization constant. Pearson's correlation coefficient between X_n and X_m is easily computed to be

$$\rho_{nm} = \frac{A^{-1}_{nm}}{\sqrt{A^{-1}_{nn}A^{-1}_{mm}}} \tag{4.7}$$

This involves the inverse of the interaction matrix A and thus depends on all interactions between variables n and m! Statisticians have dealt with this problem by defining partial correlators [6], which in the present context of a trivariate Gaussian would return the desired result. Importantly, the partial correlator only controls for bilinear interactions. To help disentangle generic, non-linear mediated interactions, we define the *conditioned cross-correlator*

$$\rho_{12|3} = \langle X_1, X_2 | X_3 \rangle = \left\langle \frac{(X_1 - \mu_{X_1|X_3})(X_2 - \mu_{X_2|X_3})}{\sigma_{X_1|X_3}\ \sigma_{X_1|X_3}} \right\rangle \tag{4.8}$$

where $\mu_{X|X_3}$, $\sigma^2_{X_1|X_3}$ are respectively the average and the variance of X_1 conditioned on X_3. Angular brackets in Eqn. 4.8 indicate the average of our conditional cross correlator (CCC) taken over the marginalized distribution of X_3. Conditioning X_1 and X_2 on X_3 controls for the contribution of latter variable to the fluctuations of X_1 and X_2, improving the ability to detect *direct* correlation of the latter two, even in the presence of non-linear interactions between X_1/X_2 and X_3.

Of course, there is no free lunch. Construction of the CCC requires large amounts of data to adequately sample moments of the conditioned joint distribution. In all empirical results that follow, we partition the X_3 axis into bins of varying widths that each contain 30 data points, compute the correlation coefficient within each bin, and then average over to estimate the true CCC, leveraging the high-throughput advantage of the utilized automated image analyses.

To illustrate the utility of conditioned cross correlation analysis in-vivo, we use it to isolate the individual contributions of myosin and cadherin to inferred tension. We find that conditioning on the cadherin level increases the myosin-tension correlation coefficient from $\langle m, T\rangle = 0.49$ to $\langle m, T|c\rangle = 0.58$. Conditioning on myosin, we find $\langle c, T|m\rangle = -0.15$ - a negative direct contribution of cadherin to tension, which is otherwise obscured by the much larger contribution of myosin ($\langle c, T\rangle = 0.29$). This lends strong empirical evidence to the predicted negative relation between junctional cadherin and tension!

Cytoskeleton-Tension

$\langle m, T\rangle$	0.49 [0.41,0.53]
$\langle m, T\|c\rangle$	0.56 [0.5,0.61]
$\langle c, T\rangle$	0.29 [0.22,0.39]
$\langle c, T\|m\rangle$	-0.15 [-0.18,-0.08]

Tension-dependent Feedback

$\langle \dot{m}, T\|m\rangle$	0.11 [0.08,0.15]
$\langle \dot{c}, T\|c\rangle$	0.17 [0.13,0.2]

Equilibration

$\langle \dot{m}, m\|T\rangle$	-0.21 [-0.16,-0.27]
$\langle \dot{c}, c\|T\rangle$	-0.19 [-0.16,-0.24]

Shear-dependent Feedback

$\langle \dot{c}, \Sigma_+\rangle$	-0.24 [-0.19,-0.31]
$\langle \dot{c}, \Sigma_-\rangle$	-0.02 [-0.05,0.02]

Figure 4.5: *Conditioned Cross Correlation Analysis:* Our analysis of myosin and cadherin average junctional fluorescence, and inferred junctional tissues is present in four parts 1) The relationship between myosin and cadherin, and tension, 2) The direct positive feedback of tension on myosin and cadherin produces the indirect correlation of myosin and cadherin levels, 3) Evidence of a balance between syntheses and degradation of junctional cytoskeletal levels, and 4) The shear stress enhancement of cadherin dissociation.

Furthermore, we find support for tension-dependent recruitment of myosin and cadherin - $\langle \dot{m}, T|m\rangle$ and $\langle \dot{c}, T|c\rangle \sim .15$. CCC analysis also indicates the presence of equilibration dynamics – $\langle \dot{m}, m|T\rangle$ and $\langle \dot{c}, c|T\rangle \sim -.2$ – supporting our assumption that junctional myosin and cadherin constantly degrade in time. Equilibrium levels are thus produced through a balance of tension-depenent synthesis and degradation. Conditioning is necessary to detect these direct pair-wise correlations.

CCC also allows us to test whether the average load per cadherin enhances the dissociation rates of cadherins. Our analysis strikingly confirms that junctions with high shear stress (junctions along stress fibers) display a negative correlation between cadherin recruitment and shear-stress dependent load – $\langle \dot{c}, \Sigma_{+} \rangle \sim -.25$. Junctions with low shear-stress dependent load (junctions aligned orthogonal to stress fibers) display little correlation – $\langle \dot{c}, \Sigma_{-} \rangle \approx 0$. $\Sigma_{\pm}$ was defined by taking values above and below the median. Rate of change of myosin levels display zero correlation with junctional shear.

Conditioning, as well taking derivatives of the largely stochastic fluorescence time traces, ought to be taken under consideration when reviewing the reported correlations. Furthermore, we note that effects can be obscured by the temporal resolution of the data (taken every $\sim$ 30 seconds) – if kinetic equilibration timescales are shorter than the temporal resolution of the data then no signature of far from steady-state effects can be meaningfully measured. We note this is the first real example of such correlative tests of a vertex-based model in the literature and represents a great quantitative first step to test postulated dynamics of biomechanical feedbacks in-vivo.

4.4 Effects of positive feedback between myosin and tension on tissue dynamics

The correlation analysis presented above suggests our model may be a reasonable approximation, but it is the dynamical consequences of the model and their agreement with the in-vivo dynamics of GBE that will confirm its usefulness. Hence, we shall analyze the consequences of the two postulated modes of mechanical feedback on cytoskeletal chemistry: (i) tension-dependent recruitment of myosin and (ii) the enhanced detachment of cadherin due to shear stresses at junctions. This section will focus on the former.

To gain intuition on the role of positive feedback between myosin and tension, we temporarily neglect the role of cadherin ($\lambda = 0$). The fixed point of the tissue dynamics is given by

$$T_{ij} = [a\tau T_s \Gamma]\, m_{ij} \qquad \text{and} \qquad m_{ij} = 1 + \gamma \frac{m_{ij}^n}{m_{ij}^n + m_*^n} \tag{4.9}$$

We have rescaled $m_{ij} \to m_{ij}/\tau\Gamma$, $\gamma = k_m/\Gamma$, and defined $m_* \equiv T_m k_m / a T_s \Gamma$. The accessible fixed points for each junction are the roots of the $n+1$ order polynomial

$$m^{n+1} - [\gamma + 1]\, m^n + [m_*^n]\, m - m_*^n = 0 \tag{4.10}$$

Provided $\gamma m_*^n \ll 1$ (in the large n limit $1 < m_* < 1 + \gamma$), dominant balance dictates that the three real roots behave as

$$m_- \approx 1 \qquad m_0 \approx {m_*}^{n/n+1} \qquad m_+ \approx 1 + \gamma \tag{4.11}$$

$m_\pm$ are the stable low and high states respectively that are separated by the unstable myosin level m_0. If $m_* < 1$ or $m_* > 1 + \gamma$ then only the low/high fixed point is stable.

The generic fixed point structure is illustrated graphically in Figure 4.6.

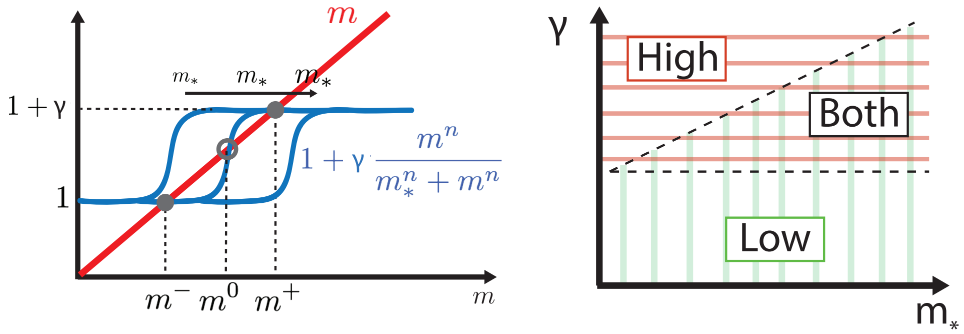

Figure 4.6: *Fixed-point analysis of myosin kinetics:* Intersection of the blue curve, the first two terms in Equation 4.3, and the red curve, the third term in Equation 4.3, constitute the fixed points of the myosin kinetics. The generic phase diagram is shown on the right. Large region of phase space exhibits bistability.

Provided we are in the region of bistability, the high myosin/tension state can nucleate and invade the surrounding tissue composed of junctions stabilized at the low level. Such a situation is expected to occur when an individual junction is driven to high myosin; it will contract and pull on connected junctional actin bundles. This will induce an elastic deformation and thus increase the tension of each junction, which provided it is a large enough perturbation, recruits additional myosin to high levels, and so on. This can be made exact by utilizing the continuum limit of the 1D ‘Active Chain’ model presented in Chapter 2 in the limit of instantaneous myosin kinetics and the linearized walking kernel so that

$$\partial_t T(x,t) = \partial_x^2 T(x,t) - \kappa \left[T - m(T)\right]$$

$$m(T) = \tau\Gamma + \tau K \Theta\left(T - T_m\right) \tag{4.12}$$

For ease of calculation, we approximate the Hill function in the $n >> 1$ limit as the Heaviside step function. We restrict our attention to traveling wave solutions $T(x,t) = T(x-vt) = T(\xi)$

$$\partial_\xi^2 T + v\partial_\xi T - \kappa\left[T - \tau\Gamma - \tau K\Theta\left(T - T_m\right)\right] = 0 \tag{4.13}$$

By construction, the high/low tension state exists to the left/right such that $T(-\infty) = T_{high}$ and $T(+\infty) = T_{low}$. The global solution can be obtained by solving both resultant linear equations independently in the left and right half-planes and enforcing continuity at $\xi = 0$.

$$T(\xi) = \begin{cases} \tau\Gamma + \tau K - \tau K\left[\frac{|\alpha_R|}{|\alpha_R|+\alpha_L}e^{\alpha_L\xi}\right] & \text{if } \xi < 0 \\ \tau\Gamma + \tau K\left[\frac{\alpha_L}{|\alpha_R|+\alpha_L}e^{-|\alpha_R|\xi}\right] & \text{if } \xi > 0 \end{cases} \tag{4.14}$$

We have defined $\alpha_{L,R} \equiv (-v \pm \sqrt{v^2+4\kappa})/2$ for notational convenience - it directly relates the localization of the wavefront to its propagation speed. As we've defined the location $\xi = 0$ as the transition between the high and low state, we must enforce the amplitude of our solution is self-consistent. As the amplitude is directly related to the velocity, we recover the speed of the wave to be $v = \sqrt{\frac{4\kappa}{1-A^2}}A$ where $A \equiv 1 - 2\frac{T_M - \tau\Gamma}{\tau k_m}$. We note this a particularly simple example of the general velocity selection problem in the context of nonlinear diffusion [38].

While this discussion describes the growth phase of a first order phase transition in one dimension, we find that the initial nucleation event is critical to the nature of the front propagation in higher dimensions. Simulations of the model in 2D demonstrate that if the nucleation of a high myosin state occurs isotropically in a single cell, the growth of a front occurs in two dimensions, shown in Fig. 4.7d-e. Alternatively, if nucleation of a high myosin state occurs anisotropically in a single cell, then growth of a cable emerges, as displayed in Fig. 4.7a-c. Intensity of colors correspond to tension levels.

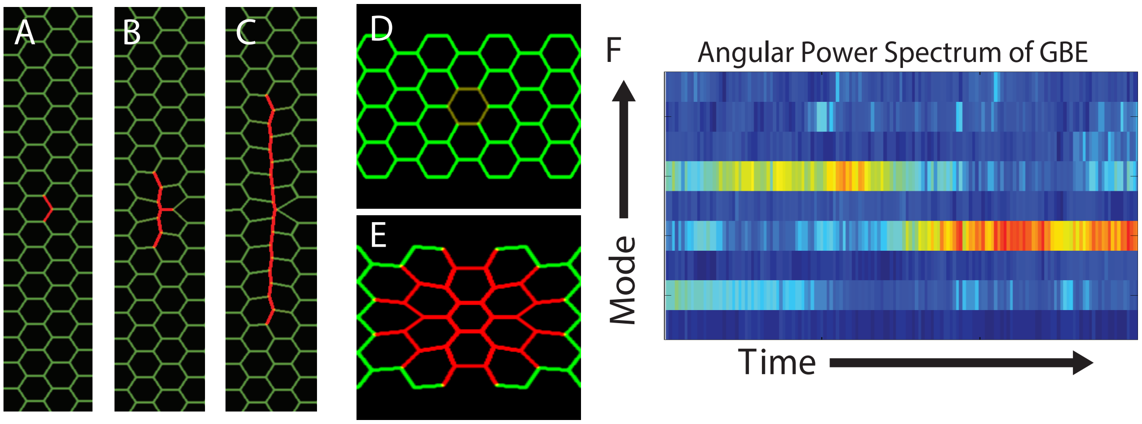

Figure 4.7: Myosin bistability can drive the propagation of a high tension/myosin state into a lattice stabilized at low tension/myosin. The symmetry of the nucleation event determines the dimensionality of the front: (a-c) anisotropic nucleation drives generation of a one-dimensional stress fiber while d-e) exhibits the two-dimensional front growth from an isotropic nucleation drives. f) The angular power spectrum (discrete Fourier transform of interior polygon angles) averaged over all cells throughout time during GBE displays a discrete transition from hexagonal to rectangular geometry.

As shown in Fig. 4.7f, the lateral ectoderm undergoes a collective transition from a predominately hexagonal cellular array into a 'square' lattice with super-cellular stress cables running along the DV axis of the embryo, consistent with observations of previous studies [187, 16]. While the proposed positive feedback between myosin and tension is sufficient to explain the self-assembly of a single cable, myosin fluctuations must themselves be patterned to achieve the observed long-range order. This prerequisite is completely consistent with experimental observation that pulsatile myosin is driven to DV oriented junctions [107]. Given patterned myosin fluctuations along the DV axis, we observe that positive mechanotransduction of myosin is sufficient to recapitulate the cellular lattice

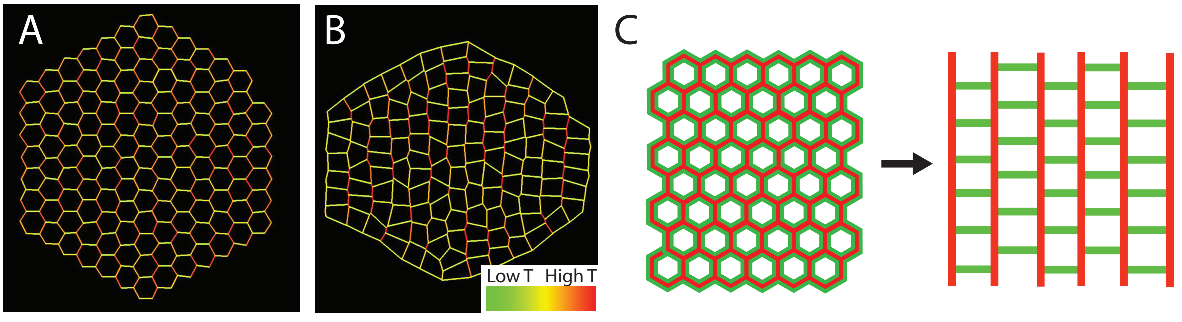

Figure 4.8: *Patterned myosin fluctuations recapitulate the collective lattice transition during GBE:* a-b) Given an initial hexagonal cellular array, either with weak initial enrichment of myosin along the DV axis, or dynamic myosin pulses that preferentially hit DV oriented junctions, we reconstruct the observed morphological transition to a square lattice, characterized by DV oriented stress cables, shown in (b) using eqns. 4.1-4.5 in the bistable regime of myosin kinetics. The cartoon representation of the initial and final cell morphologies is shown in (c).

transition observed *in-silico* as shown in Fig. 4.8a-b. Full detail on the simulation can be found in the appendix. Importantly, these results hold true in the presence of finite cadherin contribution to cortical tension ($\lambda > 0$). This is entirely consistent with our postulated cadherin kinetics; the hexagonal morphology exhibits negligible tissue shear. Once geometric anisotropy arises concomitant with the transition to square cell morphology, shear-dependent detachment of cadherin drives the subsequent dynamics.

4.5 Secondary instability of stress fibers: Cadherin regulation drives 4-fold formation

Assembly of a high tension supracellular cable will generate large shear stresses Σ along all composite junctions. This is manifest in Eq. 4.5, which in the case of 1D stress fiber as shown in Fig. 4.8 will limit to $\Sigma = \frac{2\Delta T}{r}$, where $\Delta T = T_{cable} - T_0$, denotes the difference between the tension of the stress cable and its supporting junctions (shown as green edges in Fig. 4.8). Homogeneous cables are expected to be unstable. As the 1D cable is under a large shear stress Σ, cadherin is expected to dissociate from the actin cortex. Provided $\lambda > 0$, this will *increase* the cable's tension resulting in a larger shear stress! The effective positive feedback loop between cortical tension and shear in $1D$ can drive alternating edges to zero length and thus initializes a T1 process.

We check this intuition analytically by specializing to the extreme example that $T_0 = 0$, which exactly corresponds to the case illustrated in Fig. 4.8c. Under this assumption, each stress fiber is decoupled from its neighbors and can be studied in 1D isolation using the 'Active Chain Model' presented in Chapter 2. Furthermore, the traction force of edge n along the cable simplifies to $\Sigma_n = (T_n + T_{n-1})/r_i$. Once linearized around the uniform fixed point of high myosin $r_n = r$, $m_n = m \approx \tau\left[\Gamma + k_m\right]$, and $c_n = c$, the equations of motion are (with time re-scaled in units of ν)

$$\begin{pmatrix} \delta\dot{r}_n \\ \delta\dot{T}_n \\ \delta\dot{m}_n \\ \delta\dot{c}_n \end{pmatrix} = \begin{pmatrix} 0 & \nabla_{nn'} & 0 & 0 \\ 0 & \nabla_{nn'} - \kappa\delta_{nn'} & \kappa\delta_{nn'} & -\lambda\kappa\delta_{nn'} \\ 0 & \epsilon_m\delta_{nn'} & -\tau_m^{-1}\delta_{nn'} & 0 \\ \epsilon_H\Sigma\delta_{nn} & \epsilon_c\delta_{nn'} - \frac{\epsilon_H}{r}D_{n,n'} & 0 & -\bar{\tau}_c^{-1}\delta_{nn'} \end{pmatrix} \begin{pmatrix} \delta r_{n'} \\ \delta T_{n'} \\ \delta m_{n'} \\ \delta c_{n'} \end{pmatrix} \tag{4.15}$$

We have defined $\kappa \equiv \frac{\ell^*}{\nu\tau_\ell m a T_s}$, $\epsilon_m \equiv \partial_T \frac{T^n}{T^n + T_m^n}\Big|_T$, $\epsilon_c \equiv \partial_T \frac{T^n}{T^n + T_c^n}\Big|_T$, $\epsilon_H \equiv \partial_\Sigma \frac{\Sigma^n}{\Sigma^n + \Sigma_m^n}\Big|_\Sigma$, $\bar{\tau}_c^{-1} \equiv \tau_c^{-1} + k_c\frac{\Sigma^n}{\Sigma^n + \Sigma_*^n}$, and $D_{nn'} = \delta_{n,n'+1} + \delta_{n,n'-1}$ to simplify notation. As we have assumed the cable is in the high myosin state, $\epsilon_m << 1$, myosin dynamics are saturated and can be ignored from the following analysis. Furthermore, due to translational invariance, the linearized equations of motion can be diagonalized over space by considering its Fourier transform with $k \in [0, \frac{2\pi}{N}, ..., \frac{2\pi(N-1)}{N}]$.

$$\begin{pmatrix} \delta\dot{r}_k \\ \delta\dot{T}_k \\ \delta\dot{c}_k \end{pmatrix} \approx \begin{pmatrix} 0 & 2(\cos k - 1) & 0 \\ 0 & 2(\cos k - 1) - \kappa & -\lambda\kappa \\ \epsilon_H \Sigma & \epsilon_c - \frac{2\epsilon_H}{r}\cos k & -\bar{\tau}_c^{-1} \end{pmatrix} \begin{pmatrix} \delta r_k \\ \delta T_k \\ \delta c_k \end{pmatrix} \tag{4.16}$$

For general parameter regimes, the matrix of Eq. 4.16 exhibits at least one positive, real eigenvalue and thus we conclude stress cables are unstable in the presence of the posited cadherin dynamics. However as shown in Fig. 4.9, the nature of the instability exhibits two major phases characterized by the dominant wavenumber of instability, denoted k_{max}. In the $k_{max} = 0$ phase, the shear-dependent dynamics are dominated by global positive feedback: reducing cadherin uniformally along the cable will increase tension uniformally, thus increasing shear-dependent cadherin depletion. As shown in Fig. 4.9, we expect this to be true in the limit that $T_{cable} >> 2$. In the $k_{max} = \pi$ phase, the shear-dependent dynamics are dominated by alternating junction length modulation along the cable. Cadherin on the contracting/extending junctions is depleted/recruited such that tension along the cable is kept roughly constant. As experimental observations place $T_{cable} \sim 2T_0$ [146], it is reasonable to expect GBE to operate in this regime.

Fig. 4.10a clearly demonstrates that supracellular stress fibers exhibit inhomogeneous contractions during GBE - junction lengths along the cable exhibit large variances in edge length. A characteristic snapshot of simulations of our mathematical model, chosen in a parameter regime that supports inhomogeneous contraction, is shown in Figure 4.10b, and bears a qualitative resemblance to Fig. 4.10a. This simple minded and limited comparison of the model to observations lends *some* evidence to the presence of a secondary instability along stress fibers that drives inhomogeneous contractions of

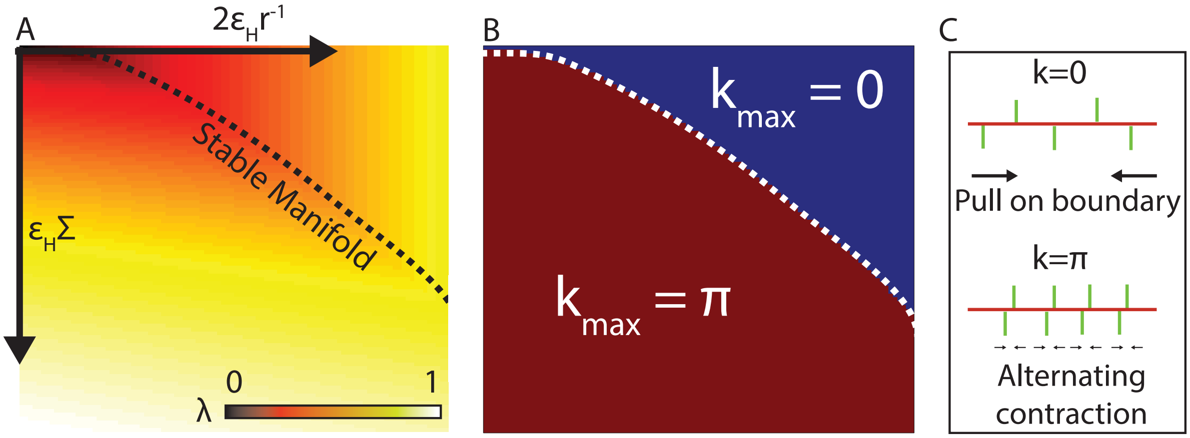

Figure 4.9: a-b) The maximum eigenvalue of dynamics Eq. 4.16, shown in the $(\epsilon_H \Sigma, 2\epsilon_H r^{-1})$ plane (with $\tau_c^{-1} = .1$, $\epsilon_c = .01$, $\lambda = .1$ and $\kappa = 10$). Two qualitatively different regimes of instability, delineated by the maximally instable wavenumber, shown in (b). Perturbing the other four parameters leaves the generic two-phase diagram invariant but changes both the position and shape of the boundary between them. The $k_{max} = 0$ regime is characterized by global rescaling of cadherin levels, effectively pulling on the boundary. $k_{max} = \pi$ regime denotes an alternating contraction of junctions along the fiber to zero length.

junctions along it. It certainly would be interesting to investigate scenarios where uniform contraction of stress fibers is observed and delve into the differential molecular regulation of cytoskeletal kinetics.

Regardless of the microscopic nature of a T1 process, a short junction along a stress fiber will necessarily be subject to high shear stresses, driving it to “zero” length. Short junctions along stress fibers are therefore unstable, imparting stability to a 4-fold vertex. This is observed in simulations, as well as in the long lifetimes of 4 fold vertices in a variety of in epithelial tissues, including the lateral ectoderm. Our results do not preclude resolutions of 4-fold vertices in the absence of stress-fibers, a neighbor exchange event often seen early on in GBE.

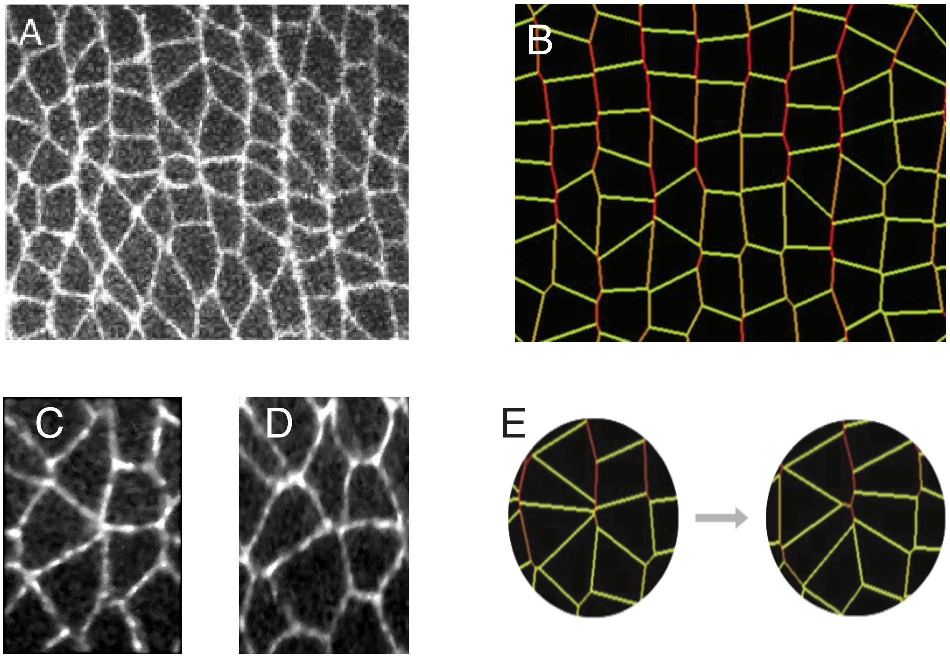

Figure 4.10: *Inhomogeneous contraction of stress-fibers, and rosette dynamics:* A) A characteristic snapshot of the epithelial lattice, observed through a live-reporter of endogenous E-cadherin, during germ band extension, after the formation of stress fibers. Inhomogeneous junctional lengths are typically observed, along with an over-abundance of 4-fold vertices. B) Lattice simulations of the model in the parameter regime supporting inhomogeneous junction contractions along stress-fiber qualitatively resembles observed lattices, with an over abundance of 4-fold vertices. C-D) Rosette, higher-fold vertex structures, are generically observed during GBE. E) Within the context of the model, rosettes are generated through the stability of four-fold vertices, and their resolution is permitted through the generation of a new junction along a low-shear configuration.

Rosettes, higher-fold vertices, as shown in Fig. 4.10c-d, are observed commonly during GBE [185] and present a route where a junction can emerge in a low shear configuration in the presence of a stress fiber. Rosette formation, and its resolution, is recovered by our simulation with no additional ingredients to the ones already discussed in this study. Fig. 4.10e illustrates an example of such an event. What permits an intercalation event through a rosette-like intermediary structure? Unlike a junction resolved from a 4-fold intercalation event, a rosette can generate a new junction that isn't under high shear, thereby escaping the secondary, cadherin-drive, instability. As formulated, this is the only pathway in which a T1 process can complete with a neighbor exchange.

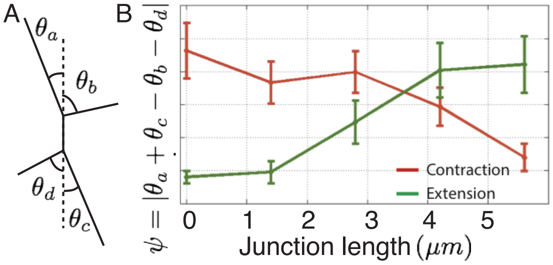

Figure 4.11: *Geometric anisotropy and directionality during cellular exchange*: Our model suggests that geometric parameter, ψ, as defined in panel A to have distinct dynamics along contracting and extending junctions. In particular, our model predicts that shrinking junctions ought to display $\psi \approx 1$, while extending junctions following T1 events ought to display $\psi \approx 0$. This qualitative difference is observed in the data, as shown in panel B.

Taking a step back from the details of the physical structures responsible for neighbor exchanges, within our mathematical model, junctional contractions are predicted to occur along asymmetric/high-shear configurations, while junctional extensions are only permitted along symmetric/low-shear configurations. Geometry asymmetry along a given junction is measured by parameter $\psi = |\theta_a + \theta_c - \theta_b - \theta_d|$. This qualitative prediction is validated by analysis of live-image time-lapse of GBE, displayed in Fig. 4.11. In particular, contracting junctions develop geometric asymmetry, while extending junctions evolve towards the symmetric hexagonal state.

4.6 Beyond correlation-based validation

In this chapter, we presented statistical analyses that support the existence of mechanical feedback on biochemical expression, and motivate the proposed functional form for kinetic models for myosin and cadherins at junctions. We note that the correlation analysis used can at best be suggestive and thus the final proof of the validity of the proposed model lies within rigorous experimental validation of the predictions of the model and the molecular mechanisms they support. This is a feature, not a bug! The model explains observed tissue phenomena with simple quantitative laws that make generic predictions insensitive to parameter values that are immediately accessible to experimentalists. The first is that tension-dependent recruitment of myosin generates bistability in myosin levels at a junction. In analogy to first order phase transitions known in condensed matter systems and excitable media, the high tension/myosin state is predicted to invade a lattice stabilized at the lower fixed point. The dimensionality of the propagating front is a function of the nature of the nucleation event. In particular, isotropic nucleation events will drive two-dimensional front propagation, whereas an anisotropic nucleation event will drive the self-assembly of a stress fiber. Using modern optogenetic tools, or sufficiently large mechanical perturbations via laser ablation, this prediction should be testable by directly probing the predicted bistability, and thus hysteresis, of myosin dynamics.

Following the observed transition in collective cellular morphology, what are the dynamics of stress fibers themselves? Since localized stress fibers generate large shear stresses at the corresponding cellular interfaces, we analyzed the consequence that stresses enhance cadherin detachment in a load dependent manner. We find two qualitatively distinct possibilities: i) homogeneous stress fiber contraction that will pull neighboring tissues producing large overall fiber contraction and large scale deformations, or ii) inhomogeneous stress fiber contractions, where every other junction contracts to "zero" length at the expense of its neighbors that extend, producing no overall fiber contraction, but instead drives cellular intercalation events. Following observations made in a number of previous studies, we see evidence of the second mode of fiber contraction during GBE, suggesting that cellular intercalations rather than overall tissue deformation is the dominant form of morphogenesis occurring during GBE. Further analysis of this model may lead to experimental possibilities that could move the lateral ectoderm into the first regime.

An unavoidable prediction of our model is that 4-fold vertices are stable in the presence of the high shear forces along a stress fiber. As such, T1 events along stress fibers either have to a result of stress-fiber dissipation or the formation of higher order vertices, termed rosettes, that permit the resolution of junctions along stress fibers along a low shear configuration. This qualitative prediction is confirmed by a geometric order parameter based analysis of large numbers of contracting and extending junctions.

In summary, clearly genetic patterning produces biases in the structure and kinetics of epithelial tissues undergoing morphogenesis. The central issue addressed in this chapter is whether mechanical feedback within a tensed epithelial tissue can sustain emergent features that play an important role in epithelial morphogenesis. We believe that suggesting specific and falsifiable modes of mechanical feedback, and connecting them to the cellular and tissue level processes that they might be responsible for is immensely useful in guiding future experiments.

Chapter 5

Continuum model of active mechanics and morphogenetic flow

Drosophila embryogenesis has historically been partitioned into autonomously acting tissues, in which intrinsic cell-specific behavior drives shape transformations of the tissue [109]. Thanks to *in-toto* imaging [93], we now have unprecedented experimental access to morphogenesis at the global scale and can begin to probe the interactions between these putative autonomous domains. For example, the non-local interactions between the formation of the ventral furrow (VF), posterior midgut invagination [165], and the convergent extension of the lateral ectoderm during early Drosophila embryogenesis remain a subject of active study which requires quantitative multi-scale analysis [36, 144, 148].

To address this particular question, we utilize light-sheet microscopy data obtained and analyzed in collaboration with Sebastian J. Streichan (KITP, UCSB), that provides detailed three-dimensional time-lapse movies of Drosophila gastrulation. For approximately ninety minutes after formation of the cephalic furrow, the embryonic tissue forms a 2D epithelial layer with minimal folds into the third dimension [165]. Hence, the global morphogenetic flow can be adequately captured by cellular dynamics on a static apical surface [73]. We find that Drosophila gastrulation is characterized by three major flow geometries, shown in Fig. 5.1. Preceding the formation of the VF, cells move dorsally with no internalization. At the onset of VF formation, cells rapidly move towards the ventral midline to form the future mesoderm of the animal, as was described in Chapter 2. After VF formation has completed, the Drosophila embryo begins to elongate its germ band (GBE), characterized by a hyperbolic flow typical of convergent extension. Fluorescently labeling myosin shows that each of the three flow field configurations is accompanied by an idiosyncratic spatial myosin distribution. Can we use quantitative modeling to connect these two empirical fields?

In preceding chapters, we phenomenologically modeled the activity of cytoskeletal actomyosin bundles in the context of tissue-scale mechanics by generalizing the classical vertex model to directly include mechanical feedbacks on cadherin and myosin expression. The discrete model is informative when probing questions at cellular scales, as was done in our analysis of Drosophila VF formation and GBE in Chapter 2 and 4 respectively. However, when considering morphogenesis of large-scale structures such as organs or entire bodies constituted from thousands of mechanically coupled cells, it is helpful to have a coarse-grained continuum model.

To this end, in this Chapter we define a coarse-grained description of the ATN model with the explicit purpose of relating the first ninety minutes of global cellular flow during Drosophila gastrulation to the spatial distribution of myosin II. Specifically, we assume the embryonic epithelial tissue is a pre-strained elastic solid whose intrinsic geometry adiabatically evolves as a result of internal rearrangements of the actomyosin cytoskeleton. At intermediate time-scales, the model predicts the tissue to effectively behave as a compressible viscous fluid driven by myosin imbalances; this picture is borne out by the data. As before, its predictions on longer time-scales will require new experiments, however we fully expect this model to be immediately applicable to many developing systems.

5.1 Active Tension Network model at the mesoscopic scale

The ATN model presented in Chapter 2 formulated tissue mechanics as a discrete network of pre-strained elastic elements that plastically deform in response to active actomyosin contractility. As such, the instantaneous mechanical energy was given by

$$E\left[\{\boldsymbol{r}_i\}\right] = \frac{1}{2}\sum_{<i,j>} K\left[r_{ij} - \ell_{ij}\right]^2 \tag{5.1}$$

where unlike classical passive materials, ℓ_{ij} was allowed to adiabatically flow, regulated by the local linear myosin density m_{ij}, which itself was taken to be a dynamical variable. As seen in Chapter 4, different mechanochemical feedback characteristics can lead to macroscopically different tissue morphologies. While the network-level model proved illuminating whilst probing morphogenesis at the cellular scale, it is unclear if such precision is required or even exhibited at the level of morphogenesis of organs and entire bodies. For example, it has been shown that molecular patterns and cellular rearrangements are highly reproducible when averaged on patches of ~ 100 cells, hereafter referred to as the mesoscopic scale, despite considerable variability at the single-cell level during metamorphosis of both the Drosophila scutellum and pupal wing [18, 51]. We thus focus our attention to coarse-graining our microscopic model.

Mathematically, the above statements are tantamount to assuming the underlying microscopic degrees of freedom are well-approximated by *continuum fields*, representing the reproducible mesoscopic patterns we aim to describe. We introduce the vector field $\boldsymbol{r}$, which denotes the smooth variation of vertex positions

$$\boldsymbol{r}_i \approx \boldsymbol{R}_{ij} + \boldsymbol{r}_{ij}^a \nabla_a \boldsymbol{r} \tag{5.2}$$

where $\boldsymbol{R}_{ij} \equiv .5\left[\boldsymbol{r}_i + \boldsymbol{r}_j\right]$ and $a, b \in [1, 2]$ index spatial dimensions. Einstein summation convention is assumed unless otherwise noted. Eq. 5.2 immediately implies the physical length of edge i, j is given by

$$r_{ij} \approx u_{ab}(\boldsymbol{R}_{ij})\, r_{ij} \hat{\boldsymbol{r}}_{ij}^a \hat{\boldsymbol{r}}_{ij}^b \tag{5.3}$$

$u_{ab} \equiv .5\left[\nabla_a \boldsymbol{r}_b + \nabla_b \boldsymbol{r}_a\right]$ denotes the continuum strain tensor which measures the local deformation of cells relative to a uniform embedding. Lastly, we introduce the symmetric, positive-definite tensor field s_{ab} that captures the intrinsic cytoskeletal geometry

$$\ell_{ij} \approx s_{ab}(\boldsymbol{R}_{ij})\, r_{ij} \hat{\boldsymbol{r}}_{ij}^a \hat{\boldsymbol{r}}_{ij}^b \tag{5.4}$$

Substituting all results into the original energy functional, we arrive at

$$E \approx \frac{K}{2} \int d^2\boldsymbol{x} \; [u_{ab} - s_{ab}] \left(\sum_{<i,j>} \delta^2(\boldsymbol{x} - \boldsymbol{R}_{ij}) r_{ij}^2 \hat{\boldsymbol{r}}_{ij}^a \hat{\boldsymbol{r}}_{ij}^b \hat{\boldsymbol{r}}_{ij}^c \hat{\boldsymbol{r}}_{ij}^d \right) [u_{cd} - s_{cd}] \tag{5.5}$$

The quantity in the parentheses is recognized as the dimensionless elasticity tensor that is dependent upon the quenched disorder associated with the local morphology of the cellular lattice. As we are only interested in the *typical* large-scale behavior of morphogenesis, we must compute the *average* of this energy over geometric disorder within the mesoscopic patch. Motivated by the approximate hexagonal nature of apical cell areas observed, we assume each patch is statistically homogeneous and isotropic [96], giving us the effective continuum energy

$$E = \frac{1}{2} \int d^2\boldsymbol{x} \; [u_{ab} - s_{ab}] \left(\lambda(\boldsymbol{x}) \delta^{ab} \delta^{cd} + \mu(\boldsymbol{x}) \delta^{ac} \delta^{bd} \right) [u_{cd} - s_{cd}] \tag{5.6}$$

The final result is unsurprising - in the continuum limit we recover the picture of epithelial tissue mechanics as a pre-strained elastic medium that we originally started with - but the above derivation allows us to interpret the mesoscopic parameters in the context of the original network variables. Specifically, the pre-stress tensor s_{ab} originates from the intrinsic geometry of the underlying cytoskeletal network - any deviation of the actual cell geometry, summarized by the strain tensor u_{ab}, from this signifies that myosin motors are actively stressing the underlying network. Furthermore, the effective constitutive relationship defined by $K^{abcd} = \lambda(\boldsymbol{x})\delta^{ab}\delta^{cd} + \mu(\boldsymbol{x})\delta^{ac}\delta^{bd}$ ultimately arises from the underlying cellular morphology within each patch. Here, we've only considered the simplified case in which all cellular patches are on average hexagonal. The overall scale is set by the stiffness of actin bundles.

Equation 5.6 is recognized as the linearization of the energy describing a non-euclidean plate, a material with no stress-less configuration in $\mathbb{R}^2$, in the limit of zero thickness [49, 155]. This class of models has had success modeling phenomena ranging from the shape of growing leaves[152], how a venus flytrap snaps [57], to the periodic wrinkles found in stretched plastic bags [156]. Non-euclidean plates and shells (thin material with finite curvature) are modeled using a material reference metric $\bar{g}$ which defines the stress-less conformation which arises from the pattern of differential growth [63]. In general, growth will lead to a metric with finite gauss curvature and thus there exists no planar embedding with zero stress - i.e. the ground state is frustrated [49].

Importantly, we have shown that in the continuum limit the ATN model recapitulates the general properties of non-euclidean plates, but generalizes the model insofar that the intrinsic metric of the material can change not only due to patterned growth, but also due to the differential flow of cells. In our present context, we imagine unbalanced myosin acting as a 'force' which contracts the intrinsic geometry of the material. For generality, we generalize Eq. 5.6 to describe epithelial morphogenesis on curved surfaces using the dictionary between non-euclidean shells and plates in the limit of zero thickness such that we can ignore bending [50]

$$E = \frac{1}{2} \int \sqrt{|g|} d^2\boldsymbol{x} \; [u_{ab} - s_{ab}] \left(\lambda g^{ab} g^{cd} + \mu g^{ac} g^{bd} \right) [u_{cd} - s_{cd}] \tag{5.7}$$

u_{ab} and s_{ab} are taken to be small perturbations of the conformational and intrinsic reference metrics relative to the shell's midsurface metric g_{ab}. For a plate ($g_{ab} = \delta_{ab}$) we recover the derived result Eq. 5.6. For the remainder of this section, we take the material to be homogeneous and thus λ, μ are scalars.

In analogy with vertex dynamics taken for the network model of Chapter 2 and 4, the equation of motion for cellular flow is assumed to be determined by relaxational dynamics of the above energy.

$$\nu \dot{u}^b = -\frac{\delta E_c}{\delta u^b} = \nabla_a \left[\lambda \left(\nabla^c u_c - s^c{}_c \right) g^{ab} + \mu \left(\frac{\nabla^a u^b + \nabla^b u^a}{2} - s^{ab} \right) \right] = \nabla_a \sigma^{ab} \tag{5.8}$$

∇_a denotes the covariant derivative along the a^{th} tangent vector belonging to the midsurface g_{ab}. The intrinsic metric s_{ab} is rank 2 symmetric tensor and thus can be decomposed into a 'flat' portion generated by the symmetrized gradient of vector field ψ_a and a 'curved' portion associated to a deviation from the intrinsic curvature of the midsurface manifold.

$$s_{ab} = \frac{1}{2} \left[\nabla_a \psi_b + \nabla_b \psi_a \right] + \nabla^*_a \nabla^*_b \varphi \tag{5.9}$$

We have defined the rotated gradient (or wedge product) $\nabla^*_a \equiv \varepsilon^b_a \nabla_b$, where ε^b_a is the Levi-Civita symbol, such that $\nabla^*_a g^{ab} \nabla_b = 0$. Cells will stop moving when stress is balanced, given by

$$\mu \left[\nabla^2 + \kappa \right] \left[u - \psi \right]^a + \lambda \nabla^a \nabla^b \left[u - \psi \right]_b = \lambda \nabla^a \nabla^2 \varphi \tag{5.10}$$

κ is defined as the Gaussian curvature of the midsurface manifold. In the limit of no bulk modulus ($\lambda = 0$), stresses are balanced when displacements u_a exactly equal the generating vector field ψ_a of the flat portion of the intrinsic metric s. The 'curvature' term leftover $\nabla^*_a \nabla^*_b \varphi$ is the residual stress that is unable to be balanced against deformations within the tangent plane; it is precisely the component which does not satisfy the St.

Venant compatibility condition [97]

$$W_{abcd} \equiv \nabla_c \nabla_d s_{ab} + \nabla_a \nabla_b s_{cd} - \nabla_b \nabla_c s_{ad} - \nabla_a \nabla_d s_{bc} = 0 \tag{5.11}$$

Eq. 5.11 is recognized as the linearization of the constraint that tensor s_{ab} has zero Riemann curvature and thus is immersible in the embedding space defined by g_{ab} [31]. The intrinsic metric s will evolve due to the active contraction of myosin on actin filaments, which we assume to take the simple form

$$\tau_\ell^{-1} \dot{s}_{ab} = \sigma_{ab} - m_{ab} \tag{5.12}$$

m_{ab} is defined as the mesoscopic myosin tensor and asymptotically determines the stress, the continuum analog of the stall condition explored in the network model in Chapter 2 and 4. Eqs. 5.8, 5.12 can be integrated to obtain a prediction of the flow field from a given time-course of mesoscopic myosin. Due to the time-scale separation between the equilibration of mechanics within the actin cytoskeleton and the global morphogenetic flow, it is reasonable to consider this problem in the adiabatic regime, i.e. the tissue instantaneously satisfies force balance $\nabla_a \sigma^{ab} = 0$ throughout the course of the cellular flow. Further assuming $|\sigma_a^a - m_a^a| \ll \frac{\mu}{\lambda}$, we arrive at the simple relationship between cell flow $\dot{u}_a$ and unbalanced myosin $\nabla_b m^{ab}$

$$\left[\nabla^2 + \kappa\right] \dot{u}^a + \frac{\lambda}{\mu} \nabla^a \left[\nabla_b \dot{u}^b\right] \approx -\nabla_b m^{ab} \tag{5.13}$$

Thus in the adiabatic limit and independent of myosin dynamics, we predict that the continuum active tension network should behave as a viscous, compressible fluid driven by actomyosin activity, phenomenologically consistent with continuum ‘Active Matter’ models [106]. As done in Chapter 4, one can immediately utilize this formula to analyze the mesoscopic effects of particular forms of mechanical feedback on myosin kinetics and thus closing the dynamical system of equations. However, we first must verify that Eq. 5.13 is an accurate starting point for tissue morphogenesis.

5.2 Measurement of morphogenetic flow and mesoscopic myosin during early Drosophila embryogenesis

In this section, we design a systematic, automated pipeline to detect coarse-grained morphogenetic flow and global myosin distributions to experimentally test eqn. 5.13 in living systems. Specifically, given a measured mesoscopic myosin tensor m_{ab}, eqn. 5.13 can be solved to obtain a prediction for the cellular flow field that can be tested against the empirically measured velocity field. This work was done in collaboration with Sebastian J. Streichan, who carried out light-sheet microscopy measurements of fluorescently labeled nuclei and myosin to measure morphogenetic flow and and the mesoscopic myosin tensor respectively. All data presented below analyzes the first few hours of Drosophila embryogenesis but we fully expect the pipeline to be applicable generally. Furthermore, the following discussion will focus on morphogenesis in the apical plane of the embryo. ImSaNe was used for dimensional reduction of the imaging data [73].

We measure the flow field using the particle image velocimetry (PIV) method, that identifies local displacements between two time points [1]. Specifically, a grid is defined over each image. The displacement that maximizes the correlation between elements of the grid within two subsequent time points is used as a proxy for the velocity. We implemented the phase correlation variant that leverages favorable execution times of fast fourier transforms, to estimate local flow within each region of interest [94]. This method is greatly preferred over tracking cells - a monumental task that requires accurate segmentation throughout the entirety of the morphogenetic movement.

We find that tissue remodeling during Drosophila gastrulation is characterized by three simple flow field configurations (Fig 5.1c-e). The earliest flows start well before the ventral furrow (VF) forms, and are characterized by a dorsal sink and ventral source (Fig 5.1c). In contrast to the VF, no cells are internalized during this flow, but rather cells reduce cross section on the dorsal side to account for the finite divergence. As the VF forms, source and sink swap sides and a large group of cells internalize on the ventral side, as mesoderm precursors leave the surface of the blastoderm (Fig 5.1d). During germband extension (GBE), the flow pattern exhibits two saddles arranged on the dorsal and ventral sides as well as four vortices, two in the posterior and two in the anterior end (Fig 5.1e). The hyperbolic flow results in the convergent extension of the lateral ectoderm.

Anisotropic distribution of myosin is often characterized by homogeneously increased accumulation to cell edges of particular orientation, while it remains homogeneously low and comparable to background on other edges [186, 16, 14]. Note that typically the number of edges at low and high signal accumulation are roughly equal. Available methods

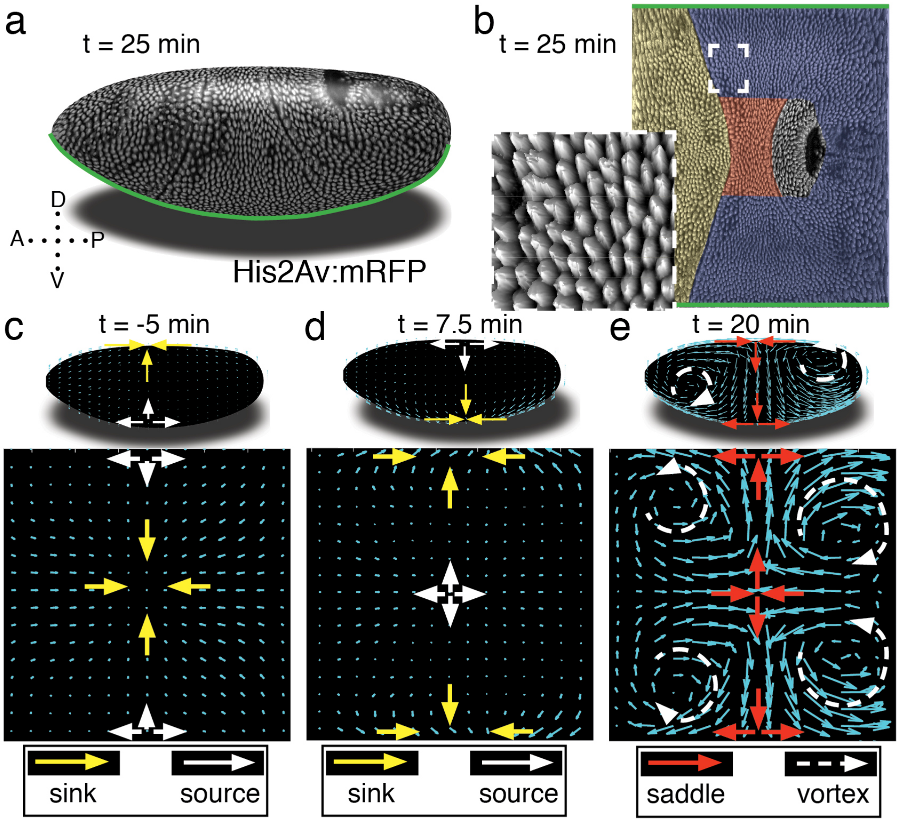

Figure 5.1: Drosophila melanogaster embryos during gastrulation, captured by three simple flow fields. (a) Example of $2D$ data. Anterior is to the left, dorsal up. Time is chosen such that 0 min coincides with the occurrence of the cephalic furrow (CF). (b) Thin sub-apical layer through embryo shown in (a), with prospective head, germband and amnioserosa color-coded. Dorsal is in the center and ventral is on top and bottom of image. Inset shows zoom into germband. (c-e) Flow field on 2D projections for representative time points of the pre-Ventral Furrow (pre-VF) phase (c), Ventral Furrow (VF) phase (d), and germband phase (GBE) (e). Cyan arrows indicate tissue flow field. Bold arrows indicate flow field topology.

to quantify cortical anisotropy mostly operate at the single cell level and construct a nematic tensor by integrating signal intensities along cell outlines [2]. At the organismal scale membrane segmentation is costly, and for polarized markers low signal to noise on a significant number of edges often results in difficulties to close the cell circumference. We overcome the need for fiduciary markers that increase experiment complexity, by shifting perspective to cell edges and designing a robust and rapid segmentation free anisotropy detection algorithm based upon the Radon Transform, an integral transform that takes a function defined in the plane to a function defined on the space of line [139]. Specifically, given an image $I(\boldsymbol{x})$, the radon transform $\mathcal{R}_I(\alpha, s)$ is defined

$$\mathcal{R}_I(\alpha, s) \equiv \int dz I(z\sin(\alpha) + s\cos(\alpha), -z\cos(\alpha) + s\sin(\alpha)) \tag{5.14}$$

Thus, the radon transform maps an image into a conjugate image containing information of all possible line integrals. We leverage this to detect enriched acto-myosin cytoskeletal bundles within an image. Since the radon transform is linear, it follows that for any image that is the linear superposition of linear signals, the radon transform is the linear superposition of the radon transform of each linear signal. For example, if an image consisted of 2 linear signals (for example a four fold vertex), the resulting radon transform is the sum of the radon transform of each linear signal, with peak levels at orientation and signed distance of each linear signal. An example is shown in Fig. 5.2a. As such, linear signals are mapped to peaks in the radon transform that reflect the total intensity along the length of the line. Knowing the location of peaks in the radon transformed space allows us to reconstruct the position and orientation of each linear signal in the image.

This simplifies the task of identifying lines to the detection of peaks which are significantly easier to detect owing to the fact that they are zero-dimensional! Furthermore, due to the integral nature of the the radon transform, the resultant signal will be less susceptible to noise in the original data. An example of the automated segmentation of myosin is given in Fig 5.2

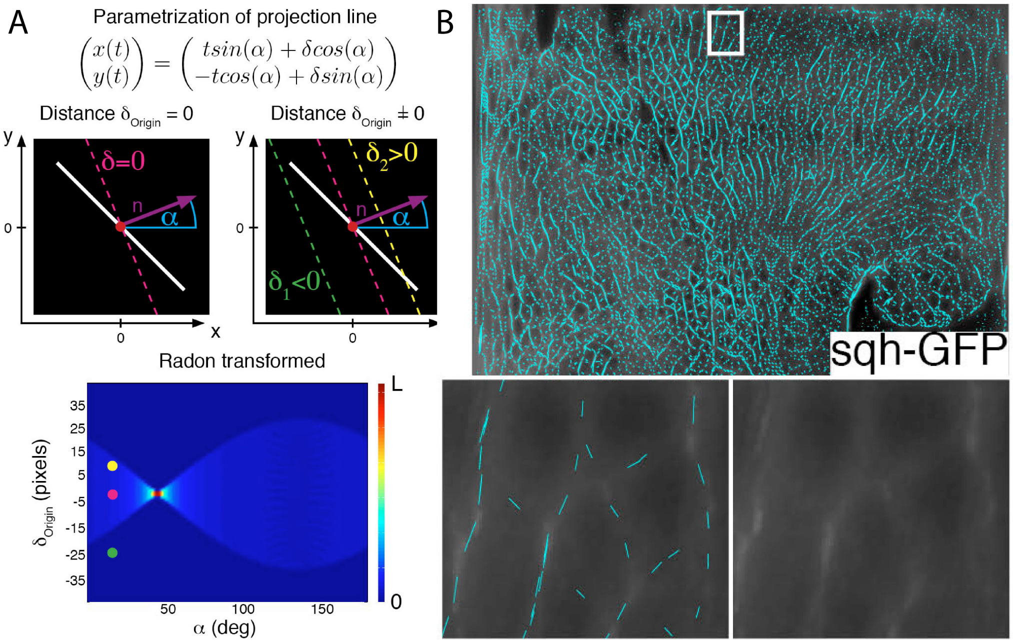

Figure 5.2: Measuring myosin in an automated manner. (a) A cartoon example of an image with its radon transform displayed below. Each colored line shown in the image is mapped to an equivalently colored point in the radon plane. (b) Representative example of edges identified with our anisotropy detection algorithm, and a magnification in a region of interest showing result in comparison with underlying raw data, florescently labeled regulatory chain of myosin motors (sqh-GFP)

The mesoscopic myosin tensor can be immediately estimated using the myosin nematics measured by the radon transform along the similar spirit as Eq 5.4. Defining m_n,$\hat{\boldsymbol{r}}_n$, and $\boldsymbol{R}_n$ to be the myosin density, orientation, and position of the n^{th} acto-myosin bundle detected by our automated segmentation respectively, the mesoscopic myosin tensor is given by

$$m^{ab}(\boldsymbol{x}) \equiv \int \sqrt{|g|} d^2\boldsymbol{x'} K(|\boldsymbol{x} - \boldsymbol{x}'|, \sigma) \left[\sum_n m_n \hat{\boldsymbol{r}}_n^a \hat{\boldsymbol{r}}_n^b \delta^2(\boldsymbol{x'} - \boldsymbol{R}_n) \right] \tag{5.15}$$

where $K(|\boldsymbol{x} - \boldsymbol{x}'|, \sigma)$ denotes the kernel used to coarse-grain (over length-scale σ) the estimated microscopic myosin configuration obtained from the radon transform. σ was chosen to be on the scale of ~ 15 cells.

Using the above pipeline, global reconfigurations of mesoscopic myosin pools were found to be a hallmark for transitions in flow field configuration during Drosophila gastrulation,; each of the three flow field geometries previously discussed was found to be accompanied by a typical spatial myosin configuration. The pre-VF flow associates with basal myosin that exhibits a pronounced Dorso Ventral (DV) symmetry breaking, with high levels of myosin on the dorsal and low levels on the ventral side (Fig 5.3a), while the apical pool appears homogeneous across the surface (Fig 5.3d). The basal pool remains asymmetric during VF flow (Fig 5.3b), but the apical pool now also displays broken DV symmetry in the reversed orientation (Fig 5.3e). The asymmetry on the apical surface becomes further pronounced in the GBE-phase (Fig 5.3c,f).

5.3 Numerical implementation of model.

To obtain a prediction for the morphogenetic flow given a myosin tensor requires solving Eq. 5.13 numerically. Implementation of the PDE was done using Finite Element Methods (FEM) implemented within the FELICITY toolbox for MATLAB [175]. Finite

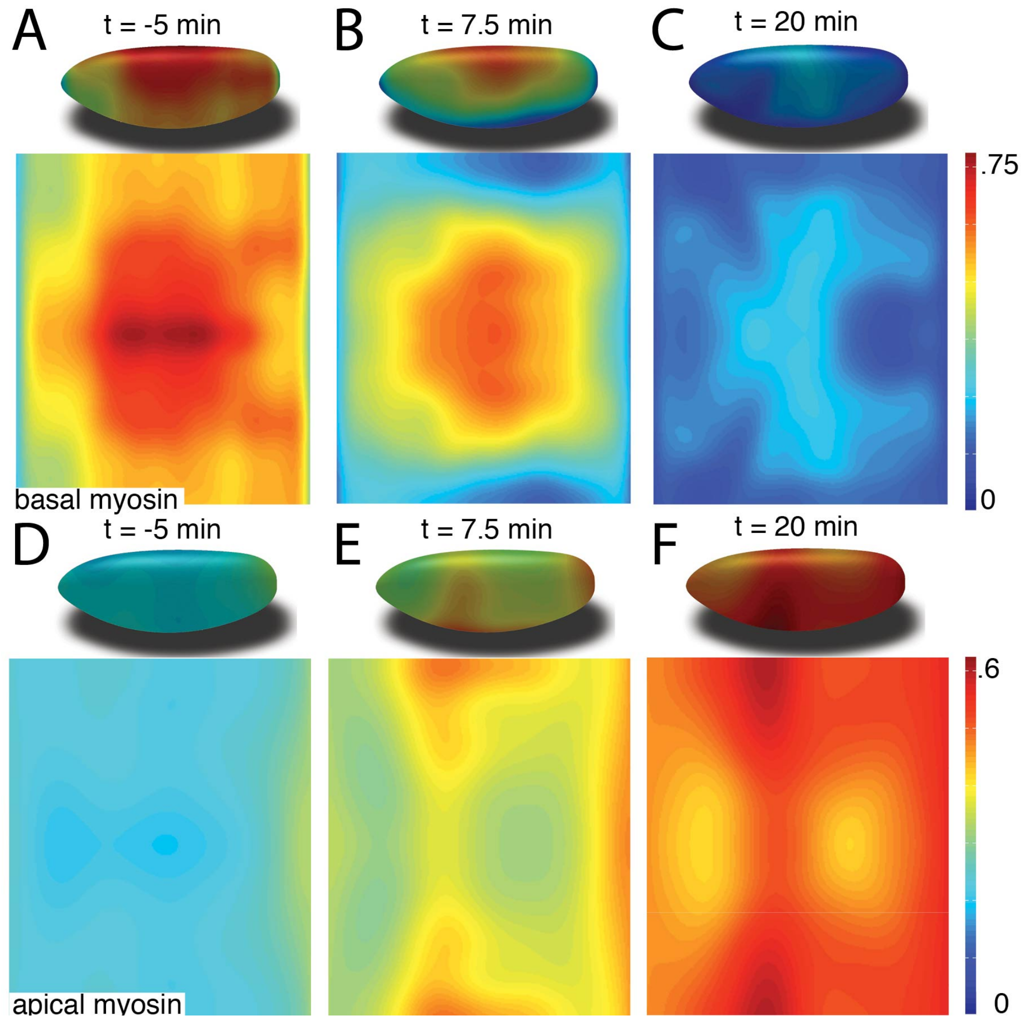

Figure 5.3: Tissue deformations of Drosophila melanogaster embryos during gastrulation, captured by three simple myosin configurations. Normalized myosin distribution on basal cell surface corresponding to times shown in (a-c). Color code from lowest 0 to highest 1. Similarly, (d-f) displays the pool of myosin on the apical cell surface

Element methods require defining a static triangular mesh representing the ‘canonical embryo mid-surface. The apical surface of the embryo was estimated from point cloud data using ImSaNe [73] and MeshLab [32].

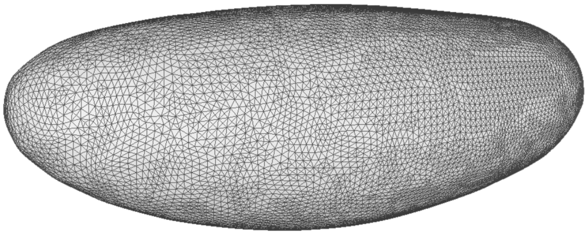

Figure 5.4: The ‘embryo’ mesh representing the apical surface. Eqn. 5.13 was inverted using FEM defined on the mesh.

The automated pipeline above measures the myosin tensor by course graining nematics obtained from the Radon transform done on the cylindrical projection of the embryo’s apical surface [73]. However FEM methods require all fields to be parameterized within the 3D embedding space of the mesh. Thus, the 2D myosin tensor was embedded using the metric between projections and the detected apical surface computed by ImSaNe [73]. The divergence of the myosin tensor was computed by interpolating the gradient of each cartesian component of the tensor onto flat triangular faces of the mesh, shown in Fig. 5.4, resulting in a third order tensor in three dimensions. The divergence is simply the partial trace of this tensor over directions within the tangent plane of the face. This operation was repeated independently for the apical and basal pool.

5.4 Continuum model predicts global flow during embryogenesis of Drosophila

Having formulated the measurement pipeline of both mesoscopic myosin and global morphogenetic flow, we can quantitatively test the presented model on intermediate timescales. Our model has only one global parameter to be fit by the data: the ratio of bulk and shear moduli. Predictions for the flow field obtained via solving eq. 5.13 are subject to an overall scale factor, related to the unknown coefficient of viscosity, undetermined by the model. To compare ensemble averaged flow field measurement $\boldsymbol{v}(t)$ to model predictions $\dot{\boldsymbol{u}}(t)$ in a quantitative fashion, we define a global measure for the difference between both vector fields that is insensitive to such a scale factor. In what follows, $\langle \boldsymbol{v}^2 \rangle$ denotes the average square norm of the velocity over the entire embryo. Fitting the overall scale between both fields by minimizing the difference, the residual field is given by

$$R = \frac{\langle \boldsymbol{u} \rangle^2 \boldsymbol{v}^2 - 2\langle \boldsymbol{u} \rangle \langle \boldsymbol{v} \rangle \left(\boldsymbol{v} \cdot \boldsymbol{u} \right)}{2\langle \boldsymbol{u} \rangle^2 \langle \boldsymbol{v} \rangle^2} \tag{5.16}$$

$\langle R \rangle \in [0, 1]$ with zero and one indicating perfect or anti-correlation respectively. The spatial field provides a density map of errors in the prediction. The model achieves about $\langle R \rangle \sim 90\%$ accurate description of the flow pattern before and after VF invagination (see Fig 5.5b). The main discrepancy of model predictions for pre-VF flow (see Fig 5.5c) is a displacement of sink and source positions along the AP axis by less than 30 μm. Prediction of GBE flow essentially agrees with measurements across the entire embryo, with the exception of a domain close to the vortices on the posterior end, due to a mismatch of

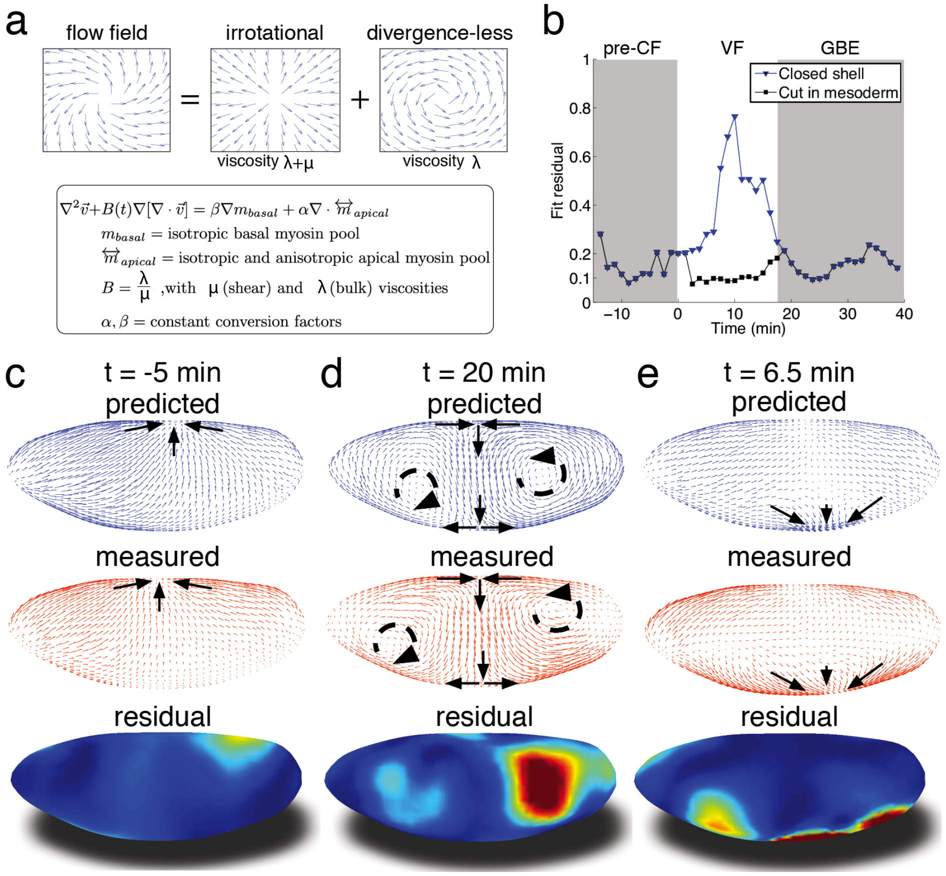

Figure 5.5: Biophysical model quantitatively predicts tissue flow based on quantitative measurements of myosin distribution. (a) Proposed mathematical description of the flow parameterizes complex mechanics of cytoskeleton in terms of two effective viscosities thatcontrols the circulatory and irrotational component of the flow. (b) Fit residual, comparing predicted flow field with measured flow field normalized for magnitude as a function of time. (c-e) From top to bottom spatial distribution of predicted (blue), measured (red) flow field, and residual (blue best agreement, red worst, on a scale from 0 to 1) for select time points.

fixed-point location (Fig 5.5d). Remarkably our model is even able to correctly predict subtle differences between anterior and posterior fixed points along the DV axis (Fig 5.5d). Measured flow is first dominated by sources and sinks that disappear later during GBE, suggesting that before and during VF invagination cells are less resistant to surface area compression than during GBE. Indeed, quantitative comparison with an independently measured flow field (Fig 5.1c-e) shows that the λ/μ ratio increases dramatically at the start of GBE phase, resulting in effective incompressibility of apical surface of cells.

Poor agreement during VF formation is due to a significant fraction of cells internalizing and thus leaving the surface. To account for this effect, we extend the model to allow a cut in the lattice along ventral midline with an imposed in-plane boundary force (perpendicular to the cut) representing the pulling effect of the VF. This relatively simple extension recovers 90% accuracy (Fig 5.5be), illustrating how regional inhomogeneity associated with particular morphogenetic events could be quantitatively captured by suitable generalizations.

To assay the robustness of the fit obtained in WT embryos, we examined morphogenetic flows in mutant embryos in which both the overall morphology and the spatial distribution of myosin is significantly altered. Tissue tectonics has shown that *twist* (*twi*) embryos, which lack the formation of a ventral furrow, exhibit slower strain rates as compared to WT [15]. The cause of this remained a subject of debate. We have quantified the flow field and myosin activity patterns in *twi* mutants, and find that our model is able to accurately predict the flow profiles (Fig 5.6a). During early flow phases corre-

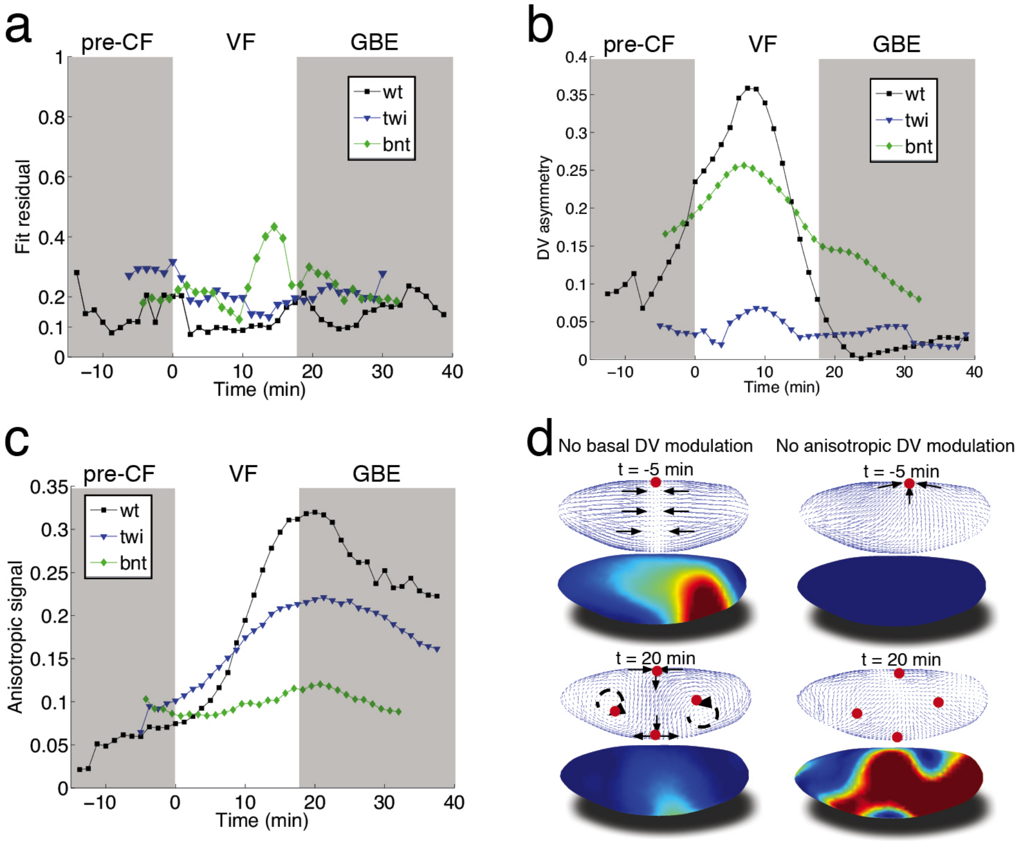

Figure 5.6: Mutant analysis reveals global modifications of myosin dynamics. (a) Fit residual as in fig. 3b, for twi, and bcd nos tsl mutants. WT is shown as reference. (b) Amplitude of basal myosin pool along DV axis for WT and mutants in (a). (c) Polarized apical myosin in mutants shown in (a) as function of time. (d) Theoretical comparison of DV constant basal pool (i.e. no gradient in DV direction) (left column), or DV constant anisotropic apical pool (i.e. no gradient in DV direction) (right column) with predicted flow based on full myosin tensor (compare to fig 3c,d respectively). Black arrows indicate flow field topology, and red dots the fixed point from prediction based off of full myosin tensor

sponding to times of pre-VF flow in WT DV asymmetry of the basal myosin pool is strongly reduced in comparison to WT, as is tissue movement towards the dorsal pole (Fig 5.6b). Moreover, anisotropy of the apical myosin pool increases at a slower rate as compared to WT. As previously reported for strain rates, this is most pronounced for the first 20 min (Fig 5.6c).

In mutant embryos lacking all AP patterning (*bicoid nanos torsolike* or *bnt*), the early basal DV asymmetry is similar to WT, with only slightly reduced myosin asymmetries and dorsal movement (Fig 5.6b). At later stages, however, anisotropy of the apical myosin pool remains low and comparable to pre-VF WT levels. This result is expected given the uniform expression of pair-rule genes in a *bnt* genetic background (Fig 5.6c). Consistent with these myosin distributions, we see the early dorsal flow associated with basal myosin asymmetry but a failure to produce the complex later flow patterns with their characteristic saddles and vortices. On a quantitative level our models predictive power for AP patterning deficient *bnt* mutant embryos is comparable to *WT* and *twi* mutants (Fig 5.6a).

5.5 Comparison of global myosin patterns and inferred stress during Drosophila gastrulation

As seen above, the mesoscopic pattern of apical myosin II motors, summarized as a 2D tensor, is sufficient to explain the coarse-grained morphogenetic flow of cells directly preceding and concurrent with GBE over the entire embryo. Fig. 5.7a shows the anisotropic component of the myosin tensor measured during GBE, exhibiting coarse-grained features of the stress cables discussed in Chapter 4. However, can we determine which regions are the putative drivers of the observed flow? Recall that myosin contractility is modeled as driving the morphological flow via eq. 5.12 and thus we expect regions where the myosin tensor diverges from the elastic stress tensor to be generating cell movement.

We can test this hypothesis using the local "Mechanical Inference" algorithm outlined in detail in Chapter 3. As myosin line density was found to correlate strongly but not perfectly with inferred tension in the lateral ectoderm, we expect this correspondence to hold at the mesoscopic scale for the embryo during the same time of development. Alas, while the formulated stress inference provides a high-throughput assay of sub-cellular mechanics, it is restricted to inference of mechanics balancing a 2D planar cell array. As such, we broadly introduce a generalization the stress inference to curved two-dimensional surfaces. Interested readers are directed to the Appendix for further description.

As previously noted in Chapter 3, the proposed mechanical inference is over-determined and thus entirely local; we can utilize the local algorithm infer mechanics of disparate subregions within the embryo despite no knowledge of the regions' boundary conditions. Therefore, provided the cell size is smaller than the surface's curvature, the tissue's surface (obtained using ImSaNe [73]) can be partitioned into overlapping, approximately flat patches. Once approximated as a planar array, each cellular region can be subsequently fit to a weighted dual triangulation. The balanced stress within each patch can only

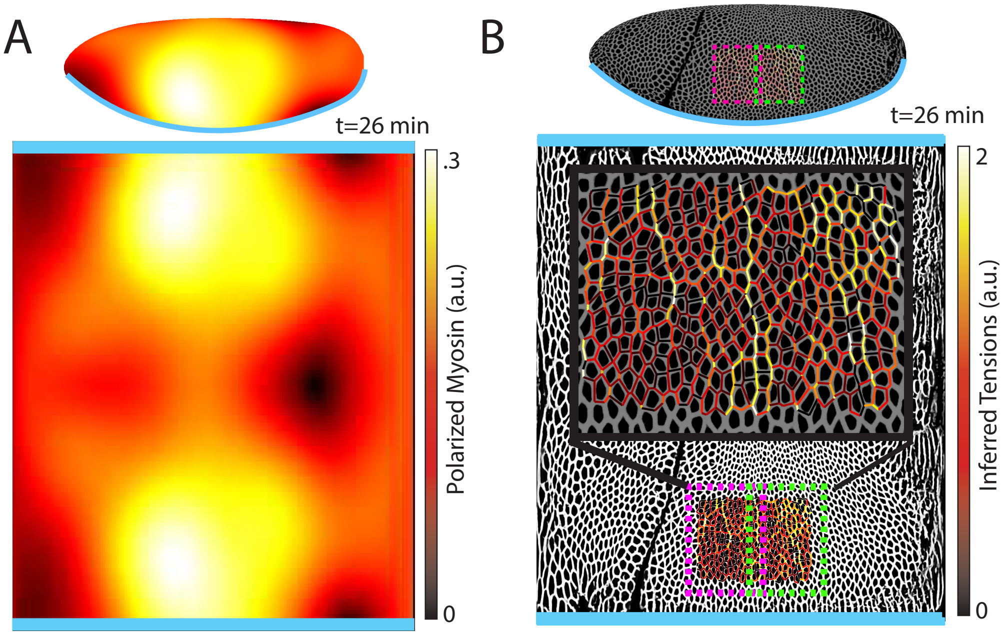

Figure 5.7: (a) The mesoscopic anisotropy of myosin (measured along the DV axis) shown on the embryo, as well as unwrapped in the plane. Anisotropy is largest in the lateral region, thought to drive GBE. (b) An example of the stress inference, plotted over the estimated geometry, done on embryo-scale data. An overlapping grid is first defined, shown in the figure within the green and pink dashed boxes, where the force inference is ran independently. The overlapping regions are used to 'stitch' together the stress tensor. Note the inferred stress cables shown in the region that is expected to exhibit high anisotropy. For quantitative comparison see next figure.

be determined up to an unknown overall scale. As such, the relative scale between all sub-regions is fit by minimizing the difference of edge tensions within overlapping regions. Full details of the inversion algorithm can be found in the Appendix. An example of two stitched overlapping patches, with the resultant stress field exhibiting the expected stress anisotropy along the DV axis, is shown in Fig. 5.7b.

Given the inferred mechanical parameters $\{T_{ij}, p_\alpha\}$ the mesoscopic stress is obtained by coarse-graining the microscopic stress tensor

$$\sigma^{ab}(\boldsymbol{r}) = \begin{cases} p_\alpha g^{ab} & \text{if } \boldsymbol{r} \in \mathcal{A}_\alpha \\ T_{\alpha\beta}\,\hat{\boldsymbol{\tau}}^a_{\alpha\beta}\hat{\boldsymbol{\tau}}^b_{\alpha\beta}\delta(|\boldsymbol{r} - \boldsymbol{\rho}_{\alpha\beta}| - R_{\alpha\beta}) & \text{if } \boldsymbol{r} \in \boldsymbol{r}_{\alpha\beta} \end{cases} \tag{5.17}$$

$\hat{\boldsymbol{\tau}}_{\alpha\beta}$ is taken to be the unit tangent vector along circular edge α, β. By construction, the stress is balanced everywhere - i.e. has no divergence. The explicit construction of the stress tensor along with the coarse-graining procedure can be found in th appendix.

Patterns of myosin and inferred stress were compared along their trace and traceless components. The 2x2 symmetric traceless tensors were compared by computing the magnitude of the difference, defined by

$$\Delta = |m - \lambda\sigma|/|m| \tag{5.18}$$

λ fixes the unknown global scale between inferred stress and measured myosin chosen to minimize the residual Δ. The traces of both tensor fields were compared using the Pearson correlation coefficient ρ over space. Fig. 5.8b shows the time-course of Δ and ρ over $\sim$50 minutes of Drosophila development during gastrulation. Overall, we find great global agreement between myosin and stress nematic tensors, preceding and concurrent with the fast phase of GBE ($\Delta \sim .15$). Conversely, the trace of both tensors disagree

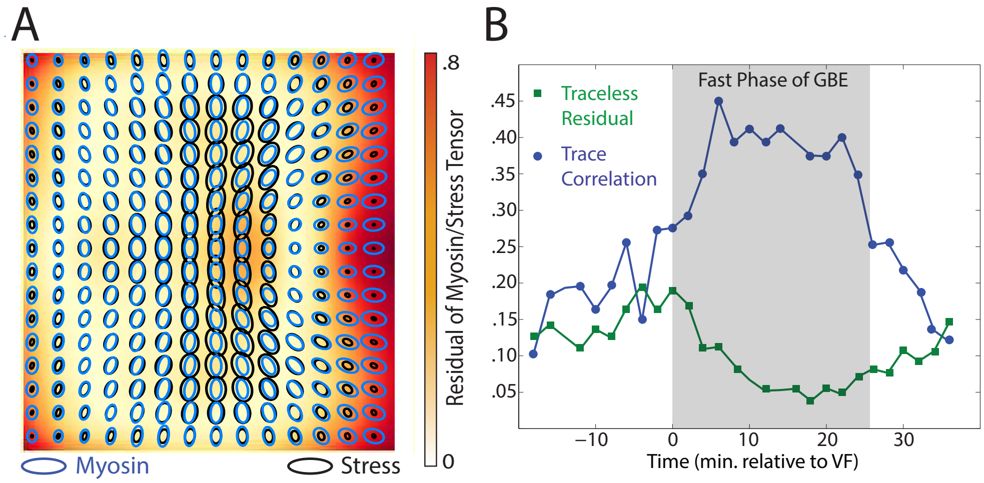

Figure 5.8: (a) A graphical comparison between the measured myosin and inferred stress tensors, each shown as ellipses with major axes pointing along the principal direction of stress. The scalar difference Δ, defined in eq. 5.18, between both tensors is plotted as a heatmap below. (b) The average distance between stress and myosin tensors as a function of time. As we can only infer the balanced stress tensor, we see the distance increase as germ band extension progresses.

in general, except during the fast phase of GBE, where we good correlation ($\rho \sim .5$), consistent with the local measurements in the lateral ectoderm shown above.

The disagreement is localized to well-defined regions during development. Preceding GBE, we predict an overall AP gradient in balanced stress that is not seen in the myosin pattern. Fig. 5.8a displays the comparison between myosin and stress 20 minutes after VF formation, showing excellent global agreement between the principal axes of myosin and stress, shown by the major axes of the plotted ellipses, however the amount of myosin is underestimated within the dorsal regions close to the posterior mid-gut and the lateral ectoderm, as shown by the respective elliptical areas. This measurement is consistent with previous studies that concluded both the invagination of the endoderm, which drives passive cell elongation, and active cell intercalations within the lateral ectoderm, both drive the morphological transitions during this time [91]. The result hints at the role that DV patterning plays in the convergent extension flow and suggests that the unbalanced myosin along the DV axis drives the observed morphological flow. We believe the ability to estimate global patterns of stress, on arbitrary surfaces, opens up a novel method in which one can find regions *driving* morphological changes.

5.6 Tissue mechanics model as a quantitative framework for the future

In addition to previously described accumulation of isotropic myosin in ventral regions, we observe a striking gradient of anisotropic apical myosin along the embryo's DV axis, reaching highest levels in lateral ectoderm and lowest levels in amnioserosa tissue at the dorsal pole. As noted, the global modulation of the myosin distribution is critical for the observed dynamics. This is further supported by comparing the measured myosin tensor with inferred stress. While local rate of cell intercalation is often interpreted in terms of local myosin distribution on cellular and sub-cellular scales, the continuum model shows that the local rate of strain is a result of the tissue-wide distribution of forces generated by the the divergence of the effective myosin tensor. The importance of spatial modulation (Fig 5.6d and Fig 5.8) suggests a novel role of the dorsal signaling pathway in the generation of the GBE flow.

Surprisingly, twi mutants exhibit a significantly reduced rate of increase as well as peak myosin anisotropy in the first 20 minutes of GBE flow (Fig 5.6c). The reduced intercalation and strain rates observed in these mutants has been previously reported, and interpreted in terms of possible generation of AP forces by the internalized VF (absent in twi mutants). Our model accounts for the reduced rate of strain in terms of the changes within the reduced level of myosin anisotropy, consistent with the local model proposed in Chapter 4. This however brings up the question of how elimination of *twi* expression in the ventral mesoderm affects myosin anisotropy in the lateral ectoderm. We suggest that this effect may be due to mechanical feedback on myosin recruitment proposed earlier, which relates the later to local rate of strain. Through this "dynamic recruitment effect, changes in the ventral region can affect myosin distribution and anisotropy in the lateral region by reducing the tensile stress along the DV axis in this region. In this way, local modification of the myosin pattern can produce not only a non-local perturbation of the flow, but also a non-local perturbation of myosin distribution.

Our observations show that morphogenetic flow is a global response to local forcing within the cytoskeleton, which arises from the spatial modulation of myosin density and anisotropy. The latter is derived from the spatial patterns of developmental transcription factors, but we suggest may also involve mechanical feedback affecting recruitment of myosin. The coarse-grained ATN model, coupled with the quantitative approach outlined in this Chapter, provides a framework for integrating the effect of local cell behaviors of disparate tissues within a singular description of the global morphogenetic flow.

Evidence for the model's validity was presented only for intermediate time-scales and thus we can only conservatively conclude that cells during early Drosophila embryogenesis, behave collectively as a viscous, compressible fluid. While circumstantial evidence in twi mutants point to the existence of the hypothesized dynamic recruitment of myosin in response to unbalanced strains, this needs to be quantitatively checked in a similar manner as presented in this Chapter. In short, the next logical step to the presented analysis is to no longer take myosin to be an input to the theory, but rather as a predictable output along with the morphological flow field. A successful theory in this regard would be tantamount to discovering the equation of motion governing the global dynamics of the observed myosin distribution as a function of tissue stress, morphogen patterns, and current myosin and would be a huge step towards understanding the patterns governing morphogenesis.

All empirical analyses were done using Eq. 5.13, which we recognized to be a non-euclidean shell of zero thickness with intrinsic metric driven explicitly by contractile myosin. An important generalization of the simple model presented in this Chapter would be to consider an active shell of finite thickness h, which would add a bending term of order h^2 to Eq. 5.7. The tissue would thus interpolate between the membrane limit where planar flow is entirely driven by myosin imbalances explored here and out-of-plane bending induced by contractility depending on the epithelial layer's thickness. Importantly, this would connect three dimensional shape to planar distributions of myosin.

Chapter 6

Future outlook: Tissue mechanics and cell fate

Pattern formation is the central feature of developmental biology. The formation of an organism's shape synthesizes many patterned cellular processes including cell growth, proliferation, death, and collective cellular rearrangements. In this dissertation, we outlined a minimal model of cell biology that directly connects the expression levels of cytoskeletal proteins to tissue-scale mechanics. This allowed us to quantitatively explore mesoscopic consequences of different regulatory architectures. When feasible, we statistically validated predictions from our model against experimental live-imaging data.

In Chapter 2, we observed that by considering known mechanosensitive myosin II contractility, cells within the resulting tension network exhibit constrained geometries and floppy geometric modes. Both predictions were strikingly confirmed at the presumptive mesoderm of *Drosophila melanogaster* during formation of the ventral furrow. Chapter 4 extended our original minimal model and demonstrated that both kinetic bistability between cortical tension and myosin, and traction-dependent degradation of cadherin molecules were sufficient to describe the morphological dynamics observed during germ band extension of the lateral ectoderm. Beyond qualitative dynamical agreement with in-vivo data, correlation-based analyses were used to support the posited kinetic equations. The model furnished several additional quantitative predictions that should be possible to test experimentally. Lastly, Chapter 5 coarse-grained the cellular model showing that global morphogenetic flows should behave as an effective viscous, compressible fluid driven by the global distribution of myosin II motors. This simple model was able to explain 90% of the observed cell flow in three distinct genotypes during the first few hours of embryogenesis of *Drosophila melanogaster*.

The work presented within this dissertation thus relates the spatial distribution of cytoskeletal expression to the resultant morphogenetic flow, serving as a predictive dictionary between microscopic phenomenology and tissue-scale behavior. But what controls the underlying pattern of genetic expression itself? There has been little pattern formation considered within the presented work; cell fate was treated as an input rather than a dynamical variable itself. Chapter 2 demonstrated that the observed medial acto-myosin pulses drove the system along the manifold of zero states. However, it is known that the existence of pulses and the subsequent stabilization of cell perimeter are dependent upon expression of genes *twist* and *snail*. In our simulation, we simply assumed the pattern of pulses was consistent with that observed in-vivo. Similarly, the collective tissue transition from a hexagonal cell packing to the rectangular geometry induced by stress cables observed during GBE, and recapitulated by the model introduced in Chapter 4, is dependent upon patterned myosin fluctuations that drive coherent cable formation running along the DV axis. Again, we had to introduce anisotropy into our model to simulate the effects of patterned cellular states. Lastly, in Chapter 5 we were able to predict morphogenetic flow conditioned on having measured the mesoscopic myosin tensor globally. We currently have nothing to say about how the pattern of myosin is initialized and how it evolves throughout the course of morphogenesis. Taken together, the work presented in this dissertation will amplify an existing pattern and translate it into observable cellular morphology, but it does not exhibit spontaneous pattern formation.

We believe the next logical step is to understand the interplay between cellular patterning and the mechanics of morphogenesis. Cell-fate specification and rearrangements within the underlying epithelial tissue are known to occur simultaneously in many developing systems. Cell intercalation, lateral inhibition (cell-cell signaling that suppresses induction of your neighbors into a new cell state if the cell in question has already been induced), and patterned cell death have all been shown to contribute to the highly regular pattern of mammalian retinal ganglion cells [153], ommatidial cells within the Drosophila compound eye [182], and the hair cells of the basilar chick papilla [62]. Furthermore, it has become evident that mechanics plays a central role in the regulation of fundamental cell biological processes such as growth and cell identity [159, 133, 115]. Investigation is further warranted on strictly theoretical grounds; it is reasonable to assume that interesting new physics will emerge when considering reaction-diffusion equations on an active substrate that moves according to the supported chemical reactions.

The duality between equilibrium cellular networks and a weighted triangulation, formulated in Chapter 3, should immediately be valuable in approaching this topic at the cellular-scale. We demonstrated that any two-dimensional network of cortical tensions supported by heterogeneous isotropic cellular stresses is equivalently described by a triangulation equipped with a point-wise metric. Any vertex model in equilibrium is thus described by our generalized description. Importantly, the duality allows one to forget postulated constitutive relationships of cellular elements and adopt the universal language of geometry. We imagine morphogenesis as the process of evolving a triangulation and its metric; cell geometry merely comes along for the ride as its dual. Our description recasts all adiabatic morphological dynamics in cell-specific equations. Provided there exists a time-scale separation between morphogenetic movements and mechanical relaxation, the interplay between the patterning of molecules $\boldsymbol{g}_\alpha$ and apical mechanics will generically be contained in equations of the form

$$\frac{d}{dt}\begin{pmatrix}\boldsymbol{q}_\alpha\\ \Theta_\alpha\\ p_\alpha\\ \boldsymbol{g}_\alpha\end{pmatrix} = \mathcal{M}_{\alpha\beta}\left[\boldsymbol{q}, p, \Theta, \boldsymbol{g}\right]\begin{pmatrix}\boldsymbol{q}_\beta\\ \Theta_\beta\\ p_\beta\\ \boldsymbol{g}_\beta\end{pmatrix} \tag{6.1}$$

To conclude, let us make the discussion concrete and consider the developing chick cochlea. In the adult avian auditory organ, it is known that hair cells, the mechanotransductive structures that sense sound waves, form a highly regular mosaic pattern in

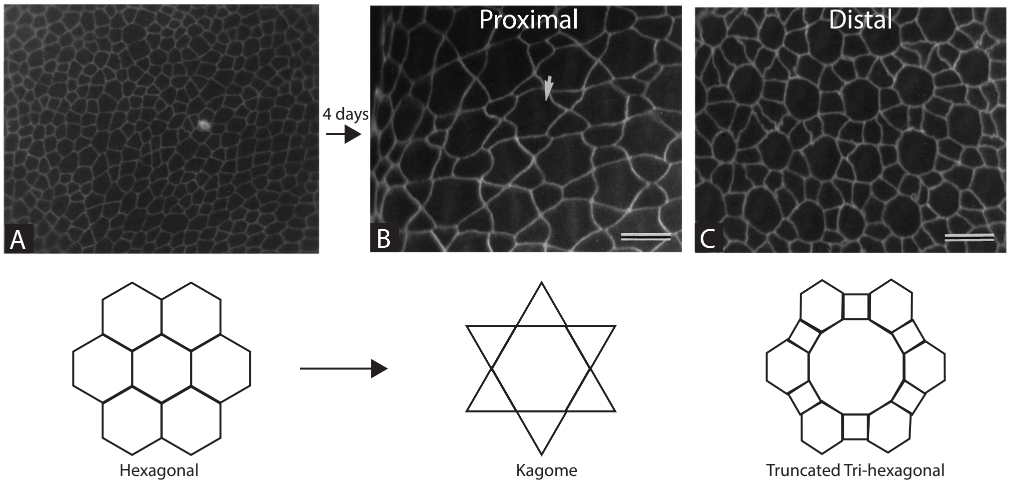

Figure 6.1: Tissue morphology starts as a weakly disordered hexagonal array until embryonic day 6 during development of the chick cochlea. Afterwards, it exhibits a dramatic morphological transition towards Kagome-like lattices at the proximal region that smoothly varies into a truncated tri-hexagonal array at the distal tip.

which each hair cell is contacted by six support cells and each support cell touches three hair cells [37]. Hair-cell specification arises on a hexagonal array as a direct consequence of lateral inhibition in which cells that adopt the hair-cell fate suppress the subsequent adoption of hair-cell state of its neighbors. In analogy to spin systems within physics, lateral inhibition can be thought of as an antiferromagnetic interaction between two-state patterning molecules of nearest-neighbor cells, and thus is phenomenologically captured with

$$\dot{A}_\alpha = \tau \sum_{\{\beta\}_\alpha} \left[r_{\alpha\beta} \frac{1}{1+A_\beta^n} \right] + \lambda \frac{\epsilon A_\alpha^{n'}}{1+\epsilon A_\alpha^{n'}} - A_\alpha \tag{6.2}$$

τ controls the strength of lateral inhibition and λ regulates the difference in expression of A between hair and support cells. As highlighted by Goodyear and Richardson [62], lateral inhibition in the cochlea does not proceed on a static substrate, but rather occurs concomitant with patterned cellular rearrangements and cell death. Strikingly, the initial hexagonal array of cells within the basilar papilla undergoes a dramatic geometric transition to different tissue morphologies that smoothly vary along the proximal-distal axis of the cochlea, shown in Fig. 6.1.

The apical geometries observed during this developmental process are all weakly disordered realizations of Archimedean tilings with trivalent vertices [67]. Remarkably, all such tilings are connected smoothly by an isogonal transformation and thus can be continuously transformed into each other, given a fixed triangulation $\boldsymbol{q}_\alpha$. The 'phase' diagram of morphology is depicted in Fig. 6.2

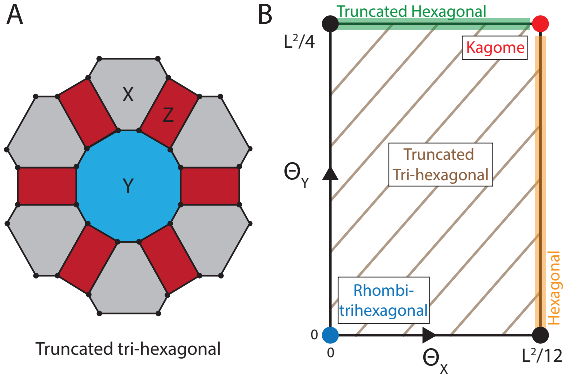

Figure 6.2: All Archimedean tilings, the class of tessellations observed during patterning of the chick cochlea, are related to each other by an isogonal transformation, parameterized by Θ_x and Θ_y defined on the truncated tri-hexagonal array defined in (a). The corresponding phase diagram of all Archimedean tilings is shown in (b) in terms of Θ_x and Θ_y.

Is there a generic relationship between the interplay of lateral inhibition given by Eq. 6.2 and the isogonal modes that move us within the morphospace defined by Fig. 6.2b that recapitulates the observed dynamics of patterning of both cell fate and tissue geometry within the chick cochlea? If so, are there regimes of behavior where we can expect the initial hexagonal lattice to be stable to cell-cell signaling? Can final cell geometry be 'tuned' by modifying cell signaling parameters? While such fundamental questions lay outside the mechanistic scope explored in this thesis, the tools presented within should allow for immediate investigation.

Appendix A

Image segmentation and model simulation

A.1 Image segmentation assisted by machine learning

In-vivo data was segmented using a combination of *ilastik* classification and a custom pipeline implemented in MATLAB. In this section, we outline the algorithmic details at a high level. *ilastik*, a supervised machine learning classifier, was used to classify each image into a 'membrane' and 'background' class [162]. Specifically, *ilastik* is a random forest classifier that specifies 100 decision trees for each pixel. Parameters of the decision tree depend upon image parameters such as intensity and shape at multiple length scales (Gaussian-blur of varying sizes). In this context, the output of *ilastik* is the fraction of trees which decided on 'membrane' relative to the 100 initialized per pixel and thus is an estimate for the pixel probability [162]. This result is then further filtered using a Laplacian of Gaussian filter and subsequently segmented using MATLAB's watershed function.

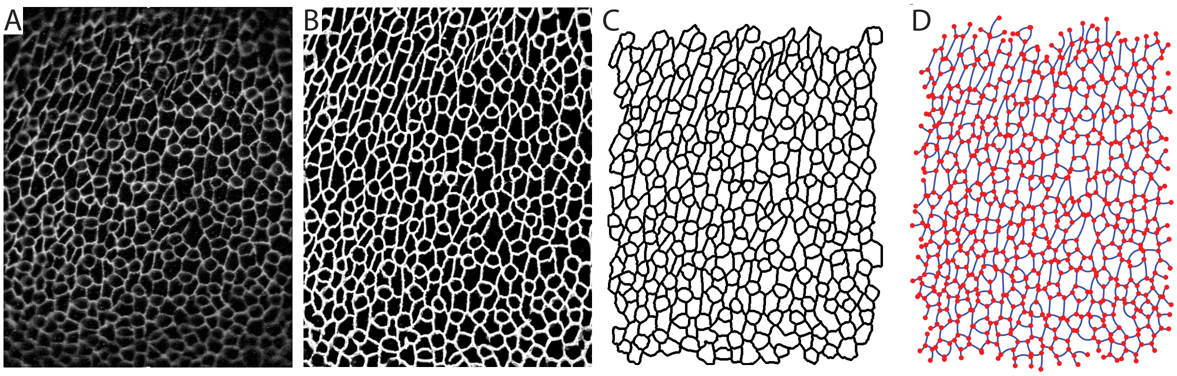

Figure A.1: a) A raw image of the chick cochlea during neurogenesis. b) Probability map output from ilastik after classification. c) Segmentation produced via watershed algorithm. d) Curved vertex model fit from the segmentation.

The watershed algorithm partitions a grayscale image (in our case the image of probabilities per pixel) into distinct basins separated by intensity ridges. Specifically, one can imagine the grayscale image as a topographical map containing regions of low intensity (basins) that are separated by lines of high intensity (mountain ranges). Starting from the local minima of each basin, we 'flood' each basin; the line of intersection between two flooding points defines the intersection of the region. Watershed-based algorithms suffer greatly from over-segmentation. If there are many local minima within a single basin which originate from noise, each will act as a flooding source resulting in a segmentation that corresponds to the noise source. We fix this issue by seeding basins, defined as a black and white mask obtained by suitable thresholding of the background class output from *ilastik*.

The output of MATLAB's watershed algorithm is a label matrix of the original size of the image that indexes each cell found, separated by the 'ridges' of equal intensity. Cellular boundaries were skeletonized using MATLAB's bwmorph 'skel' feature, which uses an iterative thinning procedure that preserves topology of the original graph. The output of the 'skel' algorithm is a black and white mask in which the pixel registers as 1 if it belongs to a cell boundary (thinned to be 1 pixel thick) or 0 otherwise. All data is stored within a custom data structure.

A.2 Measuring vertex position and edge curvature

Given a skeletonization of the segmented cell boundaries, one can easily estimate each vertex position within the image, as well as the curvature of every intercellular edge. Vertex positions were obtained using the MATLAB's bwmorph 'branchpoints' algorithm. As the skeletonization produced during the segmentation process above is an 8-connected graph, any pixel that belongs to an edge will have only two neighboring pixels that are also 1. Conversely, a vertex will have three or more neighbors equal to a cell boundary - this is defined as a branchpoint of the original skeletonization. Denote the measured position of vertex i as $\boldsymbol{r}_i$

The shape of each intercellular edge is estimated by removing the branchpoints from the skeletonization and then analyzing the pixels for each connected component of the resultant mask. Denote the set of pixels belonging to the edge that partitions cells α, β

as $\boldsymbol{r}_{\alpha\beta|n}$ where $n \in [1, ..., N]$. Edge curvatures are obtained by fitting each set of pixels to a circle, ensuring that the two vertices i, j that lie on the border of the edge are on exactly on the circumference. This is achieved by minimizing the following energy for each edge with respect to ρ

$$E_{circle} = \frac{1}{N} \sum_n \left| \boldsymbol{r}_{\alpha\beta|n} - \frac{\boldsymbol{r}_i + \boldsymbol{r}_j}{2} - \rho \left[\hat{\boldsymbol{z}} \wedge \hat{\boldsymbol{r}}_{ij} \right] \right|^2 \tag{A.1}$$

The estimated radius of curvature is $R_{\alpha\beta} = \sqrt{(r_{ij}/2)^2 + \rho_*^2}$ where ρ_* is the value which minimizes Eq. A.1. If the edge is smaller than three pixels, we assume it has infinite curvature.

Myosin and cadherin was measured using the pixels for each edge obtained from the segmentation produced via the watershed algorithm. To account for segmentation errors, the pixels were by one pixel to increase their width. The average intensity over the set of pixels was used as a proxy for protein line density.

A.3 Cell tracking

The above segmentation algorithm can be ran over every time-frame captured during the image acquisition of the developmental process. This will produce a corresponding label matrix for each time point. Importantly, the labels that cells are given in each image are indexed by their spatial position and thus have no memory across time-points - i.e. the cell labeled as index 10 in time-point t will not generally be 10 in time-point $t + 1$. The goal of tracking is to recover the list of labels one actual cell has in every time-point.

Tracking was done using the point-matching of cell centroids after correcting for PIV (Particle Image Velocimetry) estimated flow fields between time points. PIV flow fields were estimated using cross-correlation between gridded regions defined on our image [1]. Specifically, denote the position of segmented cells in time-point t as $\boldsymbol{R}_\alpha(t)$ and the PIV flow field at this position to be $\boldsymbol{v}_\alpha(t)$. Tracking is then done by finding the set of indices α' that minimizes the following sum

$$D \equiv \sum_\alpha |\boldsymbol{R}_{alpha}(t) - \boldsymbol{R}_{\alpha'}(t-1) - \boldsymbol{v}_{\alpha'}(t-1)\Delta t|^2 \tag{A.2}$$

We impose the matching be bipartite; only one cell can be tracked into another in the subsequent time-point. This can be generalized to include divisions by simply doubling the cells in time-point t to allow potential double matches. As posed, tracking is equivalent to the Munkres assignment problem [118] and can be solved in polynomial time using the Hungarian algorithm [95].

Given tracked cells, we can easily track edges and vertices throughout time as well. Edges were tracked by simply tracking pairs of cells that remain in contact (as determined by the segmentation algorithm above) throughout the course of the movie. T1 transitions thus ‘destroy’ one edge and ‘create’ another. Dynamics of edge chemistry were then obtained by looking at myosin/cadherin over time for each tracked edge. Similarly, vertices were obtained by tracking triplets of cells that remained neighbors.

A.4 Implementation of model simulation

All dynamical equations of motion were numerically integrated using MATLAB's ODE15s solver as the large time-scale separation between chemical feedback and mechanical equilibration resulted in a stiff system of equations. Fast results were obtained by storing all topological adjacency matrices (e.g. which vertices were involved in which bonds, list of vertices belonging to each cell, etc.) as sparse matrices that represented discrete exterior derivatives. Specifically, we defined matrices $d^{(0)}$ and $d^{(1)}$ to be

$$d^{(0)}_{<i,j>,k} \equiv \delta_{k,i} - \delta_{k,j} \qquad d^{(1)}_{\alpha,<i,j>} \equiv \sum_{<k,l>\in\mathcal{E}_\alpha} \sigma_{\alpha,<i,j>}\delta_{<i,j>,<k,l>} \tag{A.3}$$

$\mathcal{E}_\alpha$ denotes the set of all edges belonging to cell α. Thus, one can think of $d^{(0)}$ as the exterior derivative acting on zero-forms (vertices) which maps into the space of one-forms (edges). Conversely, $d^{(1)}$ is the exterior derivative acting on one-forms. $\sigma_{\alpha,<i,j>}$ is chosen such that $d^{(1)}d^{(0)} = 0$ and thus the discrete Stokes' theorem holds. As MATLAB's native language is matrices and not iterative loops, matrix multiplication was utilized to quickly convert between various geometric quantities such as vertex positions and edge lengths.

The topological quantities were also taken to be dynamical variables as T1 events were allowed and common. T1 processes were implemented using MATLAB's ODE event functionality which allowed us to stop numerical integration of the equations if any given edge's length fell below a user-specified value r_c. Once an event was recognized, the T1 exchange was enforced manually by updating all sparse topological matrices and rotating the bond in question by a random angle centered around $\pi/2$. This was then used as the initial condition to reinitialize the numerical integration. Under this scheme, a stable four-fold vertex is represented as a cyclic series of T1 events for a single bond. Furthermore, resolution of rosettes was allowed via multiple T1 events occurring simultaneously on neighboring bonds.

For the 2D rheology simulation presented in Chapter 2, a 15 x 15 square of cells was initialized in a slightly disordered hexagonal lattice under constant pressure to balance against the internal tension. Sinusoidal external forces were attached to the vertices on the vertical boundary. Strain rate was measured on vertical junctions throughout the bulk.

Simulation of the GBE model presented in Chapter 4 was started with a hexagonal array of ~ 100 cells with weak geometric disorder. Myosin pulses were modeled as a stochastic force on the dynamical equation of myosin. The amplitude of fluctuations was strongly dependent upon the edge orientation. This was sufficient to drive an ordered transition towards a geometry dominated by DV-oriented stress-cables, taken to be the vertical axis of the simulation.

A.5 Derivation of Cellular-Scale and Mesoscopic Stress Tensor

The algorithm presented in Chapter 3 infers the mechanics of planar cell packings that behave as quasistatic dry foams. However, in many applications one is more interested in the mesoscopic stress rather than cellular scale mechanics. As such, in this section we define the stress tensor of the curved network model, show it's divergence-less and describe the coarse-graining procedure from cell to tissue level forces. Each cell is modeled as an 'active' bubble, and as such, inside the bulk of cell α the stress tensor σ^{ab} is

$$\sigma^{ab} = -p_\alpha \delta^{ab} \tag{A.4}$$

Similarly, the stress tensor on edge α, β (interface between cells α and β) is

$$\sigma^{ab} = T_{\alpha\beta}\, \delta(\boldsymbol{r} - \boldsymbol{r}_{\alpha\beta})\, \hat{\tau}^a_{\alpha\beta} \hat{\tau}^b_{\alpha\beta} \tag{A.5}$$

where $\hat{\boldsymbol{\tau}}_{\alpha\beta}$ denotes the tangent vector along the circular arc and $\delta(\boldsymbol{r} - \boldsymbol{r}_{\alpha\beta})$ localizes the stress to the interface. As such, the functional form for the stress tensor in the vicinity of interface α, β (depicted in Fig. A.2a) is

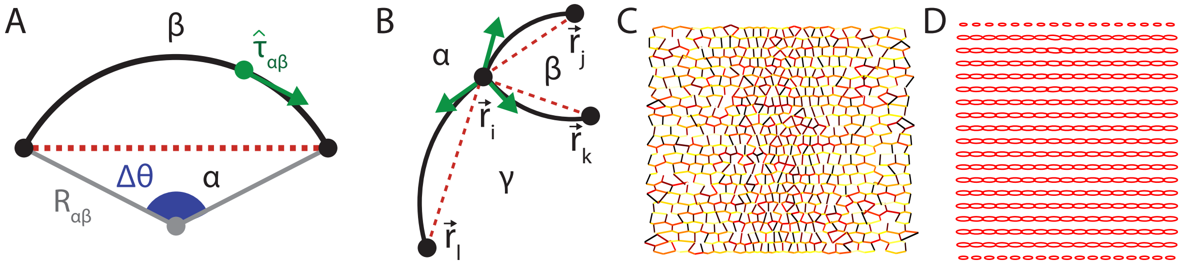

Figure A.2: (a) Diagram of definitions used to compute divergence of stress near an interface. (b) Analogous plot as in (a) used to compute divergence in the vicinity of vertex i

$$\begin{aligned} \sigma^{ab}(\boldsymbol{r}) = &-\big[p_\alpha H\left(R_{\alpha\beta} - r\right) + p_\beta H\left(r - R_{\alpha\beta}\right)\big]\delta^{ab} \\ &+ T_{\alpha\beta}\, \delta(r - R_{\alpha\beta})\, [H(\theta + \Delta\theta/2) - H(\theta - \Delta\theta/2)]\ \hat{\tau}^a_{\alpha\beta} \hat{\tau}^b_{\alpha\beta} \end{aligned} \tag{A.6}$$

where $H(x)$ is the Heaviside step function, $r = |\boldsymbol{r}|$ and θ is the angle measured from the vertical axis and $\hat{\boldsymbol{\tau}}_{\alpha\beta} = \hat{\boldsymbol{z}} \wedge \frac{1}{|\boldsymbol{r} - \boldsymbol{\rho}_{\alpha\beta}|}\left[\boldsymbol{r} - \boldsymbol{\rho}_{\alpha\beta}\right]$. With no loss of generality, we've chosen a polar coordinate system with origin at the centroid of the circular arc. The divergence of this tensor is

$$\partial_a \sigma^{ab} = \left[(p_\alpha - p_\beta) - \frac{T_{\alpha\beta}}{R_{\alpha\beta}} \right] \delta(r - R_{\alpha\beta}) = 0 \tag{A.7}$$

As expected, since the curvature of the interface obeys the Young-Laplace Law the divergence is zero. Unfortunately, this result is only valid *in the bulk of the edge.* Lastly, we consider the divergence of the stress tensor in the vicinity of the tri-fold vertex, depicted in Fig. A.2b. The functional form is

$$\begin{aligned}
\sigma^{ab}(\boldsymbol{r}) = -\Big[& p_\alpha H\left(|\boldsymbol{r} - \boldsymbol{\rho}_{\alpha\beta}| - R_{\alpha\beta}\right) H\left(R_{\gamma\alpha} - |\boldsymbol{r} - \boldsymbol{\rho}_{\gamma\alpha}|\right) + \\
& p_\beta H\left(|\boldsymbol{r} - \boldsymbol{\rho}_{\beta\gamma}| - R_{\beta\gamma}\right) H\left(R_{\alpha\beta} - |\boldsymbol{r} - \boldsymbol{\rho}_{\alpha\beta}|\right) + \\
& p_\gamma H\left(|\boldsymbol{r} - \boldsymbol{\rho}_{\gamma\alpha}| - R_{\gamma\alpha}\right) H\left(R_{\beta\gamma} - |\boldsymbol{r} - \boldsymbol{\rho}_{\beta\gamma}|\right) \Big] \delta^{ab} + \\
& T_{\alpha\beta}\, \hat{\tau}^a_{\alpha\beta} \hat{\tau}^b_{\alpha\beta}\, \delta(|\boldsymbol{r} - \boldsymbol{\rho}_{\alpha\beta}| - R_{\alpha\beta}) H(\boldsymbol{r} \cdot \hat{\boldsymbol{\tau}}_{\alpha\beta}) + \\
& T_{\beta\gamma}\, \hat{\tau}^a_{\beta\gamma} \hat{\tau}^b_{\beta\gamma}\, \delta(|\boldsymbol{r} - \boldsymbol{\rho}_{\beta\gamma}| - R_{\beta\gamma}) H(\boldsymbol{r} \cdot \hat{\boldsymbol{\tau}}_{\beta\gamma}) + \\
& T_{\gamma\alpha}\, \hat{\tau}^a_{\gamma\alpha} \hat{\tau}^b_{\gamma\alpha}\, \delta(|\boldsymbol{r} - \boldsymbol{\rho}_{\gamma\alpha}| - R_{\gamma\alpha}) H(\boldsymbol{r} \cdot \hat{\boldsymbol{\tau}}_{\gamma\alpha})
\end{aligned}$$

The step functions associated to the contributions from each edge are necessary to impose the discontinuity of stress across the vertex. The remaining step is to compute the divergence of the expression. The derivative of each pressure term is

$$\partial_c\Bigg[p_\alpha H\left(|\boldsymbol{r}-\boldsymbol{\rho}_{\alpha\beta}|-R_{\alpha\beta}\right)H\left(R_{\gamma\alpha}-|\boldsymbol{r}-\boldsymbol{\rho}_{\gamma\alpha}|\right)\Bigg]=$$

$$-p_\alpha\,\varepsilon^{cd}\Bigg[\hat{\tau}^d_{\alpha\beta}\,\delta\left(|\boldsymbol{r}-\boldsymbol{\rho}_{\alpha\beta}|-R_{\alpha\beta}\right)H\left(R_{\gamma\alpha}-|\boldsymbol{r}-\boldsymbol{\rho}_{\gamma\alpha}|\right)-$$

$$\hat{\tau}^d_{\gamma\alpha}\,\delta\left(R_{\gamma\alpha}-|\boldsymbol{r}-\boldsymbol{\rho}_{\gamma\alpha}|\right)H\left(|\boldsymbol{r}-\boldsymbol{\rho}_{\alpha\beta}|-R_{\alpha\beta}\right)\Bigg]$$

Summing together the contributions from each cell, the contribution of bulk pressures to the divergence at vertex i is found to be

$$\partial_a\sigma^{ab}_{pressure}(\boldsymbol{r}_i)=\varepsilon^{bc}\left[\Delta p_{\alpha\beta}\hat{\tau}^c_{\alpha\beta}+\Delta p_{\beta\gamma}\hat{\tau}^c_{\beta\gamma}+\Delta p_{\gamma\alpha}\hat{\tau}^c_{\gamma\alpha}\right]\delta(0)H(0)$$

Similarly, the divergence of each edge term is

$$\partial_a\Bigg[T_{\alpha\beta}\,\hat{\tau}^a_{\alpha\beta}\hat{\tau}^b_{\alpha\beta}\,\delta(|\boldsymbol{r}-\boldsymbol{\rho}_{\alpha\beta}|-R_{\alpha\beta})H(\boldsymbol{r}\cdot\hat{\boldsymbol{\tau}}_{\alpha\beta})\Bigg]=-\frac{T_{\beta\alpha}}{R_{\beta\alpha}}\epsilon^{bc}\hat{\tau}^c_{\alpha\beta}\delta(0)H(0)+T_{\alpha\beta}\hat{\tau}^b_{\alpha\beta}\delta^2(0)$$

The first term exactly cancels out the contribution from the bulk pressure, leaving us with

$$\partial_a\sigma^{ab}(\boldsymbol{r}_i)=\left[T_{\alpha\beta}\hat{\tau}^b_{\alpha\beta}+T_{\beta\gamma}\hat{\tau}^b_{\beta\gamma}+T_{\gamma\alpha}\hat{\tau}^b_{\gamma\alpha}\right]\delta^2(0)\qquad\text{(A.8)}$$

This is precisely due zero to our assumption of force balance. Thus we conclude that, as defined, σ^{ab} is balanced everywhere, directly following from edges with curvature that obey Laplace's Law and vertices at force balance. Armed with a sensible construction, we can compute the average stress per cell.

$$\bar{\sigma}_\alpha^{ab} = \frac{1}{A_\alpha} \int\limits_{A_\alpha} d^2\boldsymbol{r}\, \sigma^{ab}(\boldsymbol{r}) \tag{A.9}$$

The last equality explicitly utilized the fact that the stress tensor is balanced and thus the only contribution to the sum are the boundary forces $\hat{\boldsymbol{n}} \cdot \sigma$. In the context of the present model, the average stress per cell simplifies to

$$\bar{\sigma}_\alpha^{ab} = \frac{1}{A_\alpha} \int_{A_\alpha} d^2\boldsymbol{r}\, \sigma^{ab}(\boldsymbol{r}) = p_\alpha \delta^{ab} + \sum_{\{\beta\}_\alpha} \frac{T_{\alpha\beta}}{2A_\alpha} \int\limits_{\boldsymbol{r}_{\alpha\beta}} dr\, \hat{\tau}_{\alpha\beta}^a \hat{\tau}_{\alpha\beta}^b \tag{A.10}$$

This result was used in the main text to help predict future spindle axis in Chapter 3.

Lastly, we outline a systematic manner to coarse-grain the stress tensor to obtain mechanics at the mesoscopic scale. Given smoothing kernel $K(|\boldsymbol{r} - \boldsymbol{r}'|, \eta)$, where η parameterizes the length-scale of averaging, we define the coarse-grained stress tensor

$$\tilde{\sigma}^{ab}(\boldsymbol{r}) = \int d^2\boldsymbol{r}'\, K(|\boldsymbol{r} - \boldsymbol{r}'|, \eta)\, \sigma^{ab}(\boldsymbol{r}') \tag{A.11}$$

Provided the kernel goes to zero at the boundary, the stress tensor remains balanced under coarse-graining.

$$\partial_a \tilde{\sigma}^{ab}(\boldsymbol{r}) = \frac{\partial}{\partial \boldsymbol{r}_a} \int d^2\boldsymbol{r}'\, K(|\boldsymbol{r} - \boldsymbol{r}'|, \alpha) \sigma^{ab}(\boldsymbol{r}') = \int d^2\boldsymbol{r}'\, K(|\boldsymbol{r} - \boldsymbol{r}'|, \eta) \partial_a \sigma^{ab}(\boldsymbol{r}') = 0 \tag{A.12}$$

To ensure the average stress is invariant, $K(|\boldsymbol{r} - \boldsymbol{r}'|, \alpha)$ must be normalized. As such, the stress tensor at scale η is defined

$$\tilde{\sigma}^{ab}(\boldsymbol{r}, \eta) = \frac{1}{2\pi\eta^2} \int d^2\boldsymbol{r}'\, e^{-\frac{|\boldsymbol{r} - \boldsymbol{r}'|^2}{2\eta^2}}\, \sigma^{ab}(\boldsymbol{r}') \tag{A.13}$$

A graphical example of the coarse-graining procedure is shown in Fig. A.2c,d.

A.6 Global stress inference on curved surfaces

Most, if not all, epithelial tissues are locally flat (for small patches of cells) but curved at the organ-scale. For example, curvature of *Drosophila* embryonic epithelium becomes non-negligible for regions containing ~ 100 cells. As formulated in Chapter 3, the mechanical inverse is only well-defined for planar graphs. To this end, we leverage the locality of our algorithm to formulate a tractable inference scheme for the balanced mechanical stress in a curved tissue's tangent plane. Specifically, due to the inclusion of edge curvature information, the inverse is massively over-determined which allows one to 'measure' both bulk and boundary stress using information of just bulk geometry. Consequently, global mechanical patterns can be 'stitched' together by inferring stress on local patches of cells that can, with good approximation, be treated as planar. The blue cell array depicted in Fig. A.3a denotes the 'true' apical surface of the epithelial tissue. Provided the area of interest is much smaller than the surface's radius of curvature, we can fit a well defined tangent plane to the patch. Let $\boldsymbol{R}_i^n$ denote the 3D position of the i^{th} vertex within patch n and thus is a matrix of size 3 x v_n where v_n is the number of vertices contained in patch n. The best fit triad of vectors is obtained easily via an SVD decomposition

$$\boldsymbol{R}_i^n = U_n \Sigma V_n^T \tag{A.14}$$

The approximate planar graph of patch n, shown as the black cell array in Fig. A.3a, is obtained by projecting $\boldsymbol{R}_i^n$ onto the two rows of U_n associated to the two largest singular values. As shown in Fig. A.3b, the dual weighted triangulation can be fit to the

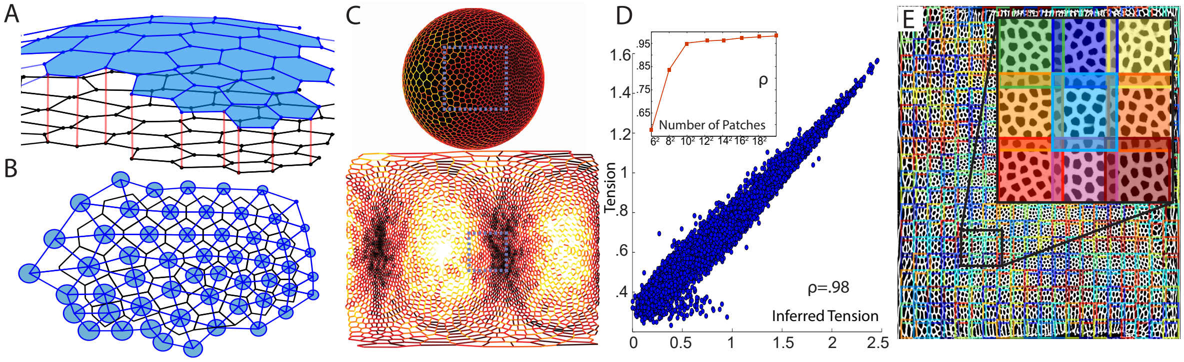

Figure A.3: (a) Graphical depiction of the process used to infer stresses in the tangent plane of a small region of cells. The patch shown enclosed in the blue box in (c), shown as the blue shaded cells, is projected onto the best fit tangent plane diagram, shown in black. The red lines depict equivalent vertices for ease. (b) The inferred weighted triangulation for the planar graph produced by the procedure outlined in (a). This is used as an estimate for the tangential balanced stresses within the patch. (c) A synthetic spherical embryo of ~ 3000 cells, plotted both in the embedded space, as well as the cylindrical unwrapping. Simulated tensions are plotted as a heatmap. (d) Scatter plot between the inferred tensions using the workflow outlined and the known tensions shown in (a). The inset displays the dependence on the number of patches used to cover the sphere. As was expected, correlation is monotonic with sampling resolution. (e) A snapshot of cell outlines during Drosophila embryogenesis at the onset of ventral furrow formation. Instead of minimizing the quadratic energy over all degrees of freedom simultaneously, the embryo is partitioned into overlapping patches, as shown overlayed on cell membranes. The inversion is done separately on each patch and then stitched together. Grid size was chosen to include 30 cells as it was small enough to neglect curvature effects.

approximated planar graph using the algorithm outlined in the main text to obtain an estimate for the balanced stress within the tangent plane of patch n.

Alas, the weighted dual triangulation is unique up to an overall scale, owing to the fact that mechanical equilibrium is unchanged by re-scaling all tensions and pressures by an overall constant. In the present case, this implies that there is an overall scale that is unknown *for each defined patch*, defined as λ_{nm}, that must be determined by continuity. As patches are defined to overlap (shown in Fig. A.3e. for Drosophila embryo) a subset of edges are involved in multiple inferred regions. Scales between adjacent patches can be matched together by enforcing equivalence of tensions in all shared edges. This was achieved by minimizing

$$\frac{1}{2}\left[\sum_{n,m=1}^{N}\sum_{n'=n-1}^{n+1}\sum_{m'=m-1}^{m+1}\sum_{e\in[\mathcal{E}_{nm}\cap\mathcal{E}_{n'm'}]}\left[\lambda_{nm}T_e^{nm}-\lambda_{n'm'}T_e^{n'm'}\right]^2\right]+\Lambda\left[\sum_{n,m=1}^{N}\lambda_{nm}-n_{patches}\right] \tag{A.15}$$

$e\in[\mathcal{E}_{nm}\cap\mathcal{E}_{n'm'}]$ denotes the set of all edges that are shared by patch (n,m) and (n',m'). In words, scale λ_{nm} for each patch is found by minimizing the squared difference between inferred tensions of edges shared by adjacent patches globally, subject to the constraint that the average scale is 1 to ensure a non-trivial solution $\lambda_{nm}\neq 0$.

The outlined procedure was validated in-silico for synthetic spherical embryos containing roughly 3000 cells, with mechanics patterned by a vertex model minimized on the surface of a sphere. An example of a simulated embryo with azimuthal pattern of tension is shown in Fig. A.3c, both in the embedding space and in the cylindrical unwrapping of the sphere. As shown in Fig. A.3e for Drosophila, the surface of the embryo is partitioned into overlapping uniform patches. Mechanics was inferred in each patch as previously described. As shown in Fig. A.3d, great agreement between inferred and known tensions was found *provided* the patch size was small compared to surface curvature. The inset shows this occurred when the defined patches contained 100 or less cells. This was used to define the patch size used in the empirical measurements during Drosophila embryogenesis as shown in Fig. A.3e.

ImSaNe [73] was used to measure, parameterize, and store the surface and embedding coordinates of the Drosophila embryonic surface. Segmentation of cells was done using the cylindrical mapping of the embyro. The 3D vertex positions were subsequently estimated using the embedding grids obtained from the ImSaNe algorithm [73].

Bibliography

[1] Ronald J Adrian. Twenty years of particle image velocimetry. *Experiments in fluids*, 39(2):159–169, 2005.

[2] Benoît Aigouy, Reza Farhadifar, Douglas B Staple, Andreas Sagner, Jens-Christian Röper, Frank Jülicher, and Suzanne Eaton. Cell flow reorients the axis of planar polarity in the wing epithelium of drosophila. *Cell*, 142(5):773–786, 2010.

[3] Bruce Alberts, Dennis Bray, Julian Lewis, Martin Raff, Keith Roberts, and James D Watson. Molecular biology of the cell. 3rd. *New York: Garland Pub*, 43(1294):67, 1994.

[4] Silvanus Alt, Poulami Ganguly, and Guillaume Salbreux. Vertex models: from cell mechanics to tissue morphogenesis. *Phil. Trans. R. Soc. B*, 372(1720):20150520, 2017.

[5] Philip W Anderson et al. More is different. *Science*, 177(4047):393–396, 1972.

[6] Kunihiro Baba, Ritei Shibata, and Masaaki Sibuya. Partial correlation and conditional correlation as measures of conditional independence. *Australian & New Zealand Journal of Statistics*, 46(4):657–664, 2004.

[7] Saumendra Bajpai, Joana Correia, Yunfeng Feng, Joana Figueiredo, Sean X Sun, Gregory D Longmore, Gianpaolo Suriano, and Denis Wirtz. α-catenin mediates initial e-cadherin-dependent cell–cell recognition and subsequent bond strengthening. *Proceedings of the National Academy of Sciences*, 105(47):18331–18336, 2008.

[8] Kapil Bambardekar, Raphaël Clément, Olivier Blanc, Claire Chardès, and Pierre-François Lenne. Direct laser manipulation reveals the mechanics of cell contacts in vivo. *Proceedings of the National Academy of Sciences*, 112(5):1416–1421, 2015.

[9] Jonathan BL Bard and Jonathan Bard. *Morphogenesis: the cellular and molecular processes of developmental anatomy*, volume 23. Cambridge University Press, 1992.

[10] Buzz Baum. Personal communication.

[11] Buzz Baum and Marios Georgiou. Dynamics of adherens junctions in epithelial establishment, maintenance, and remodeling. *The Journal of cell biology*, 192(6):907–917, 2011.

[12] LV Beloussov, JG Dorfman, and VG Cherdantzev. Mechanical stresses and morphological patterns in amphibian embryos. *Development*, 34(3):559–574, 1975.

[13] Poul M Bendix, Gijsje H Koenderink, Damien Cuvelier, Zvonimir Dogic, Bernard N Koeleman, William M Brieher, Christine M Field, L Mahadevan, and David A Weitz. A quantitative analysis of contractility in active cytoskeletal protein networks. *Biophysical journal*, 94(8):3126–3136, 2008.

[14] Claire Bertet, Lawrence Sulak, and Thomas Lecuit. Myosin-dependent junction remodelling controls planar cell intercalation and axis elongation. *Nature*, 429(6992):667, 2004.

[15] Guy B Blanchard, Alexandre J Kabla, Nora L Schultz, Lucy C Butler, Benedicte Sanson, Nicole Gorfinkiel, L Mahadevan, and Richard J Adams. Tissue tectonics: morphogenetic strain rates, cell shape change and intercalation. *Nature methods*, 6(6):458–464, 2009.

[16] J Todd Blankenship, Stephanie T Backovic, Justina SP Sanny, Ori Weitz, and Jennifer A Zallen. Multicellular rosette formation links planar cell polarity to tissue morphogenesis. *Developmental cell*, 11(4):459–470, 2006.

[17] Nicolas Borghi, Maria Sorokina, Olga G Shcherbakova, William I Weis, Beth L Pruitt, W James Nelson, and Alexander R Dunn. E-cadherin is under constitutive actomyosin-generated tension that is increased at cell–cell contacts upon externally applied stretch. *Proceedings of the National Academy of Sciences*, 109(31):12568–12573, 2012.

[18] Floris Bosveld, Isabelle Bonnet, Boris Guirao, Sham Tlili, Zhimin Wang, Ambre Petitalot, Raphaël Marchand, Pierre-Luc Bardet, Philippe Marcq, François Graner, et al. Mechanical control of morphogenesis by fat/dachsous/four-jointed planar cell polarity pathway. *Science*, 336(6082):724–727, 2012.

[19] James Briscoe and Anna Kicheva. The physics of development 100years after d'arcy thompson's on growth and form. *Mechanisms of Development*, 2017.

[20] G Wayne Brodland, Vito Conte, P Graham Cranston, Jim Veldhuis, Sriram Narasimhan, M Shane Hutson, Antonio Jacinto, Florian Ulrich, Buzz Baum, and Mark Miodownik. Video force microscopy reveals the mechanics of ventral furrow invagination in drosophila. *Proceedings of the National Academy of Sciences*, 107(51):22111–22116, 2010.

[21] Craig D Buckley, Jiongyi Tan, Karen L Anderson, Dorit Hanein, Niels Volkmann, William I Weis, W James Nelson, and Alexander R Dunn. The minimal cadherin-catenin complex binds to actin filaments under force. *Science*, 346(6209):1254211, 2014.

[22] Lucy C Butler, Guy B Blanchard, Alexandre J Kabla, Nicola J Lawrence, David P Welchman, L Mahadevan, Richard J Adams, and Benedicte Sanson. Cell shape changes indicate a role for extrinsic tensile forces in drosophila germ-band extension. *Nature cell biology*, 11(7):859, 2009.

[23] Danfeng Cai, Shann-Ching Chen, Mohit Prasad, Li He, Xiaobo Wang, Valerie Choesmel-Cadamuro, Jessica K Sawyer, Gaudenz Danuser, and Denise J Montell. Mechanical feedback through e-cadherin promotes direction sensing during collective cell migration. *Cell*, 157(5):1146–1159, 2014.

[24] Otger Campàs, Tadanori Mammoto, Sean Hasso, Ralph A Sperling, Daniel O'connell, Ashley G Bischof, Richard Maas, David A Weitz, Lakshminarayanan Mahadevan, and Donald E Ingber. Quantifying cell-generated mechanical forces within living embryonic tissues. *Nature methods*, 11(2):183–189, 2014.

[25] Sadi Carnot. Reflections on the motive power of fire, and on machines fitted to develop that power. *Paris: Bachelier*, 1824.

[26] Richard W Carthew. Pattern formation in the drosophila eye. *Current opinion in genetics & development*, 17(4):309–313, 2007.

[27] Matthieu Cavey and Thomas Lecuit. Molecular bases of cell–cell junctions stability and dynamics. *Cold Spring Harbor perspectives in biology*, 1(5):a002998, 2009.

[28] Martin Chalfie, Yuan Tu, Ghia Euskirchen, William W Ward, and Douglas C Prasher. Green fluorescent protein as a marker for gene expression. *Science*, pages 802–805, 1994.

[29] Kevin K Chiou, Lars Hufnagel, and Boris I Shraiman. Mechanical stress inference for two dimensional cell arrays. *PLoS computational biology*, 8(5):e1002512, 2012.

[30] Wangsun Choi, Bipul R Acharya, Grégoire Peyret, Marc-Antoine Fardin, René-Marc Mège, Benoit Ladoux, Alan S Fanning, Mark Peifer, et al. Remodeling the zonula adherens in response to tension and the role of afadin in this response. *J Cell Biol*, 213(2):243–260, 2016.

[31] Philippe G Ciarlet, Cristinel Mardare, and Ming Shen. Recovery of a displacement field from its linearized strain tensor field in curvilinear coordinates. *Comptes Rendus Mathematique*, 344(8):535–540, 2007.

[32] Paolo Cignoni, Marco Callieri, Massimiliano Corsini, Matteo Dellepiane, Fabio Ganovelli, and Guido Ranzuglia. Meshlab: an open-source mesh processing tool. In *Eurographics Italian Chapter Conference*, volume 2008, pages 129–136, 2008.

[33] Mireille Mae Claessens, Mark Bathe, Erwin Frey, and Andreas R Bausch. Actin-binding proteins sensitively mediate f-actin bundle stiffness. *Nature materials*, 5(9):748–753, 2006.

[34] Anabel E-M Clemen, Mojca Vilfan, Johann Jaud, Junshan Zhang, Michael Bärmann, and Matthias Rief. Force-dependent stepping kinetics of myosin-v. *Biophysical journal*, 88(6):4402–4410, 2005.

[35] JD Cockcropt. Rutherford at manchester. *Physics Bulletin*, 15(2):40, 1964.

[36] Claudio Collinet, Matteo Rauzi, Pierre-Francois Lenne, and Thomas Lecuit. Local and tissue-scale forces drive oriented junction growth during tissue extension. *Nature cell biology*, 17(10):1247, 2015.

[37] Jeffrey T Corwin, Jay E Jones, Akiko Katayama, Matthew W Kelley, and Mark E Warchol. Hair cell regeneration: the identities of progenitor cells, potential triggers and instructive cues. *Regeneration of vertebrate sensory receptor cells*, 160:103–120, 1991.

[38] Mark C Cross and Pierre C Hohenberg. Pattern formation outside of equilibrium. *Reviews of modern physics*, 65(3):851, 1993.

[39] Sara Morais da Silva and Jean-Paul Vincent. Oriented cell divisions in the extending germband of drosophila. *Development*, 134(17):3049–3054, 2007.

[40] Lance A Davidson and Buzz Baum. Making waves: the rise and fall and rise of quantitative developmental biology. *Development*, 139(17):3065–3069, 2012.

[41] Stephen J Day and Peter A Lawrence. Measuring dimensions: the regulation of size and shape. *Development*, 127(14):2977–2987, 2000.

[42] Simon De Beco, Jean-Baptiste Perney, Sylvie Coscoy, and François Amblard. Mechanosensitive adaptation of e-cadherin turnover across adherens junctions. *PloS one*, 10(6):e0128281, 2015.

[43] Karl Deisseroth. Optogenetics. *Nature methods*, 8(1):26–29, 2011.

[44] Boris Delaunay. Sur la sphere vide. *Izv. Akad. Nauk SSSR, Otdelenie Matematicheskii i Estestvennyka Nauk*, 7(793-800):1–2, 1934.

[45] Micah Dembo, Tim Oliver, A Ishihara, and K Jacobson. Imaging the traction stresses exerted by locomoting cells with the elastic substratum method. *Biophysical journal*, 70(4):2008–2022, 1996.

[46] Micah Dembo, DC Torney, K Saxman, and D Hammer. The reaction-limited kinetics of membrane-to-surface adhesion and detachment. *Proceedings of the Royal Society of London B: Biological Sciences*, 234(1274):55–83, 1988.

[47] Roberto Dominguez and Kenneth C Holmes. Actin structure and function. 2011.

[48] Wolfgang Driever and Christiane Nüsslein-Volhard. The bicoid protein determines position in the drosophila embryo in a concentration-dependent manner. *Cell*, 54(1):95–104, 1988.

[49] Efi Efrati, Eran Sharon, and Raz Kupferman. Elastic theory of unconstrained non-euclidean plates. *Journal of the Mechanics and Physics of Solids*, 57(4):762–775, 2009.

[50] Efi Efrati, Eran Sharon, and Raz Kupferman. Non-euclidean plates and shells, 2010.

[51] Raphaël Etournay, Marko Popović, Matthias Merkel, Amitabha Nandi, Corinna Blasse, Benoît Aigouy, Holger Brandl, Gene Myers, Guillaume Salbreux, Frank Jülicher, et al. Interplay of cell dynamics and epithelial tension during morphogenesis of the drosophila pupal wing. *Elife*, 4:e07090, 2015.

[52] Reza Farhadifar, Jens-Christian Röper, Benoit Aigouy, Suzanne Eaton, and Frank Jülicher. The influence of cell mechanics, cell-cell interactions, and proliferation on epithelial packing. *Current Biology*, 17(24):2095–2104, 2007.

[53] Rodrigo Fernandez-Gonzalez, Sérgio de Matos Simoes, Jens-Christian Röper, Suzanne Eaton, and Jennifer A Zallen. Myosin ii dynamics are regulated by tension in intercalating cells. *Developmental cell*, 17(5):736–743, 2009.

[54] Alexander G Fletcher, Miriam Osterfield, Ruth E Baker, and Stanislav Y Shvartsman. Vertex models of epithelial morphogenesis. *Biophysical journal*, 106(11):2291–2304, 2014.

[55] Daniel A Fletcher and R Dyche Mullins. Cell mechanics and the cytoskeleton. *Nature*, 463(7280):485, 2010.

[56] Gabor Forgacs, Ramsey A Foty, Yinon Shafrir, and Malcolm S Steinberg. Viscoelastic properties of living embryonic tissues: a quantitative study. *Biophysical journal*, 74(5):2227–2234, 1998.

[57] Yoël Forterre, Jan M Skotheim, Jacques Dumais, and Lakshminarayanan Mahadevan. How the venus flytrap snaps. *Nature*, 433(7024):421, 2005.

[58] Christian Frantz, Kathleen M Stewart, and Valerie M Weaver. The extracellular matrix at a glance. *J Cell Sci*, 123(24):4195–4200, 2010.

[59] Margaret L Gardel, Karen E Kasza, Clifford P Brangwynne, Jiayu Liu, and David A Weitz. Mechanical response of cytoskeletal networks. *Methods in cell biology*, 89:487–519, 2008.

[60] Scott F Gilbert. Induction and the origins of developmental genetics. In *A conceptual history of modern embryology*, pages 181–206. Springer, 1991.

[61] Frederick Gittes, Brian Mickey, Jilda Nettleton, and Jonathon Howard. Flexural rigidity of microtubules and actin filaments measured from thermal fluctuations in shape. *The Journal of cell biology*, 120(4):923–934, 1993.

[62] Richard Goodyear and Guy Richardson. Pattern formation in the basilar papilla: evidence for cell rearrangement. *Journal of Neuroscience*, 17(16):6289–6301, 1997.

[63] Alain Goriely and Martine Ben Amar. Differential growth and instability in elastic shells. *Physical review letters*, 94(19):198103, 2005.

[64] F Graner, Y Jiang, E Janiaud, and C Flament. Equilibrium states and ground state of two-dimensional fluid foams. *Physical Review E*, 63(1):011402, 2000.

[65] Carsten Grashoff, Brenton D Hoffman, Michael D Brenner, Ruobo Zhou, Maddy Parsons, Michael T Yang, Mark A McLean, Stephen G Sligar, Christopher S Chen, Taekjip Ha, et al. Measuring mechanical tension across vinculin reveals regulation of focal adhesion dynamics. *Nature*, 466(7303):263, 2010.

[66] Jeremy BA Green and James Sharpe. Positional information and reaction-diffusion: two big ideas in developmental biology combine. *Development*, 142(7):1203–1211, 2015.

[67] Branko Grünbaum and Geoffrey Colin Shephard. *Tilings and patterns*. Freeman, 1987.

[68] Charlène Guillot and Thomas Lecuit. Mechanics of epithelial tissue homeostasis and morphogenesis. *Science*, 340(6137):1185–1189, 2013.

[69] Jennifer M Halbleib and W James Nelson. Cadherins in development: cell adhesion, sorting, and tissue morphogenesis. *Genes & development*, 20(23):3199–3214, 2006.

[70] Tony JC Harris and Ulrich Tepass. Adherens junctions: from molecules to morphogenesis. *Nature reviews Molecular cell biology*, 11(7):502–514, 2010.

[71] M Amanda Hartman and James A Spudich. The myosin superfamily at a glance. *J Cell Sci*, 125(7):1627–1632, 2012.

[72] Rachel B Hazan, Lan Kang, Susanna Roe, Patrick I Borgen, and David L Rimm. Vinculin is associated with the e-cadherin adhesion complex. *Journal of Biological Chemistry*, 272(51):32448–32453, 1997.

[73] Idse Heemskerk and Sebastian J Streichan. Tissue cartography: compressing bioimage data by dimensional reduction. *Nature methods*, 12(12):1139, 2015.

[74] Volkhard Helms. Fluorescence resonance energy transfer. *Principles of Computational Cell Biology*, page 202, 2008.

[75] Silke Henkes, Corey S OHern, and Bulbul Chakraborty. Entropy and temperature of a static granular assembly: an ab initio approach. *Physical review letters*, 99(3):038002, 2007.

[76] Kenneth C Holmes. Structural biology: actin in a twist. *Nature*, 457(7228):389–390, 2009.

[77] H. Honda. Geometric models for cells in tissues. *International Review for Cytology*, (81):191–248, 1983.

[78] Hisao Honda. Description of cellular patterns by dirichlet domains: The two-dimensional case. *Journal of Theoretical Biology*, 72(3):523IN4531–530543, 1978.

[79] Hisao Honda, Hachiro Yamanaka, and Goro Eguchi. Transformation of a polygonal cellular pattern during sexual maturation of the avian oviduct epithelium: computer simulation. *Development*, 98(1):1–19, 1986.

[80] Lars Hufnagel, Aurelio A Teleman, Hervé Rouault, Stephen M Cohen, and Boris I Shraiman. On the mechanism of wing size determination in fly development. *Proceedings of the National Academy of Sciences*, 104(10):3835–3840, 2007.

[81] Kenneth D Irvine and Eric Wieschaus. Cell intercalation during drosophila germband extension and its regulation by pair-rule segmentation genes. *Development*, 120(4):827–841, 1994.

[82] S Ishihara, K Sugimura, SJ Cox, I Bonnet, Y Bellaiche, and F Graner. Comparative study of non-invasive force and stress inference methods in tissue. *arXiv preprint arXiv:1301.4298*, 2013.

[83] Shuji Ishihara and Kaoru Sugimura. Bayesian inference of force dynamics during morphogenesis. *Journal of theoretical biology*, 313:201–211, 2012.

[84] François Jacob and Jacques Monod. Genetic regulatory mechanisms in the synthesis of proteins. *Journal of molecular biology*, 3(3):318–356, 1961.

[85] Frank Jülicher, Armand Ajdari, and Jacques Prost. Modeling molecular motors. *Reviews of Modern Physics*, 69(4):1269, 1997.

[86] Raghu Kalluri and Robert A Weinberg. The basics of epithelial-mesenchymal transition. *The Journal of clinical investigation*, 119(6):1420, 2009.

[87] Evelyn Fox Keller. *Refiguring life: Metaphors of twentieth-century biology.* Columbia University Press, 1995.

[88] Ray Keller, Lance Davidson, Anna Edlund, Tamira Elul, Max Ezin, David Shook, and Paul Skoglund. Mechanisms of convergence and extension by cell intercalation. *Philosophical Transactions of the Royal Society of London B: Biological Sciences*, 355(1399):897–922, 2000.

[89] Daniel P Kiehart, Catherine G Galbraith, Kevin A Edwards, Wayne L Rickoll, and Ruth A Montague. Multiple forces contribute to cell sheet morphogenesis for dorsal closure in drosophila. *The Journal of cell biology*, 149(2):471–490, 2000.

[90] Anatoly B Kolomeisky and Michael E Fisher. Molecular motors: a theorist's perspective. *Annu. Rev. Phys. Chem.*, 58:675–695, 2007.

[91] Deqing Kong, Fred Wolf, and Jörg Großhans. Forces directing germ-band extension in drosophila embryos. *Mechanisms of development*, 2016.

[92] Mihály Kovács, Kavitha Thirumurugan, Peter J Knight, and James R Sellers. Load-dependent mechanism of nonmuscle myosin 2. *Proceedings of the National Academy of Sciences*, 104(24):9994–9999, 2007.

[93] Uros Krzic, Stefan Gunther, Timothy E Saunders, Sebastian J Streichan, and Lars Hufnagel. Multiview light-sheet microscope for rapid in toto imaging. *Nature methods*, 9(7):730–733, 2012.

[94] CD Kuglin. The phase correlation image alignment method. In *Proc. International Conference on Cyber-netics Society*, pages 163–165, 1975.

[95] Harold W Kuhn. The hungarian method for the assignment problem. *Naval Research Logistics (NRL)*, 2(1-2):83–97, 1955.

[96] Lev D Landau and EM Lifshitz. Theory of elasticity, vol. 7. *Course of Theoretical Physics*, 3:109, 1986.

[97] Lev D Landau and EM Lifshitz. Theory of elasticity, vol. 7. *Course of Theoretical Physics*, 3:109, 1986.

[98] Thomas Lecuit et al. E-cadherin junctions as active mechanical integrators in tissue dynamics. *Nature cell biology*, 17(5):533, 2015.

[99] Thomas Lecuit and Pierre-Francois Lenne. Cell surface mechanics and the control of cell shape, tissue patterns and morphogenesis. *Nature reviews. Molecular cell biology*, 8(8):633, 2007.

[100] Harvey Lodish. *Molecular cell biology.* Macmillan, 2008.

[101] Harvey Lodish, Arnold Berk, S Lawrence Zipursky, Paul Matsudaira, David Baltimore, James Darnell, et al. *Molecular cell biology*, volume 3. Scientific American Books New York, 1995.

[102] Marion Louveaux, Jean-Daniel Julien, Vincent Mirabet, Arezki Boudaoud, and Olivier Hamant. Cell division plane orientation based on tensile stress in arabidopsis thaliana. *Proceedings of the National Academy of Sciences*, page 201600677, 2016.

[103] Claire M Lye, Guy B Blanchard, Huw W Naylor, Leila Muresan, Jan Huisken, Richard J Adams, and Bénédicte Sanson. Mechanical coupling between endoderm invagination and axis extension in drosophila. *PLoS biology*, 13(11):e1002292, 2015.

[104] Xiaoyan Ma, Holley E Lynch, Peter C Scully, and M Shane Hutson. Probing embryonic tissue mechanics with laser hole drilling. *Physical biology*, 6(3):036004, 2009.

[105] Madhav Mani. Personal communication.

[106] M Cristina Marchetti, JF Joanny, S Ramaswamy, TB Liverpool, J Prost, Madan Rao, and R Aditi Simha. Hydrodynamics of soft active matter. *Reviews of Modern Physics*, 85(3):1143, 2013.

[107] Adam C Martin. Pulsation and stabilization: contractile forces that underlie morphogenesis. *Developmental biology*, 341(1):114–125, 2010.

[108] Adam C Martin, Michael Gelbart, Rodrigo Fernandez-Gonzalez, Matthias Kaschube, and Eric F Wieschaus. Integration of contractile forces during tissue invagination. *The Journal of cell biology*, pages jcb–200910099, 2010.

[109] Adam C Martin, Matthias Kaschube, and Eric F Wieschaus. Pulsed actin-myosin network contractions drive apical constriction. *Nature*, 457(7228):495, 2009.

[110] Takeshi Maruyama, Stephanie K Dougan, Matthias C Truttmann, Angelina M Bilate, Jessica R Ingram, and Hidde L Ploegh. Increasing the efficiency of precise genome editing with crispr-cas9 by inhibition of nonhomologous end joining. *Nature biotechnology*, 33(5):538–542, 2015.

[111] Frank M Mason, Michael Tworoger, and Adam C Martin. Apical domain polarization localizes actin–myosin activity to drive ratchet-like apical constriction. *Nature cell biology*, 15(8):926–936, 2013.

[112] Frank J Massey Jr. The kolmogorov-smirnov test for goodness of fit. *Journal of the American statistical Association*, 46(253):68–78, 1951.

[113] J Clerk Maxwell. L. on the calculation of the equilibrium and stiffness of frames. *The London, Edinburgh, and Dublin Philosophical Magazine and Journal of Science*, 27(182):294–299, 1864.

[114] Fanjie Meng, Thomas M Suchyna, and Frederick Sachs. A fluorescence energy transfer-based mechanical stress sensor for specific proteins in situ. *The FEBS journal*, 275(12):3072–3087, 2008.

[115] Callie Johnson Miller and Lance Davidson. The interplay between cell signaling and mechanics in developmental processes. *Nature Reviews. Genetics*, 14(10):733, 2013.

[116] Atsushi Miyawaki. Development of probes for cellular functions using fluorescent proteins and fluorescence resonance energy transfer. *Annual review of biochemistry*, 80:357–373, 2011.

[117] Steven Munevar, Yu-li Wang, and Micah Dembo. Traction force microscopy of migrating normal and h-ras transformed 3t3 fibroblasts. *Biophysical journal*, 80(4):1744–1757, 2001.

[118] James Munkres. Algorithms for the assignment and transportation problems. *Journal of the society for industrial and applied mathematics*, 5(1):32–38, 1957.

[119] JD Murray and GF Oster. Generation of biological pattern and form. *Mathematical Medicine and Biology: A Journal of the IMA*, 1(1):51–75, 1984.

[120] Michael Murrell, Patrick W Oakes, Martin Lenz, and Margaret L Gardel. Forcing cells into shape: the mechanics of actomyosin contractility. *Nature reviews. Molecular cell biology*, 16(8):486, 2015.

[121] Joseph Needham. Chemical embryology. *Annual Review of Biochemistry*, 1(1):507–526, 1932.

[122] W James Nelson. Regulation of cell–cell adhesion by the cadherin–catenin complex, 2008.

[123] Alexander Nestor-Bergmann, Georgina Goddard, and Sarah Woolner. Force and the spindle: mechanical cues in mitotic spindle orientation. In *Seminars in cell & developmental biology*, volume 34, pages 133–139. Elsevier, 2014.

[124] Kelly K Nikolaidou and Kathy Barrett. A rho gtpase signaling pathway is used reiteratively in epithelial folding and potentially selects the outcome of rho activation. *Current Biology*, 14(20):1822–1826, 2004.

[125] Mayuko Nishimura, Yoshiko Inoue, and Shigeo Hayashi. A wave of egfr signaling determines cell alignment and intercalation in the drosophila tracheal placode. *Development*, 134(23):4273–4282, 2007.

[126] Tamako Nishimura and Masatoshi Takeichi. Remodeling of the adherens junctions during morphogenesis. *Current topics in developmental biology*, 89:33–54, 2009.

[127] Melanie F Norstrom, Philip A Smithback, and Ronald S Rock. Unconventional processive mechanics of non-muscle myosin iib. *Journal of Biological Chemistry*, 285(34):26326–26334, 2010.

[128] C Nüsslein-Volhard. Maternal effect mutations that alter the spatial coordinates of the embryo of drosophila melanogaster. *Determinants of spatial organization*, 28, 1979.

[129] Christiane Nüsslein-Volhard and Eric Wieschaus. Mutations affecting segment number and polarity in drosophila. *Nature*, 287(5785):795–801, 1980.

[130] Andrew C Oates, Nicole Gorfinkiel, Marcos Gonzalez-Gaitan, and Carl-Philipp Heisenberg. Quantitative approaches in developmental biology. *Nature reviews. Genetics*, 10(8):517, 2009.

[131] G Odell, G Oster, B Burnside, and P Alberch. A mechanical model for epithelial morphogenesis. *Journal of mathematical biology*, 9(3):291–295, 1980.

[132] George F Oster, James D Murray, and AK Harris. Mechanical aspects of mesenchymal morphogenesis. *Development*, 78(1):83–125, 1983.

[133] Yuanwang Pan, Idse Heemskerk, Consuelo Ibar, Boris I Shraiman, and Kenneth D Irvine. Differential growth triggers mechanical feedback that elevates hippo signaling. *Proceedings of the National Academy of Sciences*, page 201615012, 2016.

[134] J Thomas Parsons, Alan Rick Horwitz, and Martin A Schwartz. Cell adhesion: integrating cytoskeletal dynamics and cellular tension. *Nature reviews. Molecular cell biology*, 11(9):633, 2010.

[135] A Ponti, M Machacek, SL Gupton, CM Waterman-Storer, and G Danuser. Two distinct actin networks drive the protrusion of migrating cells. *Science*, 305(5691):1782–1786, 2004.

[136] Marko Popović, Amitabha Nandi, Matthias Merkel, Raphaël Etournay, Suzanne Eaton, Frank Jülicher, and Guillaume Salbreux. Active dynamics of tissue shear flow. *New Journal of Physics*, 19(3):033006, 2017.

[137] Philippe-Alexandre Pouille, Padra Ahmadi, Anne-Christine Brunet, and Emmanuel Farge. Mechanical signals trigger myosin ii redistribution and mesoderm invagination in drosophila embryos. *Sci. Signal.*, 2(66):ra16–ra16, 2009.

[138] Douglas C Prasher, Virginia K Eckenrode, William W Ward, Frank G Prendergast, and Milton J Cormier. Primary structure of the aequorea victoria green-fluorescent protein. *Gene*, 111(2):229–233, 1992.

[139] Johann Radon. On the determination of functions from their integral values along certain manifolds. *IEEE transactions on medical imaging*, 5(4):170–176, 1986.

[140] Sabyasachi Rakshit and Sanjeevi Sivasankar. Biomechanics of cell adhesion: how force regulates the lifetime of adhesive bonds at the single molecule level. *Physical Chemistry Chemical Physics*, 16(6):2211–2223, 2014.

[141] Sriram Ramaswamy. The mechanics and statistics of active matter. 2010.

[142] Khushboo Rastogi, Mohammed Shabeel Puliyakodan, Vikas Pandey, Sunil Nath, and Ravikrishnan Elangovan. Maximum limit to the number of myosin ii motors participating in processive sliding of actin. *Scientific reports*, 6, 2016.

[143] Cordelia Rauskolb, Shuguo Sun, Gongping Sun, Yuanwang Pan, and Kenneth D . Cytoskeletal tension inhibits hippo signaling through an ajuba-warts complex. *Cell*, 158(1):143–156, 2014.

[144] Matteo Rauzi, Uros Krzic, Timothy E Saunders, Matej Krajnc, Primož Ziherl, Lars Hufnagel, and Maria Leptin. Embryo-scale tissue mechanics during drosophila gastrulation movements. *Nature communications*, 6, 2015.

[145] Matteo Rauzi, Pierre-François Lenne, and Thomas Lecuit. Planar polarized actomyosin contractile flows control epithelial junction remodelling. *Nature*, 468(7327):1110, 2010.

[146] Matteo Rauzi, Pascale Verant, Thomas Lecuit, and Pierre-Francois Lenne. Nature and anisotropy of cortical forces orienting drosophila tissue morphogenesis. *Nature cell biology*, 10(12):1401, 2008.

[147] Ivan Rayment, Hazel M Holden, Michael Whittaker, Christopher B Yohn, Michael Lorenz, Kenneth C Holmes, and Ronald A Milligan. Structure of the actin-myosin complex and its implications for muscle contraction. *Science*, 261:58–58, 1993.

[148] Wayne L Rickoll and SJ Counce. Morphogenesis in the embryo ofdrosophila melanogastergerm band extension. *Wilhelm Roux's archives of developmental biology*, 188(3):163–177, 1980.

[149] Katherine W Rogers and Alexander F Schier. Morphogen gradients: from generation to interpretation. *Annual review of cell and developmental biology*, 27:377–407, 2011.

[150] David Rudel and Ralf J Sommer. The evolution of developmental mechanisms. *Developmental biology*, 264(1):15–37, 2003.

[151] Benedikt Sabass, Margaret L Gardel, Clare M Waterman, and Ulrich S Schwarz. High resolution traction force microscopy based on experimental and computational advances. *Biophysical journal*, 94(1):207–220, 2008.

[152] Michal Sahaf and Eran Sharon. The rheology of a growing leaf: stress-induced changes in the mechanical properties of leaves. *Journal of experimental botany*, 67(18):5509–5515, 2016.

[153] DR Sengelaub and BL Finlay. Cell death in the mammalian visual system during normal development: I. retinal ganglion cells. *Journal of Comparative Neurology*, 204(4):311–317, 1982.

[154] Friedhelm Serwane, Alessandro Mongera, Payam Rowghanian, David A Kealhofer, Adam A Lucio, Zachary M Hockenbery, and Otger Campàs. In vivo quantification of spatially-varying mechanical properties in developing tissues. *Nature methods*, 14(2):181, 2017.

[155] Eran Sharon and Efi Efrati. The mechanics of non-euclidean plates. *Soft Matter*, 6(22):5693–5704, 2010.

[156] Eran Sharon, Benoit Roman, and Harry L Swinney. Geometrically driven wrinkling observed in free plastic sheets and leaves. *Physical Review E*, 75(4):046211, 2007.

[157] Annette M Shewan, Madhavi Maddugoda, Astrid Kraemer, Samantha J Stehbens, Suzie Verma, Eva M Kovacs, et al. Myosin 2 is a key rho kinase target necessary for the local concentration of e-cadherin at cell–cell contacts. *Molecular biology of the cell*, 16(10):4531–4542, 2005.

[158] Osamu Shimomura, Frank H Johnson, and Yo Saiga. Extraction, purification and properties of aequorin, a bioluminescent protein from the luminous hydromedusan, aequorea. *Journal of Cellular Physiology*, 59(3):223–239, 1962.

[159] Boris I Shraiman. Mechanical feedback as a possible regulator of tissue growth. *Proceedings of the National Academy of Sciences of the United States of America*, 102(9):3318–3323, 2005.

[160] J Maynard Smith, Richard Burian, Stuart Kauffman, Pere Alberch, John Campbell, Brian Goodwin, Russell Lande, David Raup, and Lewis Wolpert. Developmental constraints and evolution: a perspective from the mountain lake conference on development and evolution. *The Quarterly Review of Biology*, 60(3):265–287, 1985.

[161] Michael Smutny, Hayley L Cox, Joanne M Leerberg, Eva M Kovacs, Mary Anne Conti, Charles Ferguson, Nicholas A Hamilton, Robert G Parton, Robert S Adelstein, and Alpha S Yap. Myosin ii isoforms identify distinct functional modules that support integrity of the epithelial zonula adherens. *Nature cell biology*, 12(7):696, 2010.

[162] C Sommer, C Strahle, U Kothe, and FA Hamprecht. ilastik: Interactive learning and segmentation toolkit. *Eighth IEEE International Symposium on Biomedical Imaging (ISBI). Proceedings*, 230, 2011.

[163] David Sprinzak. Personal communication.

[164] Karel Svoboda and Steven M Block. Biological applications of optical forces. *Annual review of biophysics and biomolecular structure*, 23(1):247–285, 1994.

[165] Dari Sweeton, Suki Parks, Michael Costa, and Eric Wieschaus. Gastrulation in drosophila: the formation of the ventral furrow and posterior midgut invaginations. *Development*, 112(3):775–789, 1991.

[166] Noel M Swerdlow. Astronomy in the renaissance. In *Astronomy before the Telescope*, pages 187–230, 1996.

[167] Darcy Wentworth Thompson et al. On growth and form. *On growth and form.*, 1942.

[168] John Philip Trinkaus. Cells into organs: the forces that shape the embryo. 1984.

[169] Alan Mathison Turing. The chemical basis of morphogenesis. *Philosophical Transactions of the Royal Society of London B: Biological Sciences*, 237(641):37–72, 1952.

[170] Matthew J Tyska and David M Warshaw. The myosin power stroke. *Cytoskeleton*, 51(1):1–15, 2002.

[171] Miguel Vicente-Manzanares, Xuefei Ma, Robert S Adelstein, and Alan Rick Horwitz. Non-muscle myosin ii takes centre stage in cell adhesion and migration. *Nature reviews. Molecular cell biology*, 10(11):778, 2009.

[172] Jacques Villain. Two-dimensional solids and their interaction with substrates. In *Ordering in strongly fluctuating condensed matter systems*, pages 221–260. Springer, 1980.

[173] Georges Voronoï. Nouvelles applications des paramètres continus à la théorie des formes quadratiques. deuxième mémoire. recherches sur les parallélloèdres primitifs. *Journal für die reine und angewandte Mathematik*, 134:198–287, 1908.

[174] Elise Walck-Shannon and Jeff Hardin. Cell intercalation from top to bottom. *Nature reviews. Molecular cell biology*, 15(1):34, 2014.

[175] Shawn W. Walker. Felicity wiki documentation, 2017.

[176] John B Wallingford, Scott E Fraser, and Richard M Harland. Convergent extension: the molecular control of polarized cell movement during embryonic development. *Developmental cell*, 2(6):695–706, 2002.

[177] Chun-Chao Wang, Leen Jamal, and Kevin A Janes. Normal morphogenesis of epithelial tissues and progression of epithelial tumors. *Wiley Interdisciplinary Reviews: Systems Biology and Medicine*, 4(1):51–78, 2012.

[178] James D Watson, Francis HC Crick, et al. Molecular structure of nucleic acids. *Nature*, 171(4356):737–738, 1953.

[179] Da Weaire and N Rivier. Soap, cells and statistics. random patterns in two dimensions. *Contemporary Physics*, 25(1):59–99, 1984.

[180] Eric Wieschaus and Christiane Nüsslein-Volhard. The heidelberg screen for pattern mutants of drosophila: A personal account. *Annual review of cell and developmental biology*, 32:1–46, 2016.

[181] Frederik Wirtz-Peitz and Jennifer A Zallen. Junctional trafficking and epithelial morphogenesis. *Current opinion in genetics & development*, 19(4):350–356, 2009.

[182] Tanya Wolff and Donald F Ready. The beginning of pattern formation in the drosophila compound eye: the morphogenetic furrow and the second mitotic wave. *Development*, 113(3):841–850, 1991.

[183] Lewis Wolpert. Positional information and the spatial pattern of cellular differentiation. *Journal of theoretical biology*, 25(1):1–47, 1969.

[184] Matthew A Wyczalkowski, Zi Chen, Benjamen A Filas, Victor D Varner, and Larry A Taber. Computational models for mechanics of morphogenesis. *Birth Defects Research Part C: Embryo Today: Reviews*, 96(2):132–152, 2012.

[185] Jennifer A Zallen and J Todd Blankenship. Multicellular dynamics during epithelial elongation. In *Seminars in cell & developmental biology*, volume 19, pages 263–270. Elsevier, 2008.

[186] Jennifer A Zallen and Eric Wieschaus. Patterned gene expression directs bipolar planar polarity in drosophila. *Developmental cell*, 6(3):343–355, 2004.

[187] Jennifer A Zallen and Richard Zallen. Cell-pattern disordering during convergent extension in drosophila. *Journal of Physics: Condensed Matter*, 16(44):S5073, 2004.